Chiroptically-Active Metal Oxide Nanomaterials

Trinity College Dublin

The University of Dublin

A thesis submitted to the School of Chemistry,

Trinity College, the University of Dublin,

for the degree of Doctor of Philosophy

Olan Cleary

Under the supervision of Prof. Yurii K. Gun'ko

September 2017

Abstract

The aim of this work was to develop and characterise a variety of new chiroptically-active metal oxide nanomaterials, with a view to exploring their potential enantioselective catalytic, biomedical, chiroptical applications.

In this thesis, Chapter 1 presents a literature review of the areas relevant to this research and is a general introduction to the field chiroptically-active nanomaterials.

Chapter 2 details the synthesis and characterisation of a chiral and luminescent TiO_2 nanomaterials which have been prepared by a single step nonaqueous synthesis. These materials are then fully characterised by various instrumental techniques. These chiroptically-active TiO_2 NPs were also tested for catalytic activity in a range of organic transformations. Chiral polymer templates made from a tartaric acid and PEI complex are used for the production of an amorphous, chiroptically-active TiO_2 based nanomaterials. Finally, 16-2-16 gemini tartrates were also used for the preparation of chiral TiO_2 with a helical morphology.

In Chapter 3, a range of chiroptically-active Mn_3O_4 NPs were prepared through functionalisation with a variety of chiral ligands. The catalytic properties of the Mn_3O_4 NPs were also tested. The chiroptically-active Mn_3O_4 NPs were also tested for activity against against breast cancer cells. Finally, we report the synthesis and preliminary studies of a chiral metal organic framework (MOF) as a new chiral nanomaterial.

Chapter 4 reports the development of chiroptically-active and luminescent ZnO NPs. The chiroptical and luminescent properties of these NPs are also characterised.

Chapter 5 describes the development of a catalyst for both aldol and Michael reactions by

ligand self assembly on the surface of CeO_2 NPs.

Chapter 6 describes all experimental details relating to the work presented in this thesis and has been labelled with the specific experimental details concerning the results in each chapter. Details of all instrumental techniques used in our work are also presented in this chapter.

Chapter 7 provides the conclusions of the entire work and outlines the main achievements of our research. This chapter also includes details of future directions of our work.

Declaration

This thesis is submitted for the degree of Doctor of Philosophy to the University of Dublin, Trinity College and has not been submitted before for any degree or examination to this or any other university. Other than where acknowledged, all work described herein is original and carried out by the author alone. Permission is granted so that the Library may lend or copy this thesis upon request. This permission covers only single copies made for study purposes, subject to normal conditions of acknowledgement.

_____

Olan Cleary

Acknowledgements

First and foremost, I wish to express my gratitude to my supervisor, Professor Yurii Gun'ko. His astute guiding hand and great knowledge has been invaluable during the course of my studies. Secondly, I must thank Finn, Fearghal, Raquel, Dan, Shelley, Sarah, Vera and all of the members of the Gun'ko research group for their constant support and advice throughout the entirety of my time here.

A special mention must be given to Aurélien Vanderkerchekove, Cédric Vauthier and César Gomez for their excellent contributions to this research.

Thanks to Dr Manuel Reuther, Dr John O'Brien and Dr Brendan Twamley for helping me with all their technical expertise and know-how. It has been invaluable to me.

I would like to acknowledge Alex Loudon for putting up up with me for years, which have to have been the some of best years of my life so far.

Finally, I would also like to thank my family for the support they provided me through my entire life. I would like to especially acknowledge Rebecca for her constant love and encouragement whilst writing my thesis.

Contents

Contents

List of Figures

List of Schemes

List of Tables

Abbreviations

1D = one-dimensonal

2D = two-dimensional

CD = circular dichroism

BINAP = 2,2'-Bis(diphenylphosphino)-1,1'-binaphthyl

DCC = N,N'-dicyclohexylcarbodiimide

DMSO = dimethylsulfoxide

DR-CD = diffuse reflectance circular dichroism

DTA = differential thermal analysis

e.e. = enatiomeric excess

hr = hour

IR = infrared

OA = oleic acid

LCAO = linear combination of atomic orbitals

MOF = metal organic framework

MRI = magnetic resonance imaging

MTT = (3-(4,5-dimethylthiazol-2-yl)-2,5-diphenyltetrazolium

NOE = nuclear Overhauser effect

NOESY = nuclear Overhauser effect spectroscopy

NMR = nuclear magnetic resonance

NPs = nanoparticles

PDI = polydispersity index

PEI = polyethylenimine

PTFE = polytetrafluoroethylene

QD = quantum dot

rt = room temperature

SEM = scanning electron microscopy

SDS = sodium dodecyl sulfate

STEM = scanning tunneling electron microscopy

TBHP = tert-butyl hydroperoxide

TEM = transmission electron microscopy

THF = tetrahydrofuran

TGA = thermo-gravimetric analysis

TLC = thin-layer chromatography

UV-vis = Ultraviolet-visible

XRD = x-ray diffraction

Chapter 1

Introduction

1.1 Introduction to Nanomaterials

The area of nanomaterials includes several fields of research focusing on the development of new advanced materials that have found applications in catalysis, optics, medicine and computing, to name but a few. A nanomaterial is generally defined as a material that has at least one dimension in the size range of 1 to 100 nm. A comparison of various materials over differing size ranges is shown in Figure 1.1.

The current high interest in nanomaterials is due to their unique size-dependent properties which differ greatly from their bulk counterparts. Examples of size dependent features of nanoparticles include (but are not limited to) quantum confinement in semiconducting quantum dots,[1] the exceptional strength and conductivity displayed by graphene,[2] the superparamagnetism displayed by magnetic nanoparticles,[3,4] the size-dependent cellular uptake of NPs for biomedical applications,[5] and the increased catalytic surface area of nanocatalysts compared to the bulk.[6]

1.1.1 Metal oxide nanomaterials

Considering all of the materials that have been synthesised on the nanoscale, metal oxides are a particularly diverse set of materials. Their unique properties cover
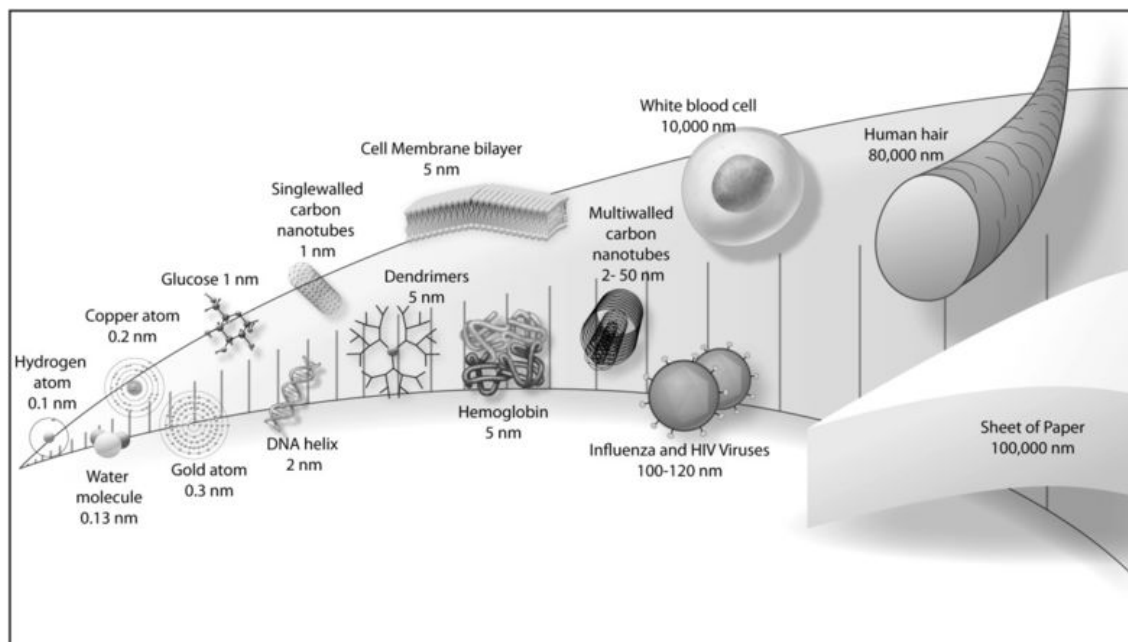
Figure 1.1: Sizes of various materials at the nanoscale compared to more familiar materials. Figure reproduced from Yokel *et al.*[7]

almost all of the many aspects of materials science. They have a wide range of potential crystal structures from the simple, cubic rock salt configuration to highly complex ones, and the nature of the metal-oxygen bond varies from almost ionic to covalent or metallic.[8] Due to such changes in structure and bonding, metal oxides possess a wide variety of properties and applications. Some oxides like RuO_2 or ReO_3 are metallic, whereas $BaTiO_3$ for example is an insulator. Other such as Fe_3O_4 are ferromagnetic[3] and others may exhibit photoluminescence as in the case of ZnO.[9–11] Metal oxides may also exhibit interesting catalytic behaviour, with a large number of oxidative, reductive and both Lewis and Brønsted acid-base catalysed processes being reported.[12] This wide range of applications stem from the unique electronic and structural properties of metal oxides. The electronic properties of metal oxides are well described by band theory and a brief description of this theory will be given in the following section. The description of the structural properties of metal oxide surfaces is currently a developing field and an overview will be given in Section 1.1.1.2.

1.1.1.1 Band theory

If one tries to model the bonding in a metal oxide by conventional molecular orbital theory, a problem emerges. There are not enough valence shell orbitals or electrons for each atom to form bonds with all it's neighbours. A model with multi-centre orbitals must then be used. As seen in the case of conducting metal oxides, the multi-centre orbitals must spread over the whole metal oxide crystal to account for electron mobility. This is described generally by band theory, a model of which is shown schematically in Figure 1.2. In this figure, increasing numbers of atoms and their respective atomic orbitals combine to form new systems. When two atoms combine, the overlap of two atomic orbitals results in two molecular orbitals, three atoms form three molecular orbitals and so on. This in known as the linear combination of atomic orbitals (LCAO). The energy separation between adjacent molecular orbitals decreases as the number of interacting orbitals increases. For n = 30, there are still discrete, well-resolved energy levels, but as n increases from 30 to a number close to Avogadro's number, the spacing between adjacent energy levels becomes almost infinitely small. The result is a continuum of energy levels. The levels that are lowest in energy correspond to mostly bonding combinations of atomic orbitals, those highest in energy correspond to mostly antibonding combinations, and those in the middle correspond to essentially nonbonding combinations.[13] This arrangement can be described as a band whereby the energy differences between the groups of molecular orbitals are so small that the system behaves as if a "continuous, non-quantized variation within the band is possible."[14]

An extended solid may have one of three different band structures as seen in Figure 1.2. If a solid has a filled valence band with a relatively low-lying empty band above it (a conduction band), then electrons can be excited by thermal energy from the filled band into the vacant band where they can then migrate through the crystal, making it a metal (conductive in nature). A fully occupied band separated from the next empty band by an energy separation (the band gap) leads to the material being either a semiconductor in the case of a small energy separation of an insulator in the case of a large energy separation.
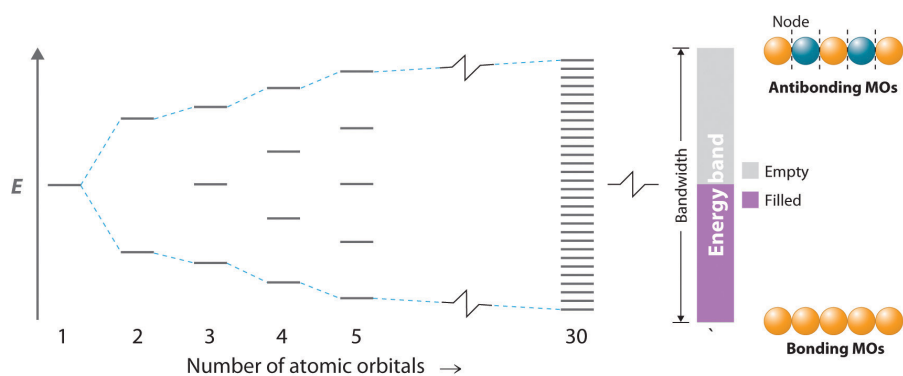
(a) The molecular orbital energy-level diagram for a linear arrangement of n atoms. Figure reproduced from Averill *et al.*[13]
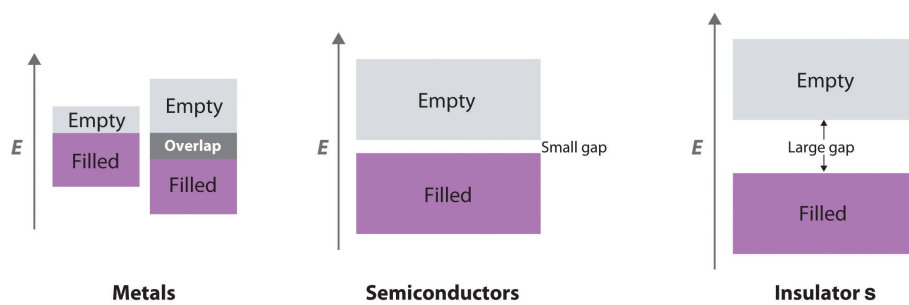
(b) Band structure of metals, semiconductors and insulators. Figure reproduced from Averill *et al.*[13]

Figure 1.2: Band theory and band structure
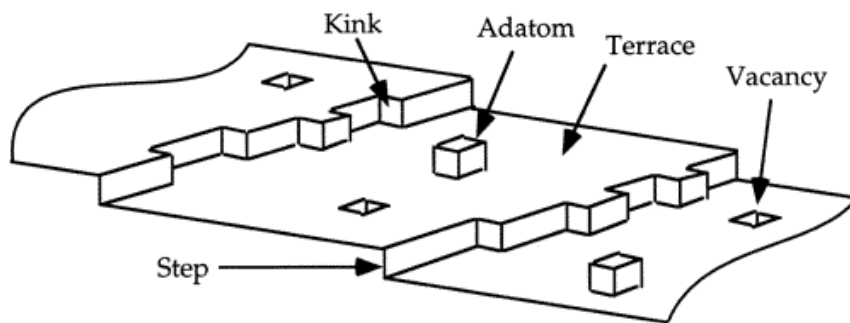
Figure 1.4: Different structural sites on a metal oxide surface. Figure reproduced from Brown *et al.*[16]

1.1.1.2   Surface properties of metal oxide nanomaterials

Whereas the electronic structure of metal oxide nanoparticles and the interaction of their surfaces with ligands may be adequately described by the application of both band theory and ligand field theory; the explanations given by these theories fail to account for the local physical structures present at the surface of metal oxide nanoparticles (Figure 1.4). These structures take the form of "defects" in the idealised crystal structure and are frequently where the majority of catalytic events take place. Defects are also responsible for the formation of holes in the CB an traps in the VB for photoluminescent and photocatalytic processes. Thus a full discussion of metal oxide nanoparticles cannot be completed without consideration of these features.

The physical and chemical properties of metal oxide NPs are dominated by surface effects. An example of this is that a spherical NP 3 nm in diameter will have nearly 50% of the atoms or ions on the surface. All crystals must also contain a certain number of defects above absolute zero due to thermodynamic considerations, and these defects form during the fabrication of any metal oxide nanomaterial, either intentionally or unintentionally.[15]

Examples of the defects that may be present at metal oxide surfaces include Frenkel (vacancy plus interstitial of the same type) and Schottky (balancing pairs of vacancies) defects. On oxide surfaces, these "point" defects can be cation vacancies, anion vacancies, or adatoms. Measurements of the electronic structure of a variety of oxide

surfaces have shown that the predominant type of defect formed when samples are heated are oxygen vacancies.[17]

1.1.2 Preparation of metal oxide nanomaterials

For the prepartion of metal oxide nanomaterials, two approaches are possible. The "top-down" or the "bottom-up" approach.[18] The "top-down" approach involves starting from larger starting materials that are then etched to remove crystals planes which are already present on the substrate. A top-down approach can thus be viewed as an approach where some parts of the material are removed from the substrate to form the nanostructure. The benefits of this approach are in the relatively low costs and scalability of the process. The "bottom-up" approach is where one starts from smaller building blocks to construct a nanomaterial. Chemical synthesis of NPs is a typical example of this approach. This is advantageous because there is larger scope to synthesise complex nanostructures and exert fine control over the surface chemistry of the NPs synthesised by this method. The "bottom-up" approach will be the method that will be focused upon in this thesis.

There are two main bottom up approaches to the preparation of metal oxide nano-materials. The first approach involves the co-precipitation of metal oxides from aqueous solutions of inorganic metal salts by adjusting the pH or temperature. The resulting salt impurities are washed away and the metal hydroxide product can be collected by filtration and then calcined to obtain a crystalline metal oxide mate-rial. A disadvantage of this method is that uncontrolled precipitation can often take place, leading to a wide range of sizes and structures in the final product. The role of counter ions formed during the reaction is also impossible to predict as they can potentially coordinate to the metal centre, altering chemical reactivity and influ-encing the final morphology and chemical composition of the obtained product.[12] The second approach to the preparation of metal oxide nanomaterials involves the hydrolysis of metal-organic precursors such as metal alkoxides. This involves two steps, hydrolysis and condensation (Scheme 1.1). Hydrolysis takes place where the alkoxide groups (-OR) of the metal-organic precursor are replace via nucleophilic

$$\equiv\text{M--OR} \quad + \quad H_2O \quad \longrightarrow \quad \equiv\text{M--OH} \quad + \quad \text{R--OH} \qquad (1.1)$$

$$\equiv\text{M--OH} \quad + \quad \text{HO--M}\equiv \quad \longrightarrow \quad \equiv\text{M--O--M}\equiv \quad + \quad H_2O \qquad (1.2)$$

$$\equiv\text{M--OR} \quad + \quad \text{HO--M}\equiv \quad \longrightarrow \quad \equiv\text{M--O--M}\equiv \quad + \quad \text{R--OH} \qquad (1.3)$$

Scheme 1.1: Main reactions in the hydrolysis of metal alkoxides. Hydrolysis (Eq. 1.1) and condensation, involving oxolation (Eq. 1.2) and alkoxolation (Eq. 1.3)

attack of the oxygen atom belonging to a water molecule (Eq. 1.1). Condensation reactions may then proceed between hydroxylated metal centres with the formation of water (oxolation) or the formation of an alcohol (alkoxolation). The amorphous products obtained can be purified by centrifugation and then calcined in order to obtain a crystalline material.[19]

Most transition metal alkoxides (such as $Ti(OEt)_4$) are highly sensitive to hydrolysis at room temperature and have inherently fast rate of condensation reactions that results in poor control over product morphology and a wide range of size distributions. This is due to the high electropositive character of the metal centre. The rates of hydrolysis and condensation can be controlled in a variety of ways however. The various factors influencing these rates include the length of the alkoxide chain, oligermerisation of the metal alkoxide precursor, the pH of the aqueous solution, the steric hindrance around the metal centre and the presence of chelating ligands.[20]

1.2 Chirality at the Nanoscale

Chirality is a property of asymmetry that is important over a wide range of sciences, from mathematics to biology and beyond. The basic concept of chirality is that a chiral molecule is non-superimposable upon it's mirror image. This concept was first presented by Louis Pasteur to the Chemical Society of Paris, where he demonstrated that the levorotary and dextrorotary properties of hemihedral tartaric acid crystals were due to their inherent asymmetry at the molecular level.[21] The field of chiral nanomaterials has grown over recent years as it has been demonstrated that chirality
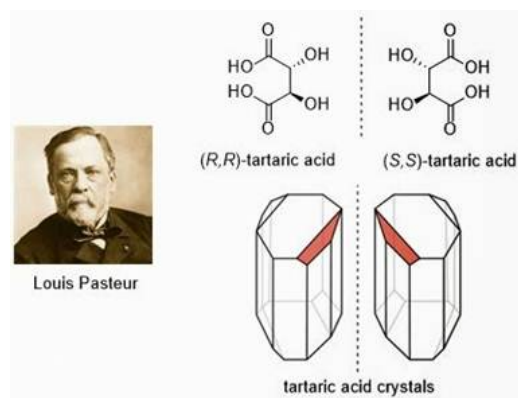
(a) Louis Pasteur and levorotary and dextrorotary crystals of tartaric acid. Figure reproduced from ref.[24]
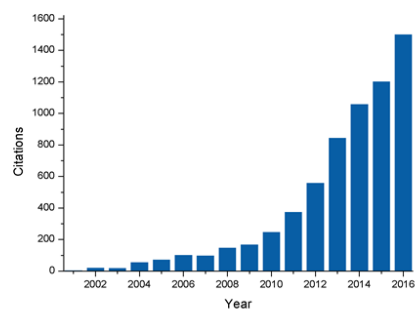
(b) Number of citations for publications concerning "Chiral nanomaterials" by year. Graph made using data from "Web of Science"

Figure 1.5: Chirality in the past and today

may exist in many different forms at the nanoscale. The resulting chiral nanomaterials can be used in a wide range of applications, from biomedical applications, to catalysis and chiroptical applications.[22,23] The rapid growth of interest in the field can be observed by noting that the number of citations for academic publications concerning "chiral nanomaterials" has almost tripled in the last four years (Figure 1.5b).

One of the simplest ways to define chirality is the fact that chiral entities display optical activity, i.e. they are able to rotate a plane of plane-polarised light. A related property of optical activity is circular dichroism, wherein a chormophore may display preferential absorption of left- and right-handed circularly polarised light (Figure 1.6). This is a useful property as it allows one to determine which chromophores are optically active within a given sample.[25] There are a number of different mechanisms that have been postulated in the literature whereby a chiral nanomaterial can manifest chiroptical activity. It is useful to classify these different mechanisms as they are related to the structure of the chiral nanomaterial. Broadly speaking, it is possible to identify 3 main groups of chiral nanomaterials:

- Chiral macrostructured nanomaterials

- Nanomaterials with instrinsic chirality and chiral ordering of surface atoms
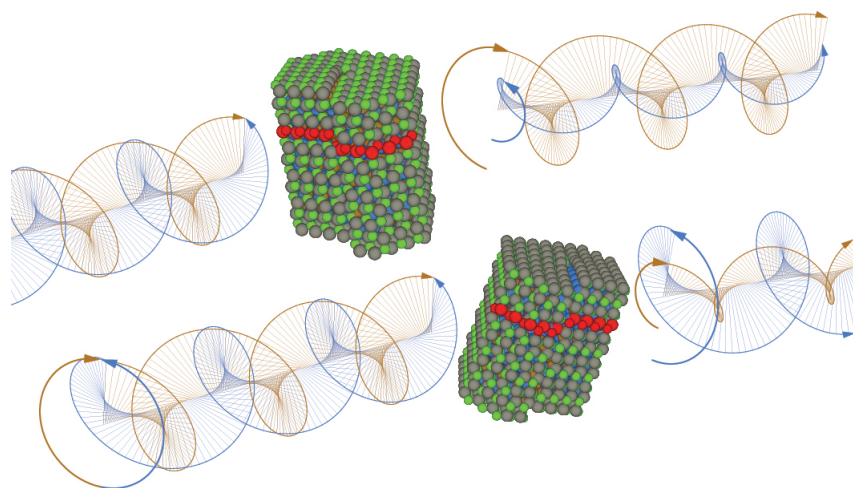
Figure 1.6: Levorotatory and dextrorotatory CdSe quantum dots with left and right chiral defects. Figure reproduced from Mukhina *et al.*[26]

- Nanomaterials with chiral ligand-induced circular dichroism

1.2.1   Chiral macrostructures

Nanomaterials can be CD-active by virtue of a chiral nanostructure. The most common structures of this type are based on single helices (Figure 1.7),[27–31] double helices[32] or helical stacking of achiral nano-units.[33,34] Chirality is not limited to helical-based structures however, as chirality can be present in nanorod dimers due to the dihedral angle between two achiral nanorods.[35] The origin of chirality in these macro-systems can be attributed to a long range chiral arrangement of chromophores (these may be organic groups, metallic, or semiconductor nanoparticles). These structures exhibit a collective response to circularly polarised light which is delocalised throughout the entire structure resulting in one of the circular polarisations of light exchanging energy more efficiently than the other. This circular dichroism response has a magnitude proportional to the overall size and long-range chiral nature of the aggregates.[36] To summarise, these systems contain a number of chromophores that by themselves are not intrinsically chiral, but are arranged in such a way that makes the whole system chiral.[37]
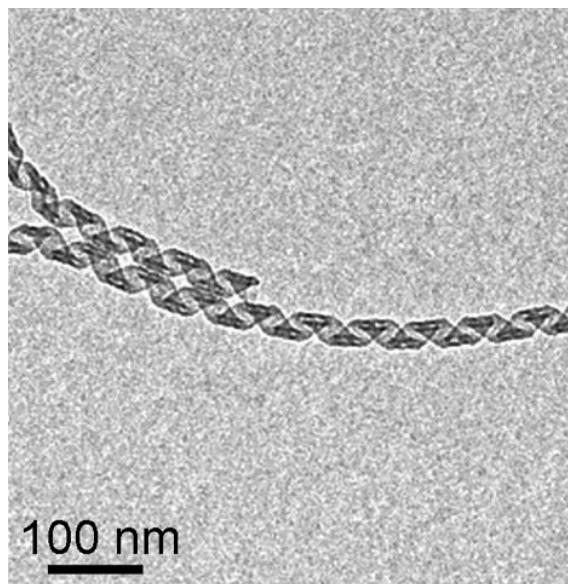
Figure 1.7: Chiral silica nanohelix, an example of a chiral macrostructure. TEM image reproduced from Delclos *et al.*[28]

1.2.2   Intrinsic chirality and chiral ordering of surface atoms

The second type of chirality in nanomaterials that can be found in the literature is attributed to the presence of a chiral surface of a nanomaterial. Chiral crystalline mesoporous silica structures have been prepared that do not exhibit any obvious chiral macrostructure such as a topologically characteristic helix. The origin of chirality in these structures has been postulated to be due to a geometrically ordered chiral surface whereby chiral blocks are distributed randomly throughout the surface.[38] A schematic example of these structures is shown in Figure 1.8. Similar structures are possibly present in an analogous TiO_2 material that has been prepared by a similar synthetic route.[39] Evidence for a chiral surface has also been observed in amorphous spherical TiO_2 nanoparticles. These particles exhibit a preference for the adsorption of the L-enantiomer of a racemic solution of camphor. This suggests the presence of a chiral surface.[40] It has been demonstrated that the chiral ordering of surface atoms is a successful strategy for the production of enantioselective electrochemical oxidation catalysts and there have been a number of reports of chiral metal oxide surfaces being used for this purpose.[41,42] A notable example is of a chiral surface has been presented by Switzer *et al.* who have demonstrated chiral CuO films with
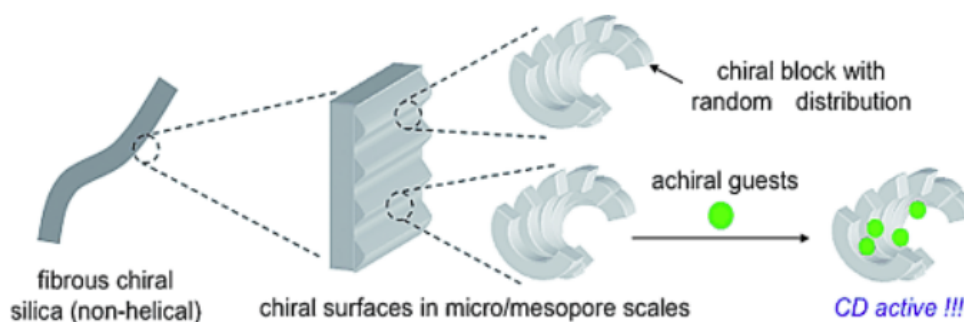
(a) Representation of geometrically ordered chiral blocks distributed randomly through the silica wall and bounded chromophores. Figure reproduced from Matsukizono *et al.*[44]
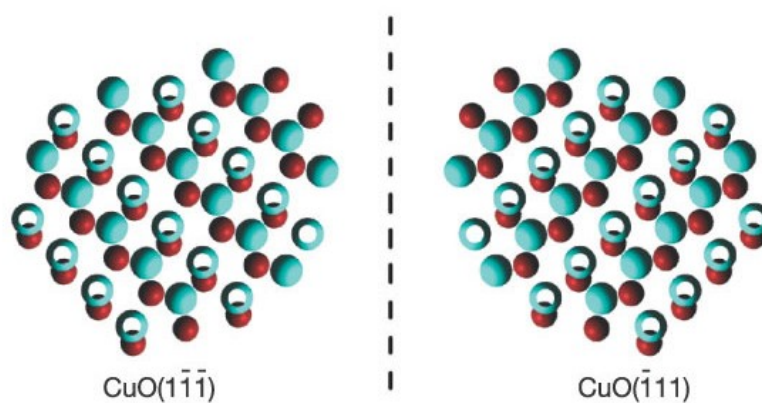
(b) Chiral CuO surfaces with mirror image symmetry. Figure reproduced from Switzer *et al.*[43]

Figure 1.8: Examples of intrinsic chirality and chiral ordering of surface atoms

mirror-image symmetry (Figure 1.8).[43]

1.2.3 Ligand-induced circular dichrosim

Circular dichroism can also be present in inorganic nanomaterial due to the presence of chiral organic ligands on their surfaces. This induced circular dichroism can manifest itself through two main mechanisms. The first case involves a dynamic Coulomb interaction between a chiral adsorbed molecule and a plasmonic metal or semiconductor nanocrystal. These near field dipole-dipole interactions have been observed in the case of Au, Ag and CdTe nanoparticles.[45] The magnitude of this plasmonic CD response is directly related to the optical rotary dispersion (ORD)
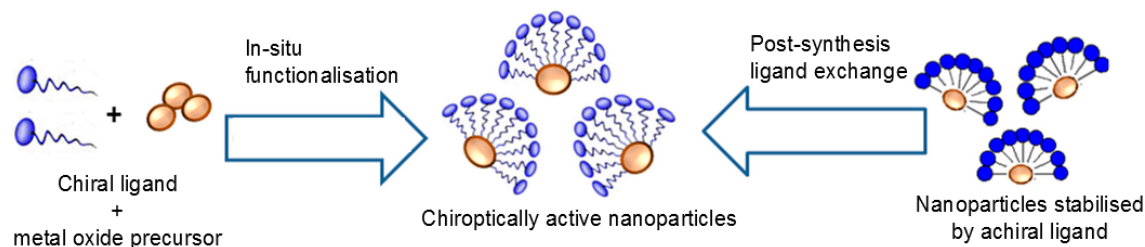
Figure 1.10: *In situ* functionalisation of nanomaterials vs post synthesis ligand exchange. Figure altered from original published by Razzaque *et al.*[52]

properties of the adsorbed organic molecules. The presence of chiral molecules with an ORD response at the plasmonic wavelength makes the plasmonic resonance itself chiral. This has been postulated to be the origin of chiral plasmonic peaks in the case of achiral nanoparticles functionalised with a chiral organic molecular layer.[46]

The second mechanism by which induced optical chirality may be present is whereby the electronic states of an adsorbed chiral molecule overlap with the orbital wave functions of an achiral nanocrystal. This is the mechanism of ligand-induced chirality that is prevalent in semiconductor NPs.[47–49] This overlap of electronic wave function leads to the chirality of electronic surface states. A ligand may couple strongly to a metal center, so as to create new electronic states with metal-ligand character, these ligands are known as non-innocent ligands.[50] This mixed-character state that forms delocalizes not only over the metal to which the ligand binds, but also over the entire crystal lattice of the semiconductor NP, such that binding of the ligand creates a new electronic structure without distinct NP or ligand phases.[51]

A noteworthy phenomenon is that chirality may be induced in the opposite direction to the above examples. Chiral crystalline nanomaterials have been found to induce a circular dichroism response in achiral ligands bound to their surfaces. It has been asserted that this occurs via the same mechanism of overlapping of chiral electronic states as discussed in the previous examples. The effect has been observed in copper (II) tetra-4-sulfonatophenyl-porphyrin complexes assembled onto chiral TiO_2 helices[27] as well as $PhSiO_3$ groups bound to the surface of chiral mesoporous silica.[38]

There are two main "bottom-up" approaches for the production of chiroptically-active nanoparticles stabilised by chiral ligands (Figure 1.10). The first approach is an *In situ* functionalisation of nanoparticles with a suitable chiral ligand during the NP synthesis.[53] This is an advantageous appraoch because it is a one-step synthesis and there is the possibility to synthesise novel chiral morphologies as the chiral ligand may act as a "template" for the synthesis. A drawback of this method is that optimal reaction parameters can be difficult to ascertain. The second approach is a post synthesis ligand exchange, whereby initial achiral ligands are exchanged with chiral ligands.[54] This method enables use of established synthesis to provide nanoparticles of desired morphology and crystallinity. The NPs can then be transferred from the organic phase to an aqueous phase and *vice versa*.

1.2.4   Chiroptically-active luminescent nanomaterials

Chiropticaly-active luminescent nanomaterials are typically represented by chiral semiconductor quantum dots. Chiral quantum dots were first reported by Moloney *et al.* in 2007.[55] Since this landmark publication, chiral quantum dots have since been utilised in applications such as sensing of chiral molecules,[56,57] circularly po-larised luminescence sources[48] and cellular imaging agents.[58]

As discussed in Section 1.1.1.1, the band theory of a continuum of bands in a bulk material owes its origin to huge number of LCAOs in an extended solid. When a materials size is reduced to the nanometre range, the number of atoms is vastly reduced. This means that the continuum of bands is no longer in effect and the electronic properties are more accurately described by finitely spaced discrete energy levels that make up the VB and CB. This is known as the quantum size effect and an example of it's effects upon the band gap of luminescent semiconductor quantum dots is shown in Figure 1.11.

Since the band gap can be tuned by varying the size of the QD, the absorption and emission can be tuned across a range. The absorption profile of a quantumly con-fined nanostructure exhibits a sharp peak, which is indicative of the exciton binding
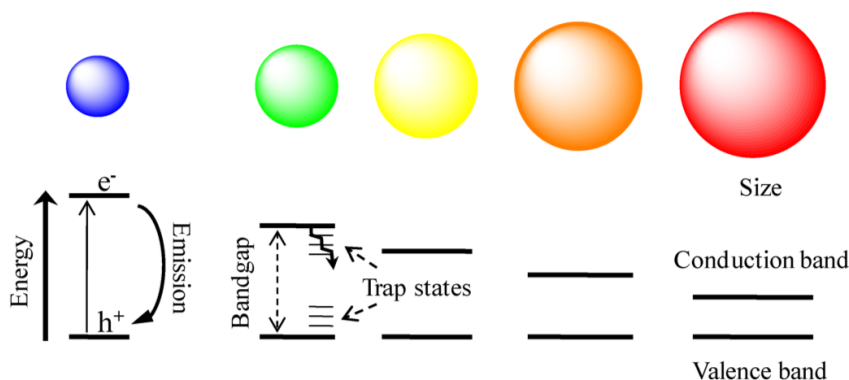
Figure 1.11: Illustration of size-tunable QDs and creation of the exciton (electronhole pair) upon photoexcitation followed by radiative recombination (fluorescence emission) or relaxation through trap states. Figure reproduced from Frasco *et al.*[59]

energy. This means that the formation of quantum dots can be monitored by UV-vis absorption spectroscopy and serves as a useful tool for their characterisation.[9,54]

1.3 Catalysis by Nanomaterials: The Boundary Between Homogeneous and Heterogeneous

The International Union of Pure and Applied Chemistry (IUPAC) has defined a catalyst as "a substance that increases the rate of a reaction without modifying the overall standard Gibbs energy change in the reaction."[60] A heterogeneous catalyst is where the phase of the catalyst differs from that of the reactants, whilst a homogeneous catalyst is in the same phase as the reactants. Heterogeneous catalysts are advantageous due to better recyclability and ease of scaling when compared to homogeneous catalysts. There are many different types of heterogeneous catalyst, from metal surfaces to zeolites and metal-organic frameworks and they have been applied in the fields of petrochemistry, organic synthesis and the processing of emissions.[61]

Nanomaterial based catalysts which have been rendered soluble in organic or aqueous solvents through the use of appropriate stabilising ligands or surface potential have been called quasi-homogeneous catalysts, as they are heterogeneous catalysts in solution.[62–64] These materials exist on the boundary between homogeneous and

heterogeneous catalysts and are the subject of much interest as the ligand sphere surrounding stabilised NPs has been found to influence their catalytic activity.[65,66] For example, there is a recent report of a colloidal HfO_2 nanocatalyst in which a carboxylic acid acts as both a stabilising ligand and a reactant. This exciting example of chemically driven ligand displacement preserves the colloidal stability of the heterogeneous catalyst and bypasses the tradeoff between colloidal stability and catalytic activity.[67]

1.3.1 Catalytic properties of metal oxide nanomaterials

The surface of a metal oxide consists of unsaturated metal cations and oxygen anions. As a rule, metal oxides with increasing ionic character display increasing Lewis acid-base behaviour. In this model, the metal cations act as Lewis acids whereas the oxygen anions act as Lewis bases. An example of Lewis acid behaviour can be found on TiO_2 surfaces where the presence of two types of Lewis acid sites has been observed and they have been attributed to five- and four-fold coordinated titanium cations situated on different faces.[68] Examples of strong Lewis base character on metal oxide surfaces can be seen in the case of the alkaline earth metal oxide catalysts such as MgO and CaO.[69–71]

The catalytic properties of metal oxides can also be related to the presence of surface defects. Although surface defects are indeed more reactive than other surface sites on oxides, they are not required for most surface sites to exhibit reactivity as most metal oxide surfaces have the presence of unsaturated metal cations and oxygen anions.[72]

1.3.2 Asymmetric catalysis

When a reaction creates a new stereogenic centre in a previously achiral molecule using achiral reagents, a racemic mixture is obtained because the transition states leading to these enantiomers are equal in energy. Therefore a synthesis, unless it uses enantiomerically pure starting materials/reagents or catalysts will give a mixture of
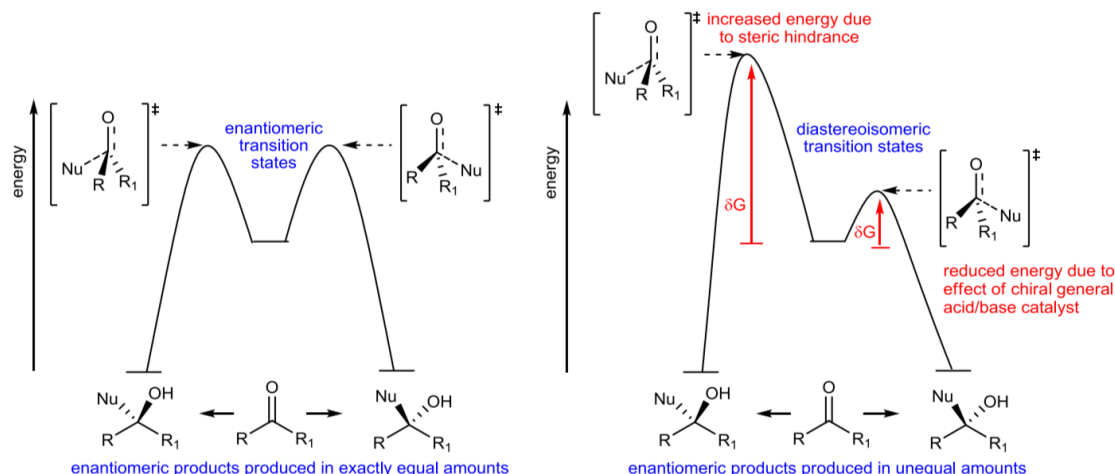
Figure 1.12: Effect of an asymmetric catalyst on transition state energies

enantiomers. If only one enantiomer is needed, resolution of enantiomers is possible but wasteful, as the other enantiomer is usually removed and thrown away. The aim of asymmetric catalysis is to change the reactions two enantiomeric transition states into transition states that are unequal in energy. This will lead to preferential formation of the desired product. An ideal asymmetric catalyst solves this problem via a twofold approach. Firstly, the energy of the transition state of the undesired enantiomer is made greater through steric crowding of one face of the substrate. As a result the starting molecule is hindered from approaching the undesired face of the substrate by the chiral orientation of the catalyst. Secondly, the energy barrier leading to the transition state of the desired enantiomer is lowered by activation of the reaction sites on the nucleophile and electrophile (Figure 1.12).

1.3.3 Asymmetric heterogeneous catalysis

As described in the previous section, asymmetric catalysis is the most attractive method for the production of isolated enantiomers and the field has had much success including a Nobel prize in 2001 for William S. Knowles and Ryoji Noyori "for their work on chirally catalysed hydrogenation reactions" and the other half to K. Barry Sharpless "for his work on chirally catalysed oxidation reactions".[73] However, despite such successes there in fact very few examples of asymmetric catalysts being employed in industry despite the obvious advantages of such a process. The reason

for this is not due to the efficacy of the reactions where high yields and e.e.'s and
yields have been demonstrated but rather the high costs of the ligand or metal.[62]

The use of an asymmetric heterogeneous catalyst would be an elegant solution for
the high costs of the metal/ligand as the catalyst could be separated and easily re-
cycled for further reactions. The development of successful heterogeneous catalysts
is complex however, and this is especially so for asymmetric heterogeneous cata-
lysts. The development of heterogeneous catalysts has a number of drawbacks and
challenges:

- Longer reaction times and higher catalyst loadings are generally needed for
  heterogeneous processes when compared to homogeneous ones

- The surface of a heterogeneous catalyst is not a trivial thing to model and
  leads to difficulties in catalyst design

- Creating an asymmetric environment around catalytic centres on a heteroge-
  neous catalyst is a harder task than when compared to a homogeneous one
  (this is related to the second point)

Well known examples of successful asymmetric heterogeneous catalysts include Pt
modified with cinchona alkaloids[74–77] and Raney nickel modified with tartaric acid,
having been employed in various asymmetric hydrogenations. Other early examples
of attempted asymmetric heterogeneous catalysts was the deposition of a metal or
metal oxide onto a chiral support, which led to poor enantioselectivities in hydro-
genation and dehydration reactions.[78] The disappointing results are understandable
when considering that only a fraction of the total surface metal atoms, those at the
metal/support interface, are in direct contact with the chiral support, whereas on
the rest of the surface sites the reaction may proceed without any stereochemical
control. The lesson from these attempts is that the chiral information must be in
close proximity to the catalytic sites (on the order of bond lengths) if one wants to
affect the stereochemical outcome of a catalytic transformation. This can be seen
in the templating of the Pt surface with cinchona alkaloids to produce a asymmet-
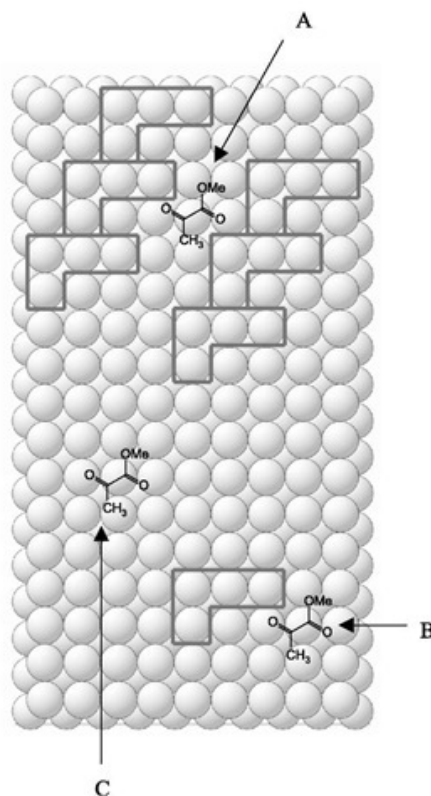
Figure 1.13: The L-shaped structure of the cinchona alkaloid creates three possible reaction sites when adsorbed on a surface. Sites A and B allow the methyl pyruvate to interact with the adsorbed modifier and thus promote enantioselective hydrogenation. Site C is achiral and does not promote enantioselective hydrogenation. Figure reproduced from Rampulla *et al.*[79]

ric catalyst. The adsorption of the cinchona alkaloid to the Pt-surface creates an L-shaped pocket which promotes asymmetric hydrogenation (Figure 1.13).[77,79]

Thus it has been successfully demonstrated enantioselective heterogeneous catalyst can be produced through the modification of a surface with an appropriate chiral ligand modifier. This approach has been shown to be applicable to colloidal metal oxide catalysts with a number of asymmetric organic transformations having been reported for MgO NPs modified with a chiral adsorbate.[70,71,80] This has also has been reported for an asymmetirc hydrosilylation catalysed by chirally modified CuO[81] and for magentically recoverable $CuFe_2O_4$ NPs[82] Asymmetric aldol reactions have also been demonstrated by chirally modified CuO[83] and ZnS[84] NPs, the latter of which when modified with L-proline which is proposed to form a reactive site with the

surface in a ligand-accelerated effect.

1.4   Aims of the Project

The main aims of this project are the development and characterisation of novel chiroptically-active metal oxide nanomaterials. These metal oxides included TiO_2, Mn_3O_4, ZnO and CeO_2. These nanomaterials are to be synthesised through a variety of "bottom-up" techniques, including sol-gel and hydrothermal approaches. As chiral component of these systems we plan to use amino acids and "priveliged" chiral ligands which have been previously employed in the field of asymmetric catalysis. The justification for the choice of each oxide is outlined below:

- Initially, a chiroptically-active TiO_2 nanomaterial is to be synthesised. TiO_2 has excellent photocatalytic properties that make the addition of a chiral component an attractive goal. In addition TiO_2 has demonstrated a very strong antibacterial activity.

- A chiroptically-active Mn_3O_4 is also chosen as it is a good candidate due to its catalytic properties and biomedical applications in anti-cancer therapy and as an MRI contrast agent.

- ZnO was chosen due to its unique properties such as light emission and potential biomedical applications. These have particular relevance to the fields of non-toxic quantum dots and anticancer therapy.

- Finally, CeO_2 is chosen as a component of a potential enantioselective catalyst due to its cooperative assembly with chiral PyBox-type ligands to form a basic catalytic site. A number of asymmetric base-catalysed organic transformations are to be investigated, including aldol and Michael reactions.

It is anticipated that these new chiroptically-active metal oxide nanomaterials could find potential uses as heterogeneous catalysts, as well as materials for biomedical and/or chiroptical sensing applications.

References

(1) Alivisatos, A *Science* **1996**, DOI: `10.1126/science.271.5251.933`.

(2) Geim, A. *Science* **2009**, DOI: `10.1126/science.1158877`.

(3) Gubin, S. P., *Magnetic Nanoparticles*, 2009.

(4) Koksharov, Y. A. In *Magnetic Nanoparticles*, 2009.

(5) Ma, N.; Ma, C.; Li, C.; Wang, T.; Tang, Y.; Wang, H.; Moul, X.; Chen, Z.; Hel, N. *Journal of nanoscience and nanotechnology* **2013**, DOI: `10.1166/jnn.2013.7525`.

(6) Sambur, J. B.; Chen, P. *Annual Review of Physical Chemistry* **2014**, DOI: `10.1146/annurev-physchem-040513-103729`.

(7) Yokel, R. A.; MacPhail, R. C. *Journal of Occupational Medicine and Toxicology* **2011**, DOI: `10.1186/1745-6673-6-7`.

(8) Fierro, J. L. G., *Metal Oxides: Chemistry and Applications*, 2006.

(9) Viswanatha, R.; Sapra, S.; Satpati, B; Satyam, P. V.; Dev, B. N.; Sarma, D. D. *Journal of Materials Chemistry* **2004**, DOI: `10.1039/b310404d`.

(10) Zhang, L.; Yin, L.; Wang, C.; lun, N.; Qi, Y.; Xiang, D. *The Journal of Physical Chemistry C* **2010**, *114*, 9651–9658.

(11) Zhang, L.; Yin, L.; Wang, C.; Lun, N.; Qi, Y. *ACS Applied Materials & Interfaces* **2010**, *2*, 1769–1773.

(12) Hu, J.; Chen, L.; Richards, R. In *Metal Oxide Catalysis*; Wiley-VCH Verlag GmbH & Co. KGaA: 2009, pp 613–663.

(13) Averill, B.; Eldredge, P., *Chemistry: Principles, Patterns, and Applications*, 2006.

(14) Housecroft, C. E.; Sharpe, A. G., *Inorganic Chemistry*, 2012.

(15)   Jackson, S. D.; Hargreaves, J. S. J., *Metal Oxide Catalysis*, 2009.

(16)   Brown Jr., G. E.; Henrich, V. E.; Casey, W. H.; Clark, D. L.; Eggleston, C.; Felmy, A.; Goodman, D. W.; Graetzel, M.; Maciel, G.; McCarthy, M. I.; Nealson, K. H.; Sverjensky, D. a.; Toney, M. F.; Zachara, J. M. *Chem. Rev.* **1999**, DOI: `10.1021/cr980011z`.

(17)   Barteau, M. A. *Chem. Rev.* **1996**, DOI: `10.1021/cr950222t`.

(18)   Iqbal, P.; Preece, J. A.; Mendes, P. M. In *Supramolecular Chemistry*, 2012.

(19)   Niederberger, M; Pinna, N, *Metal Oxide Nanoparticles in Organic Solvents*, 2009.

(20)   Livage, J; Henry, M; Sanchez, C *Progress in Solid State Chemistry* **1988**, *18*, 259–341.

(21)   Pasteur, L., *Researches on the Molecular Asymmetry of Natural Organic Products*, 14th ed.; Alembic Club: 1915.

(22)   Wang, Y.; Xu, J.; Wang, Y.; Chen, H. *Chemical Society Reviews* **2013**, *42*, 2930–2962.

(23)   Milton, F. P.; Govan, J.; Mukhina, M. V.; Gun'ko, Y. K. *Nanoscale Horizons* **2016**, *1*, 14–26.

(24)   How can we prepare a chiral compound? PART II. Resolution of racemates. , http://remotecat.blogspot.ie/2014/12/ Date accessed: 18/09/17.

(25)   Rodger, A.; Nordén, B, *Circular Dichroism and Linear Dichroism*; Oxford University Press: 1997.

(26)   Mukhina, M. V.; Maslov, V. G.; Baranov, A. V.; Fedorov, A. V.; Orlova, A. O.; Purcell-Milton, F.; Govan, J.; Gun'Ko, Y. K. *Nano Letters* **2015**, DOI: `10.1021/nl504439w`.

(27)   Liu, S.; Han, L.; Duan, Y.; Asahina, S.; Terasaki, O.; Cao, Y.; Liu, B.; Ma, L.; Zhang, J.; Che, S. *Nat Commun* **2012**, *3*, 1215.

(28)   Delclos, T.; Aimé, C.; Pouget, E.; Brizard, A.; Huc, I.; Delville, M.-H.; Oda, R. *Nano Letters* **2008**, *8*, 1929–1935.

(29)   Kobayashi, S.; Hamasaki, N.; Suzuki, M.; Kimura, M.; Shirai, H.; Hanabusa, K. *Journal of the American Chemical Society* **2002**, *124*, 6550–6551.

(30) Kawasaki, T.; Araki, Y.; Hatase, K.; Suzuki, K.; Matsumoto, A.; Yokoi, T.; Kubota, Y.; Tatsumi, T.; Soai, K. *Chemical Communications* **2015**, *51*, 8742–8744.

(31) Kim, J.; Lee, J.; Kim, W. Y.; Kim, H.; Lee, S.; Lee, H. C.; Lee, Y. S.; Seo, M.; Kim, S. Y. *Nat Commun* **2015**, *6*, DOI: `10.1038/ncomms7959`.

(32) Jin, R.-H.; Yao, D.-D.; Levi, R. *Chemistry – A European Journal* **2014**, *20*, 7196–7214.

(33) Duan, Y.; Liu, X.; Han, L.; Asahina, S.; Xu, D.; Cao, Y.; Yao, Y.; Che, S. *Journal of the American Chemical Society* **2014**, *136*, 7193–7196.

(34) Qian, Y.; Duan, Y.; Che, S. *Advanced Optical Materials* **2017**, *5*, 1601013–n/a.

(35) Ma, W.; Kuang, H.; Wang, L.; Xu, L.; Chang, W.-S.; Zhang, H.; Sun, M.; Zhu, Y.; Zhao, Y.; Liu, L.; Xu, C.; Link, S.; Kotov, N. A. *Scientific Reports* **2013**, *3*, 1934.

(36) Keller, D.; Bustamante, C. *The Journal of Chemical Physics* **1986**, *84*, 2972–2980.

(37) Dick, B. *ChemPhysChem* **2011**, *12*, 1578–1587.

(38) Matsukizono, H.; Jin, R.-H. *Angewandte Chemie International Edition* **2012**, *51*, 5862–5865.

(39) Gedanken, A. *Ultrasonics Sonochemistry* **2004**, *11*, 47–55.

(40) Gabashvili, A.; Major, D. T.; Perkas, N.; Gedanken, A. *Ultrasonics Sonochemistry* **2010**, *17*, 605–609.

(41) Chen, C.; Shi, H.; Zhao, G. *The Journal of Physical Chemistry C* **2014**, *118*, 12041–12049.

(42) Seung-Woo, L.; Izumi, I.; Toyoki, K. *Chemistry Letters* **2002**, *31*, 678–679.

(43) Switzer, J. A.; Kothari, H. M.; Poizot, P.; Nakanishi, S.; Bohannan, E. W. *Nature* **2003**, *425*, 490–493.

(44) Matsukizono, H.; Jin, R.-H. *Angewandte Chemie International Edition* **2012**, *51*, 5862–5865.

(45) Govorov, A. O.; Gun'ko, Y. K.; Slocik, J. M.; Gerard, V. A.; Fan, Z.; Naik, R. R. *Journal of Materials Chemistry* **2011**, *21*, 16806–16818.

(46) Abdulrahman, N. A.; Fan, Z; Tonooka, T.; Kelly, S. M.; Gadegaard, N.; Hendry, E.; Govorov, A. O.; Kadodwala, M. *Nano Letters* **2012**, *12*, 977–983.

(47)   Moshe, A. B.; Markovich, G. *Israel Journal of Chemistry* **2012**, *52*, 1104–1110.

(48)   Tohgha, U.; Deol, K. K.; Porter, A. G.; Bartko, S. G.; Choi, J. K.; Leonard, B. M.; Varga, K.; Kubelka, J.; Muller, G.; Balaz, M. *ACS Nano* **2013**, *7*, 11094–11102.

(49)   Ben-Moshe, A.; Teitelboim, A.; Oron, D.; Markovich, G. *Nano Letters* **2016**, DOI: `10.1021/acs.nanolett.6b03143`.

(50)   Ray, K.; Petrenko, T.; Wieghardt, K.; Neese, F. Joint spectroscopic and theoretical investigations of transition metal complexes involving non-innocent ligands., 2007.

(51)   Frederick, M. T.; Amin, V. A.; Weiss, E. A. *Journal of Physical Chemistry Letters* **2013**, DOI: `10.1021/jz301905n`.

(52)   Razzaque, S.; Hussain, S. Z.; Hussain, I.; Tan, B. Design and utility of metal/metal oxide nanoparticles mediated by thioether end-functionalized polymeric ligands., 2016.

(53)   Ben-Moshe, A.; Wolf, S. G.; Sadan, M. B.; Houben, L.; Fan, Z.; Govorov, A. O.; Markovich, G. *Nat Commun* **2014**, *5*, DOI: `10.1038/ncomms5302`.

(54)   Moloney, M. P.; Govan, J.; Loudon, A.; Mukhina, M.; Gun'ko, Y. K. *Nat. Protocols* **2015**, *10*, 558–573.

(55)   Moloney, M. P.; Gun'ko, Y. K.; Kelly, J. M. *Chem. Commun.* **2007**, DOI: `10.1039/B704636G`.

(56)   Delgado-Pérez, T.; Bouchet, L. M.; De La Guardia, M.; Galian, R. E.; Pérez-Prieto, J. *Chemistry - A European Journal* **2013**, DOI: `10.1002/chem.201300875`.

(57)   Gao, F.; Ma, S.; Xiao, X.; Hu, Y.; Zhao, D.; He, Z. *Talanta* **2017**, DOI: `10.1016/j.talanta.2016.10.091`.

(58)   Martynenko, I. V.; Kuznetsova, V. A.; Litvinov, I. K.; Orlova, A. O.; Maslov, V. G.; Fedorov, A. V.; Dubavik, A; Purcell-Milton, F; Yu, K. G.; Baranov, A. V. *Nanotechnology* **2016**, *27*, 75102.

(59)   Frasco, M. F.; Chaniotakis, N. Semiconductor quantum dots in chemical sensors and biosensors., 2009.

(60)   A. D. McNaught, A., *IUPAC Compendium of Chemical Terminology, 2nd ed.* Blackwell Scientific Publications, Oxford: 1997.

(61)   Fechete, I.; Wang, Y.; Védrine, J. C. *Catalytic Materials for Energy: Past, Present and Future* **2012**, DOI: `10.1016/j.cattod.2012.04.003`.

(62)   Weckhuysen, B. *Angewandte Chemie International Edition* **2007**, *46*, 492.

(63)   Bönnemann, H.; Braun, G.; Brijoux, W.; Brinkmann, R.; Tilling, A.; Seevogel, K.; Siepen, K. *Journal of Organometallic Chemistry* **1996**, DOI: `10.1016/0022-328X(96)06273-0`.

(64)   Rangheard, C.; Fernandez, C. d. J.; Phua, P.-H. *Dalton transactions (Cambridge, England : 2003)* **2010**, DOI: `10.1039/c001226b`.

(65)   Wu, B.; Zheng, N. Surface and interface control of noble metal nanocrystals for catalytic and electrocatalytic applications., 2013.

(66)   Huang, J.; Haruta, M., *Bridging Heterogeneous and Homogeneous Catalysis*, 2014.

(67)   De Roo, J.; Van Driessche, I.; Martins, J. C.; Hens, Z. *Nat Mater* **2016**, *15*, 517–521.

(68)   Hadjiivanov, K; Lamotte, J; Lavalley, J.-C. *Langmuir* **1997**, DOI: `10.1021/la962104m`.

(69)   Choudary, B. M.; Kantam, M. L.; Ranganath, K. V. S.; Mahendar, K.; Sreedhar, B. *Journal of the American Chemical Society* **2004**, *126*, 3396–3397.

(70)   Kantam, M. L.; Ranganath, K. V. S.; Mahendar, K.; Chakrapani, L.; Choudary, B. M. *Tetrahedron Letters* **2007**, *48*, 7646–7649.

(71)   Choudary, B. M.; Ranganath, K. V. S.; Pal, U.; Kantam, M. L.; Sreedhar, B. *Journal of the American Chemical Society* **2005**, *127*, 13167–13171.

(72)   Idriss, H.; Barteau, M. A. *Advances in Catalysis* **2000**, DOI: `10.1016/S0360-0564(02)45016-X`.

(73)   The Nobel Prize in Chemistry 2001., 2014.

(74)   Blaser, H. U.; Studer, M. Cinchona-modified platinum catalysts: From ligand acceleration to technical processes., 2007.

(75)   Studer, M.; Burkhardt, S.; Blaser, H.-U. *Chemical Communications* **1999**, DOI: `10.1039/A905113I`.

(76)   Blaser, H. U.; Jalett, H. P.; Wiehl, J *Journal of Molecular Catalysis* **1991**.

(77)   Sutherl, I. M.; Ibbotson, A; Moyes, R. B.; Wells, P. B. *Journal of Catalysis* **1990**, *125*, 77 –88.

(78)   Mallat, T.; Orglmeister, E.; Baiker, A. Asymmetric catalysis at chiral metal surfaces., 2007.

(79)   Rampulla, D.; Gellman, A. Enantioselectivity on Surfaces with Chiral Nanostructures., 2004.

(80)   Choudary, B. M.; Kantam, M. L.; Ranganath, K. V. S.; Mahendar, K.; Sreedhar, B. *Journal of the American Chemical Society* **2004**, *126*, 3396–3397.

(81)   Kantam, M. L.; Laha, S.; Yadav, J.; Likhar, P.; Sreedhar, B; Choudary, B. *Advanced Synthesis & Catalysis* **2007**, *349*, 1797–1802.

(82)   Kantam, M. L.; Yadav, J.; Laha, S.; Srinivas, P.; Sreedhar, B.; Figueras, F *The Journal of Organic Chemistry* **2009**, *74*, 4608–4611.

(83)   Kantam, M. L.; Ramani, T.; Chakrapani, L.; Kumar, K. V. *Tetrahedron Letters* **2008**, *49*, 1498–1501.

(84)   Shah, E.; Soni, H. P. *RSC Advances* **2013**, *3*, 17453–17461.

Chapter 2

Chiroptically-Active TiO$_2$ Nanoparticles

2.1 Introduction

Titanium dioxide is one of the most investigated metal oxides due to its unique properties, chemical stability and the favourable positions of its valence and conduction bands. TiO$_2$ nanomaterials have found applications in "self-cleaning" glass, solar cells, gas sensors and in heterogeneous catalysis, to name but a few.[1] TiO$_2$ has three crystalline phases; anatase, rutile and brookite, of which anatase and rutile are the most important for catalytic applications. This is due most in part to their band gaps of 3.2 eV for anatase and 3.0 eV for rutile, both of which are larger than the corresponding band gap for brookite.[2] Both anatase and rutile have tetragonal-based crystal structures (Figure 2.1). Of the two phases, rutile is the most thermodynamically stable, although anatase becomes the most stable phase at crystallite sizes less than 14 nm.[3]

Anatase is widely regarded as a superior photocatalyst to rutile, owing to its larger band gap.[4] A mixture of the two phases however, can exhibit greater photocatayltic activity than pure anatase. This is due to favourable valence and conduction band alignments at the interface between the two phases[5]. The basic mechanism of TiO$_2$
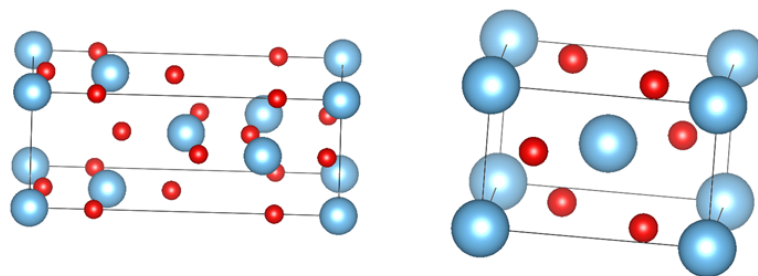
Figure 2.1: The unit cell of anatase (left) and rutile (right). Titanium atoms are marked blue whereas oxygen atoms are marked red.

photocatalysis can be represented by a simple band gap model (Figure 2.2). The band gap is defined as the energy difference (ΔE_g) between the valence and conduction bands.[6] When energy greater than ΔE_g is applied to the semiconductor surface such as TiO_2, valence band electrons are promoted to the conduction band, creating electron-hole pairs (1). Migration of the pairs to the semiconductor surface (2) allows the occurrence of redox reactions with adsorbates with suitable redox potentials (3). Oxidation will occur if the redox potential of the valence band is more positive than that of the adsorbates. Similarly, conduction band electrons can reduce adsorbed species if their redox potential is more negative than that of the adsorbates. The most likely outcome of the formation of electron–hole pairs is their recombination, with subsequent release of thermal energy and/or light (4).
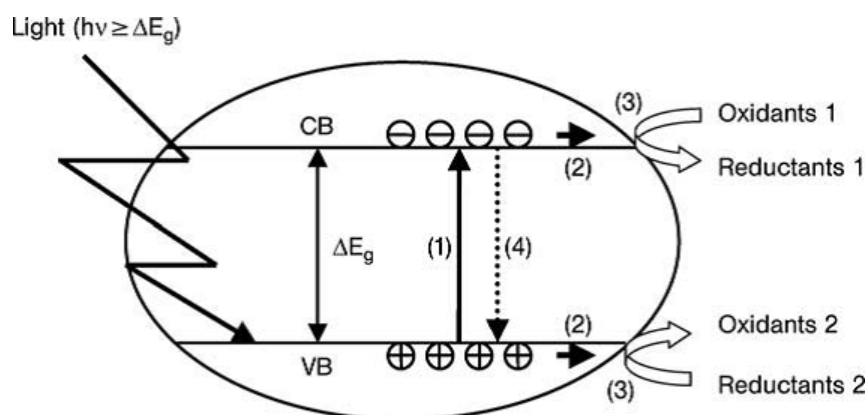
Figure 2.2: Diagram of the band gap model. (1) Photoinduced electron-hole creation; (2) charge migration to the surface; (3) redox reactions; (4) recombination. Figure reproduced from Wells et al.[2]

Recombination occurring within the same timescale as the redox processes being pro-

$$\mathrm{e}_{CB}^{-} + h_{tr}^{+} = hv_{green} \qquad (1)$$

$$\mathrm{e}_{deep}^{-} + h_{VB}^{+} = hv_{red} \qquad (2a)$$

$$\mathrm{e}_{shallow}^{-} + h_{VB}^{+} = hv_{blue} \qquad (2b)$$

Scheme 2.1: Types of TiO$_2$ luminescence centres

moted reduces photocatalytic activity considerably. For electron–hole pairs, charge separation can be a vital factor for catalytic activity. Defects can play an important role in "trapping" these charge carriers and preventing recombination from taking place. Examples of defects include oxygen vacancies in nanostructured oxides, dopants, or impurities.[2] Due to their photocatalytic properties, TiO$_2$ nanomaterials have also found application in promoting a wide range of selective organic transformations.[7] Examples of these reactions include photocatalytic oxidations,[8–11] photocatalysed degradation of organic dyes[12] and the enantioselective α-oxyamination of aldehydes.[13] It has also been reported that TiO$_2$ films exhibit a strong antimicrobial effect upon irradiation with UV light.[14] These applications present an array of potential avenues of further research upon the synthesis of a TiO$_2$ nanomaterial which has an appropriate chiral surface arrangement, as these photocatalytic reactions may be modified to include a chiral component.

Recently TiO$_2$ has begun to attract considerable interest due to its luminescent properties. TiO$_2$ may exhibit photo-luminescent emission due to the presence of a defective surface.[15,16] These surface defects have been suggested in the literature to be surfaces such as the [001] facet, with a high proportion of penta-coordinated Ti^{3+} atoms,[17] or due to oxygen vacancies.[18–21] These defective sites may serve as electron traps or as positively charged holes, either situated near the conduction or valence bands respectively. These surface states act as luminescent centres for different types of luminescence as shown in Scheme 2.1.

There are 3 types of luminescence that can be exhibited by the different types of

TiO$_2$ defective surface centres. Type 1 luminescence is green and is due to the presence of a positively charged trap state positioned near the valence band. Type 2 a) and b) luminescence is thought to be due to the presence of deep or shallow electron trap states. The different types of luminescence are summarised in Figure 2.3.
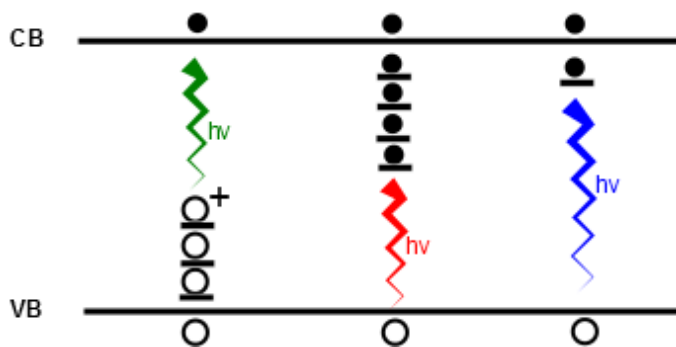
Figure 2.3: Types of luminescence associated with defective surface centres of TiO$_2$

By carefully controlling the surface chemistry of TiO$_2$, it is theoretically possible to prepare surfaces that selectively quench or enhance each of the three types of luminescence. For instance, the [001] surface of anatase has a higher number of penta-coordinated Ti-sites when compared with the more stable [101] surface. This surface is conventionally prepared using F$^-$ anions during synthesis, the role of these anions being to stabilise the high energy penta-coordinate Ti-atoms present. The F$^-$ caps the high energy Ti-atoms on the surface, forming a six-coordinate Ti species. Annealing the [001] surface removes the F$^-$, and increases the PL intensity of the surface.[22] Conversely, it is possible to quench this red luminescence through the addition of valence-band hole scavengers such as EtOH. It has been shown that EtOH binds more preferentially to the [101] surface than compared to the [001]. In this case, scavenging of the VB holes quenches the red emission and leads to radiative recombination of CB electrons with trapped holes dominating the spectrum. This causes a Type 1 green emission.[23] Thus, according to the current state of the art it is possible to control the luminescence of TiO$_2$ NCs by controlling the surface chemistry. Therefore an appropriate choice of a ligand that has both a favourable influence on the surface defective states as well as chiral properties may provide an avenue towards preparing a chiral TiO$_2$ nanomaterial with different wavelengths of

emission. The main aim of this part of our work is to develop new chiroptically-active TiO_2 based nanomaterials and investigate their properties.

2.2 Results and Discussion

2.2.1 Chiral and luminescent TiO_2 nanoparticles

For the initial synthesis of chiral and luminescent TiO_2 nanoparticles, a non-aqueous solvent controlled synthesis was chosen. This synthesis was first reported by Niederberger *et al.* and had been used to produce crystalline and luminescent TiO_2 NCs in one synthetic step.[24] This synthetic method was chosen because most hydrolytic syntheses of TiO_2 nanoparticles result in products that are amorphous in nature and require a post-synthesis crystallisation step. This crystallisation involves annealing or a hydrothermal treatment, and drastically changes the surface structure of the TiO_2. This step has been shown to be detrimental to the formation of chiral metal oxide NPs as seen in later in this chapter. An initial investigation was carried out on a number of different TiO_2 precursors as well as a number of chiral capping ligands. The results are summarised in Table 2.1.
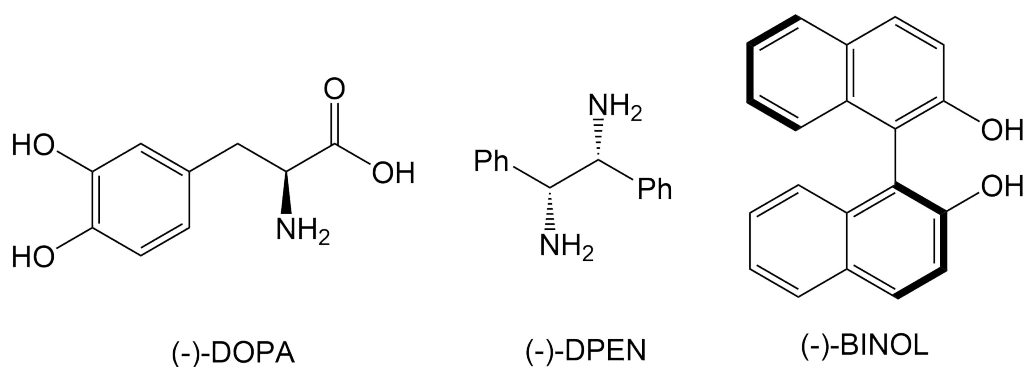
Figure 2.4: Chiral capping ligands

TiO$_2$ Precursor	Chiral Ligand	Optical Activity
TiCl$_4$	(-)-DOPA	No
TiCl$_4$	(-)-DPEN	**Yes**
TiCl$_4$	(-)-BINOL	No
Ti^{i}OPr$_4$	(-)-DOPA	No
Ti^{i}OPr$_4$	(-)-DPEN	No
Ti^{i}OPr$_4$	(-)-BINOL	No
Ti^{i}OBu$_4$	(-)-DOPA	No
Ti^{i}OBu$_4$	(-)-DPEN	No
Ti^{i}OBu$_4$	(-)-BINOL	No

Table 2.1: Initial investigations of the synthesis of chiral and luminescent TiO$_2$

After the initial investigations, it was found that TiCl$_4$ as the TiO$_2$ precursor in combination with (1R,2R)-(+)-1,2-diphenylethylenediamine (DPEN) or (1S,2S)-(-)-1,2-DPEN as the chiral capping agent gave a material that was both luminescent as well as chiroptically-active in nature.

TEM as well as STEM images of the TiO$_2$ nanoparticles obtained from this synthetic protocol (Figure 2.5) demonstrate that the sample is composed of nanostructures with dendritic morphology that range in size between 30 and 50 nm. These structures are made up of aggregates of smaller TiO$_2$ nanorods 3–4 nm in diameter, which can be clearly seen from the images obtained through TEM. Dynamic light scattering measurements (see Figure 2.7) also indicate that the nanoparticles exist as these large aggregates in solution and not the smaller nanorods that can be seen in the TEM images. It is clear that the nanoparticles are crystalline in nature due to the presence of lattice fringes in the TEM images. The XRD pattern also agrees with this analysis and shows that the nanoparticles are phase pure anatase as can be seen in Figure 2.6.

Figure 2.8 displays the circular dichroism spectra of both the (+) and (-)-DPEN capped samples. These results show that the nanoparticles are chiral in nature as the expected mirror image spectrum is obtained. The large peak at 230 nm can be
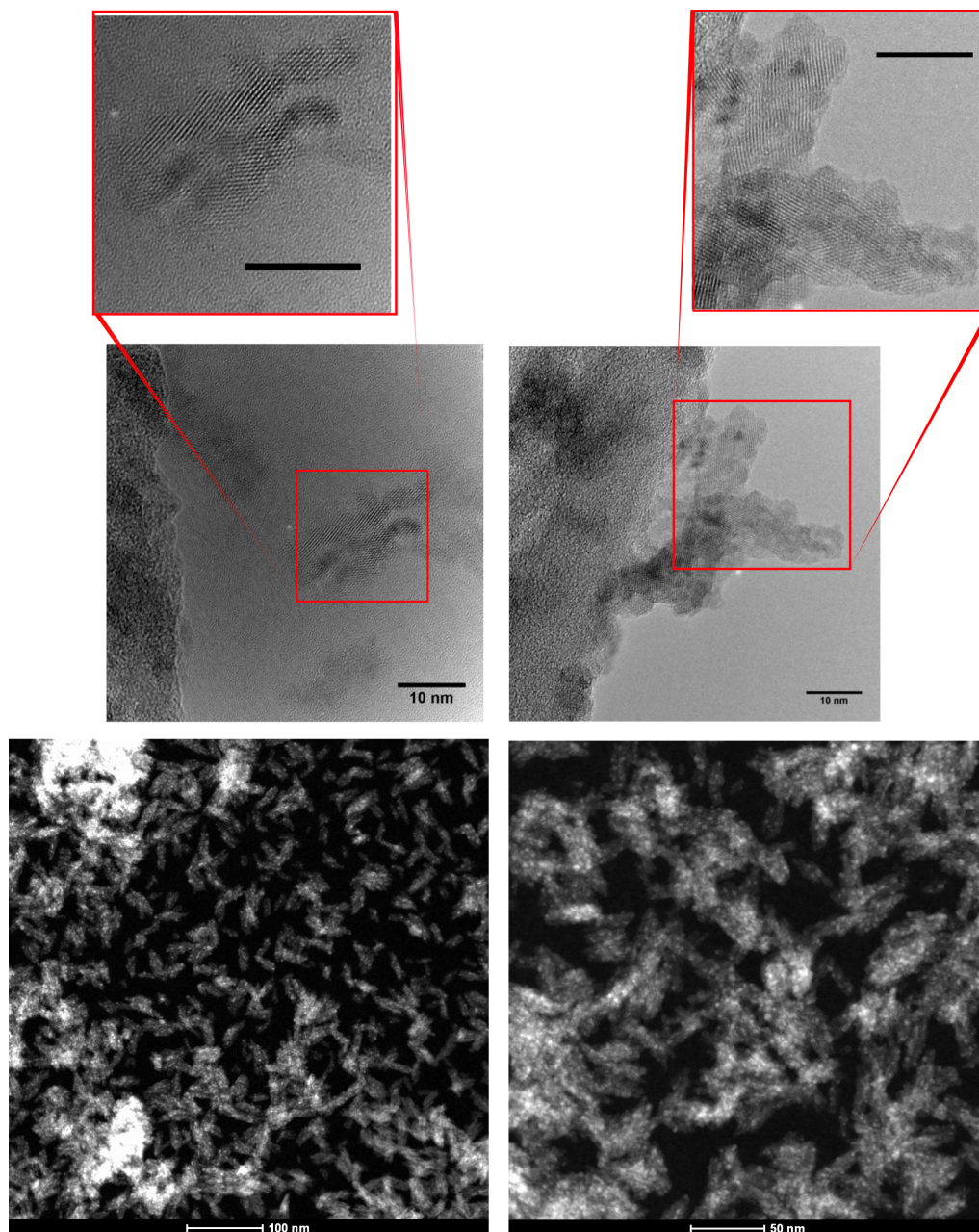
Figure 2.5:   TEM (top) and STEM (bottom) images of (+)-diphenylethylenediamine capped nanoparticles. Black scale bars are 10 nm in length
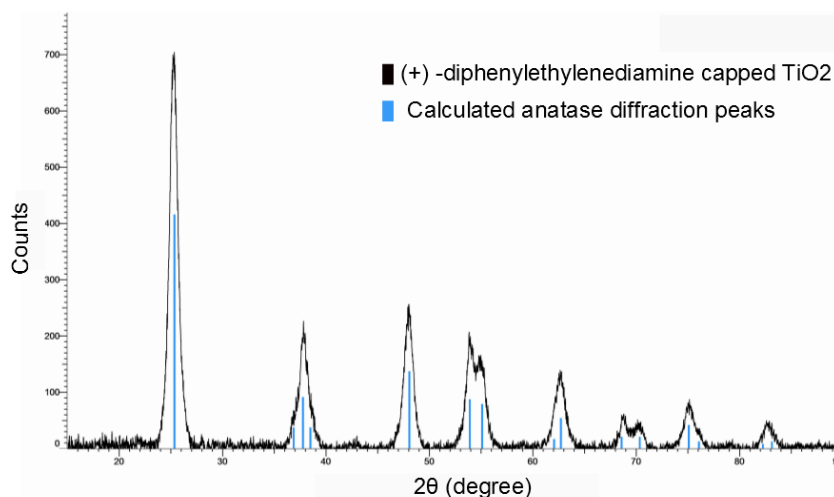
Figure 2.6: XRD pattern of (-)-diphenylethlenediamine capped nanoparticles (black) and calculated anatase peaks (blue)
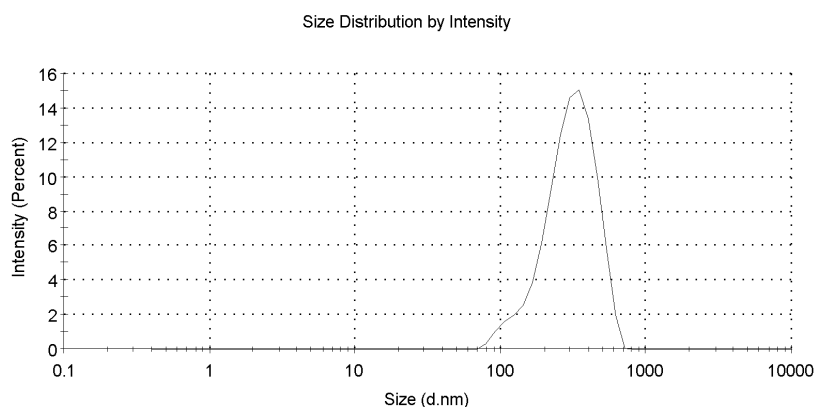
Figure 2.7: Dynamic light scattering measurement of (+)-DPEN capped TiO_2 nanoparticles

attributed to the presence of the organic capping ligand, as it appears in its characteristic region of the spectrum (Figure 2.9). It is interesting to note that the (+) and (-)-DPEN peaks between 256 and 268 nm are not present in the circular dichroism spectra of the chiral TiO_2. This clearly indicates that the circular dichroism is not due to the presence of free ligand in solution.

The broad peak which begins at 350 nm can be assigned as originating from the inorganic component of the ligand-capped TiO_2 nanoparticles, as it is in the expected band-edge region for TiO_2. The origin of this optical activity can be explained by a ligand-induced effect caused by the overlap of the chiral ligand HOMOs (highest
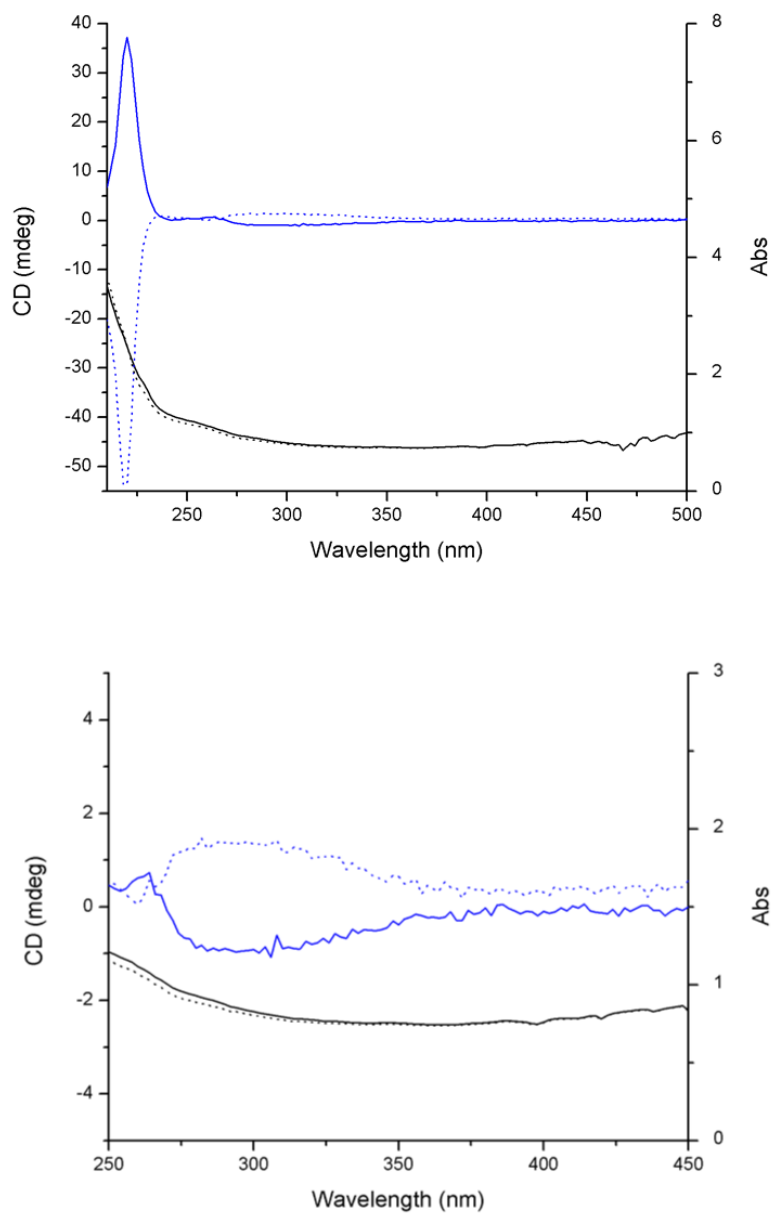
Figure 2.8: Circular dichrosim spectra (blue) and absorption spectra (black) of (+)-DPEN (solid) and (-)-DPEN (dotted) capped TiO2 nanoparticles
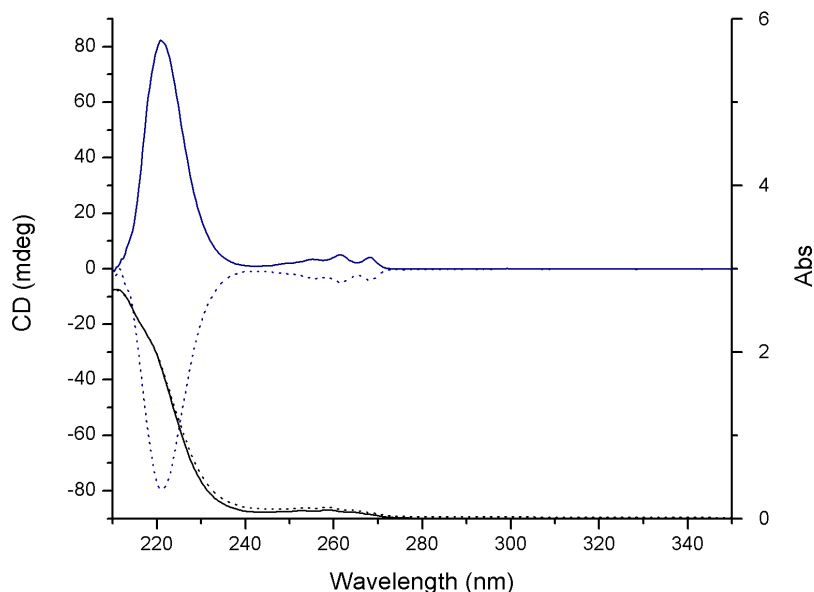
Figure 2.9: Circular Dichrosim spectra (blue) and absorption spectra (black) of (+)
–DPEN (solid) and (-)-DPEN (dotted)

occupied molecular orbital) with the TiO_2 valence band states. This phenomenon
is known to occur in II–VI QDs capped by chiral capping ligands.[25–27] A signal in
this region is not observed in the case of the free ligand, providing further proof
that this signal originates from the inorganic TiO_2 nanoparticles and not the chiral
capping ligand. There is a Cotton effect present at ~263 nm, which is the same region
as the distinct peak found in the normalised absorption spectrum (Figure 2.12).
A Cotton effect is characteristically seen passing through zero at the wavelength
at which the maximum absorption appears,[25] the circular dichroism results when
viewed in tandem with the normalised absorption spectrum in Figure 3 confirms the
assignment of the inorganic component of the ligand-capped TiO_2 nanoparticles.

Upon heat treatment of the nanoparticles at 300 °C for 1 hour to remove the chiral
ligand from the surface, the circular dichroism signals and any optical activity dis-
appeared (Figure 2.10). This shows that the circular dichroism signal is entirely due
to the presence of the ligand on the surface and the interaction of chiral ligand and
ligands orbitals with the QD valence band states and not caused by a chiral "surface
imprint" or chiral defects in the inorganic TiO_2 nanoparticles. An investigation was
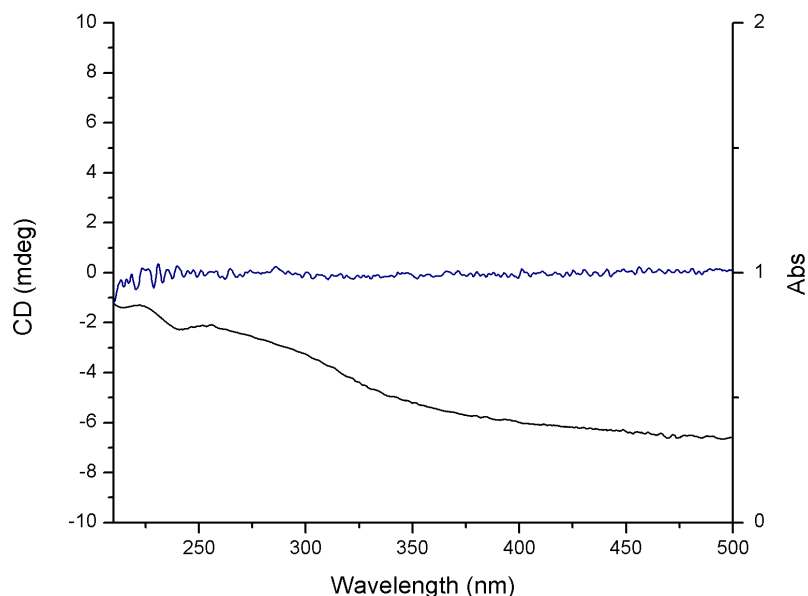
Figure 2.10: Circular Dichrosim spectrum (blue) and absorption spectrum (black) of (+) –DPEN capped TiO2 nanoparticles after heat treatment at 300 ºC for 1 hour

also carried out relating the dependence of the magnitude of the CD signal to the number of equivalents of DPEN used in the reaction. The results of this investigation is shown in Figure 2.11. The graph is presented as a series of normalised CD spectra. The convention is to refer to these normalised spectra as g-factor spectra and this convention shall be adhered to hereafter in this text. The results of these investigations show that as the number of equivalents of chiral ligand is reduced, so too does the strength of the g-factor signal. This is hardly surprising, but it does show the importance of concentration of chiral ligand on the results of the reaction. The g-factor response is non-linear with respect to the concentration of chiral ligand used in this reaction. Careful consideration must be given to the amount of chiral ligand used in a reaction if one aims to prepare a chiral TiO_2 NPs by this method.

The absorption spectra of TiO_2 in THF solution (Figure 2.12) shows onset at 600 nm, with a more pronounced absorption occurring below 350 nm with a distinct peak found at 263 nm. The origin of the longer wavelength absorption (past 400 nm), is assigned as occurring due to a combination of scattering and interband gap states. The peak at 265 nm can be assigned to a quantum confined nanostructure of
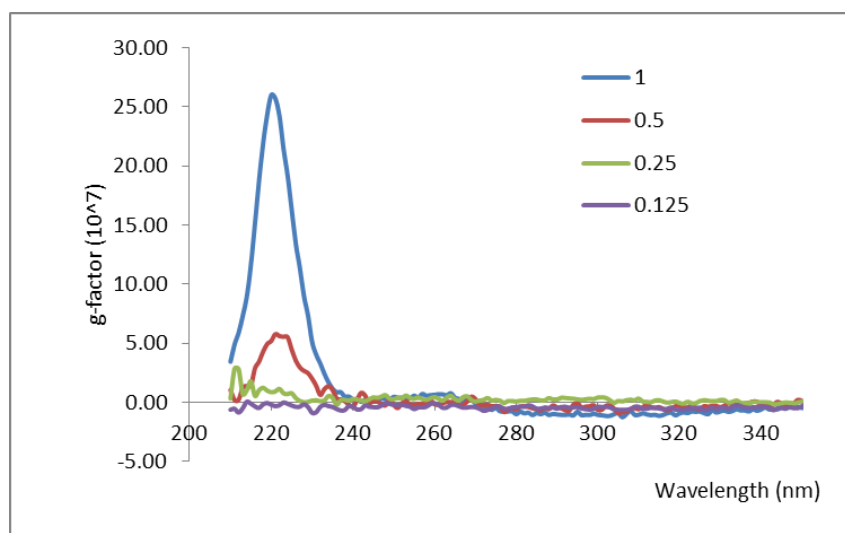
Figure 2.11: g-factor spectra comparing TiO_2 samples prepared using different molar equivalents of (+)-DPEN (0.125, 0.25, 0.5 and 1.0)

TiO_2 indicating that at least one dimension of our particles is on the order of 1–10 nm,[28] and therefore comparable to the Bohr radius of TiO_2 which is 1.5 nm.[29]
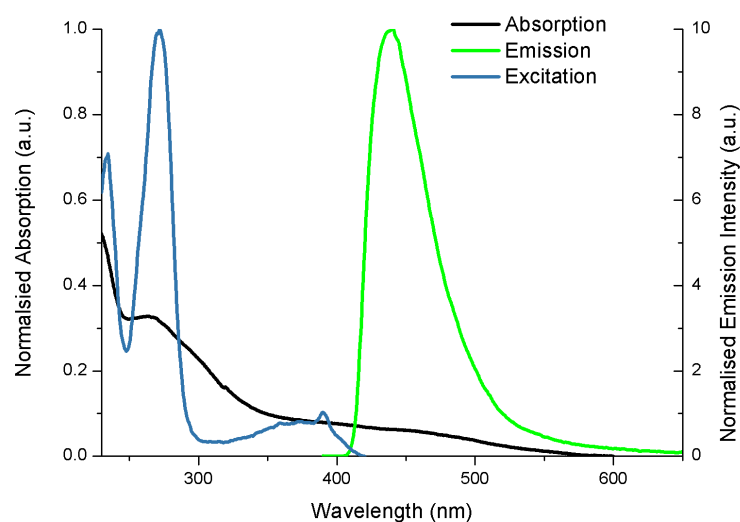
Figure 2.12: Absorption, emission, and excitation spectra of (+)-DPEN capped TiO_2 nanoparticles

Photoluminescence spectroscopy was used for analysis of the produced TiO_2 samples in THF solution at room temperature with the resulting spectra shown in Figure 2.12. In these spectra, a relatively broad photoluminescence peak centred upon 439.5 nm with a full-width half max of 52.6 nm can be seen. This visible luminescence

band originates from a gap state at 0.7 eV below the conduction band due to oxygen vacancies associated with Ti^{3+} in anatase TiO_2.[30,31] The quantum yield of the TiO_2 nanoparticles was determined to be 3.5 % in THF solution when excited at 261 nm and was determined by the relative approach, using quinine sulfate dihydrate dye in 0.105 M $HClO_4$ in water as our standard which has a quantum yield of 60.9 %.[32] This quantum yield compares favourably with examples in literature measured at room temperature, which range generally from 1.6 to 0.25 and even as low as 0.05 %,[19,33,34] though a single report does exist claiming quantum yields up to 20 %.[28] The dependence of the photoluminescence spectra on the excitation wavelength in the range from 240 to 320 nm was investigated (Figure 2.13). There was no distinct change in peak shape, while a strong change in intensity was discovered; therefore we carried out excitation spectra analysis. The excitation spectra of the TiO_2 particles in THF solution show a sharp peak at 271 nm, and correlates with the distinct peak found in the absorption spectra of the sample. We also find another notable area of excitation at lower energy, between 300 and 400 nm which then ends below 420 nm (3.2 eV) which is the bulk band gap of anatase TiO_2,[35] indicating absorption below this energy shows no correlation to the luminescence of these particles, which further points toward absorption spectra below this energy being due to scatter and inter-band gap states.

The luminescent lifetimes of the TiO_2 in THF solution (Figure 2.14) were then examined, exciting the sample at 261 nm and measuring the lifetime for the emission peak at 440 nm. Anthracene was used as a fluorescence lifetime standard in cyclohexane using a standard lifetime of 5.3 ± 0.1 ns[36] so as to deconvolute the instrument response function. The TiO_2 NPs lifetime which was fit using a biexponential, showing a lifetime of 6.30 ± 0.029 and 13.62 ± 0.079 ns with a relative amplitude of 79.7 % and 20.3 %. Though sub-nanosecond lifetimes for TiO_2,[18,37] have been reported, these are associated with higher energy luminescence, while the emission presented here is also of a much lower energy of 2.81 eV. It has therefore been assigned as a shallow trap state emission as reported in literature,[19] and which is commonly found to display much longer luminescence lifetimes.[18]
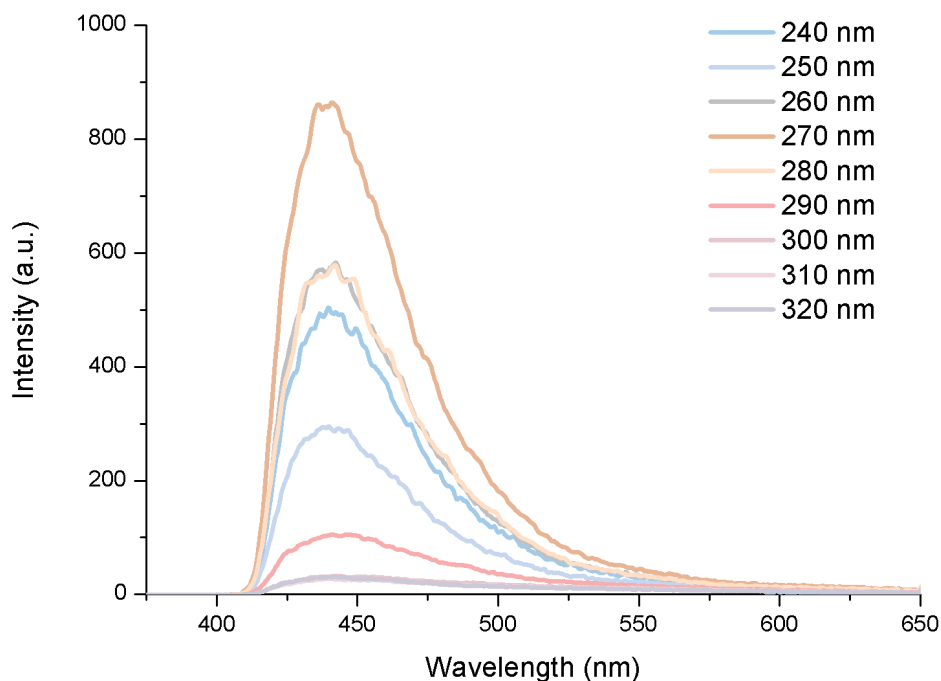
Figure 2.13: Excitation spectra of (+)-DPEN capped TiO_2 nanoparticles

Circularly polarised luminescence (CPL) measurements were also carried out on a sample of the (+)-DPEN capped TiO_2 NPs. CPL is a luminescence phenomenon that resulting from the differential emission intensity of right and left circularly polarised light. There is a growing interest toward the development of systems capable of circularly polarised emission due to their potential applications in sensors, asymmetric synthesis as well as display and optical storage devices.[25,38–40]The results of the measurements shown in Figure 2.15 indicate that the chiral TiO_2 NPs do not exhibit any CPL, or have a very low CPL that cannot be distinguished from the noise levels of the instrument as the quantum yield of the NPs is not sufficiently high enough for successful detection.
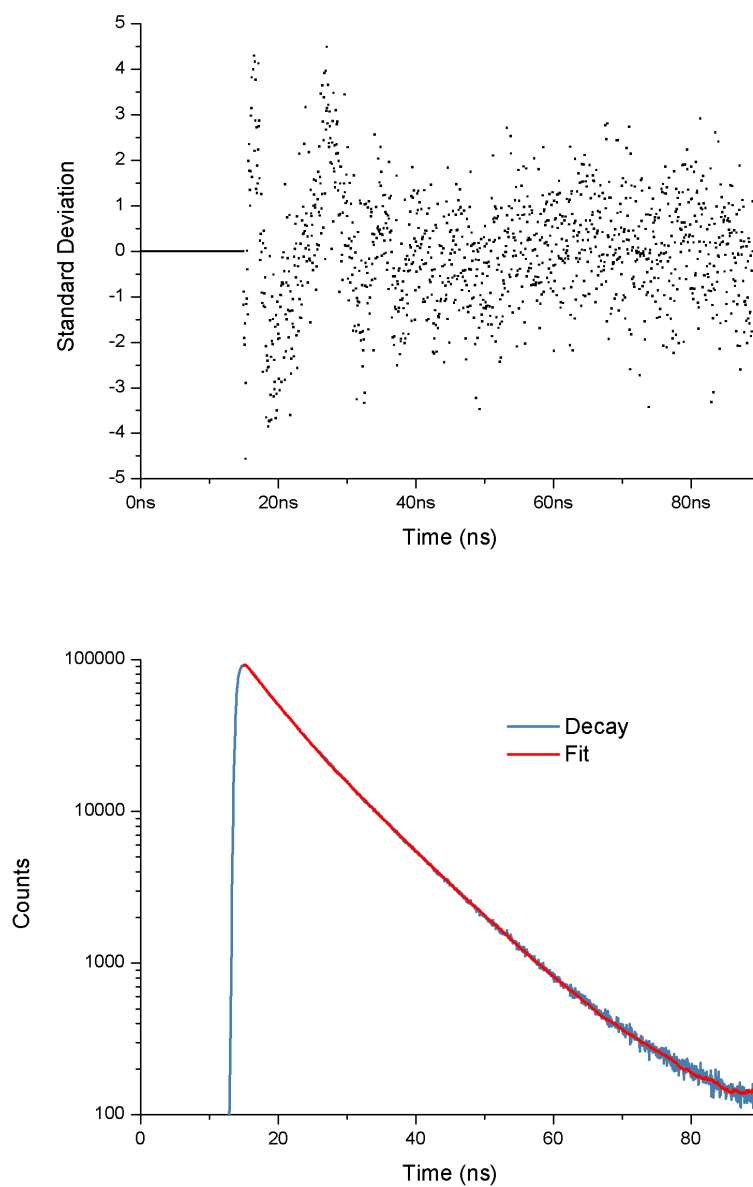
Figure 2.14: Luminescent lifetime of (+)-DPEN capped TiO$_2$ nanoparticles (bottom) and calculated residuals (top)
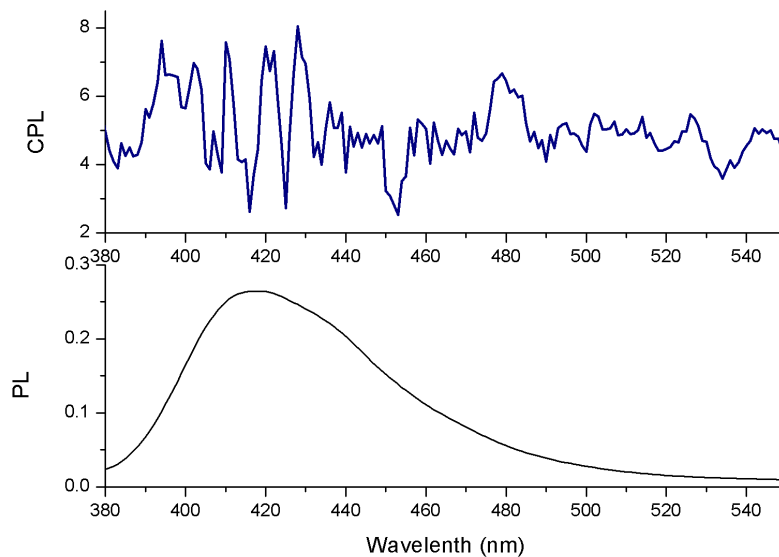
Figure 2.15: CPL spectrum (top) and PL spectrum (bottom) of (+)-DPEN capped TiO_2 NCs

2.2.2   Phase transfer method for the preparation of chiral TiO_2 NCs

Another approach for the preparation of chiral TiO_2 NPs is the phase transfer method. The phase-transfer method[41,42] is an attractive approach for the formation of chiral TiO_2 NPs as initial synthesis in organic solvents can provide a great degree of control over the size, morphology and crystallinity of the TiO_2 NPs. The prepared NPs can then be modified in a convenient post-synthesis step to produce aqueous-soluble TiO_2 NPs. The use of the phase-transfer method also allows for the facile screening of a number of different ligands, when compared to functionalising the NPs *in situ* during the synthesis. This approach allows one to compare the resulting chiral and luminescent properties of a number of different TiO_2 NPs, based only upon differences in their respective ligand spheres. TiO_2 nanorods were first prepared by a previously reported synthetic procedure.[43] The as-prepared nanoparticles are capped with oleic acid (OA) and are soluble in organic solvents such as hexane and chloroform. The transmission electron microscopy (TEM) images in Figure 2.16 indicate that the sample is composed of nano-rods of length 12 ± 4 nm and 3 ± 1 nm.
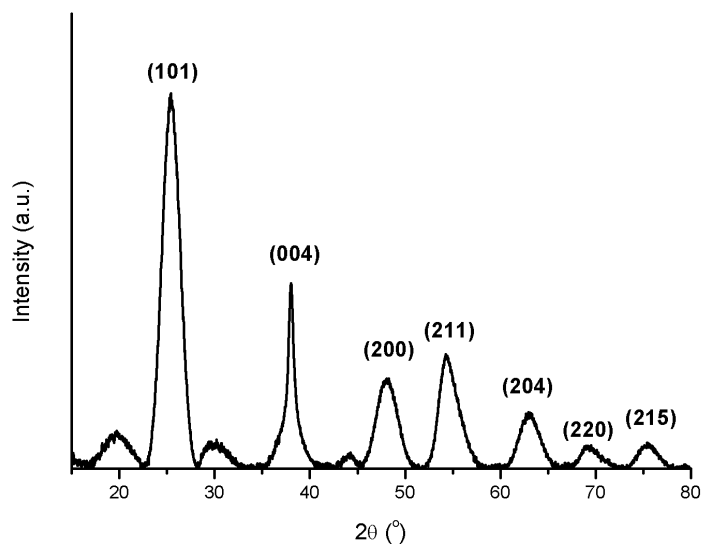
Figure 2.17: XRD pattern of OA-Capped TiO_2 nanorods with assigned Miller indices
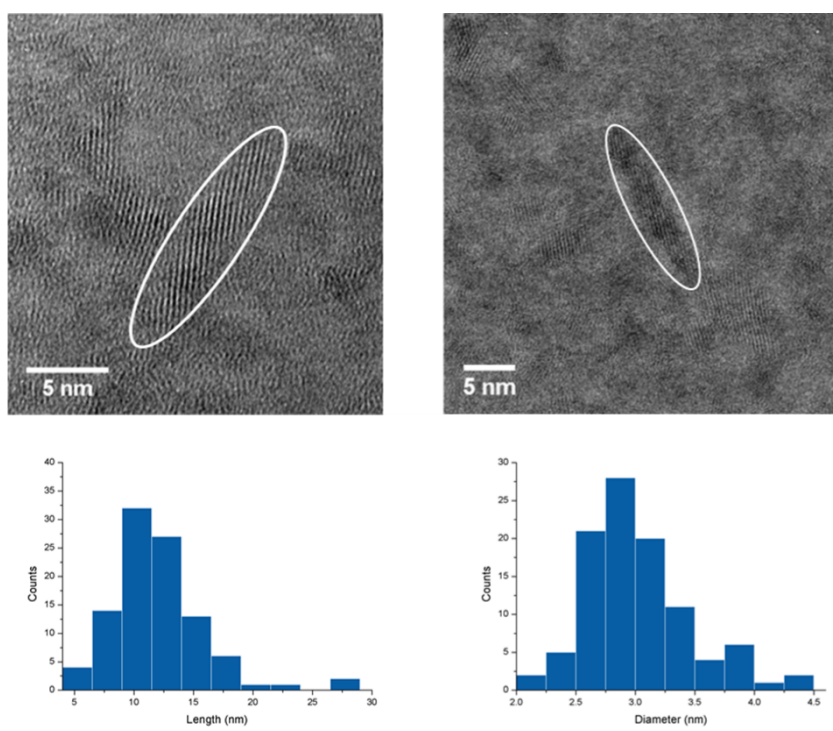
Figure 2.16: TEM images of OA-capped TiO_2 nanorods and size histograms (n=100)

The powder X-ray diffraction pattern in Fig 2.17 indicates that the nanoparticles are of the anatase phase. Debeye-Scherrer analysis of the [200] peak gives an estimate of the crystallite size of 37.1 Å. This is in close agreement with the diameter of the

nano-rods as shown in the TEM images in Figure 2.16.

The surface chemistry of the OA-capped TiO_2 NPs were investigated by ^{1}H NMR spectroscopy. The ^{1}H NMR spectra of both the OA-capped TiO_2 NPs and free-OA can be seen in Fig 2.18. In the ^{1}H NMR of the free-OA ligand, narrow peaks and fine structure are observed. This is as expected in the case of small molecules such as OA. The ^{1}H NMR spectrum of the bound OA however, features broadening of the peaks and a loss of fine structure. It is typical for bound ligands to exhibit line broadening indicative of excessive T_2 relaxation.[44] This is due to the different relaxation behaviours between bound and free molecules and serves as a useful diagnostic tool for the differentiation of these states.

It is interesting to note that the resonances closest to the bound carboxylic acid moiety exhibit the most severe line broadening. Indeed, the proton resonances -α and -β to the carboxylic acid have broadened close to the point of disappearing from the spectrum and the carboxylic acid resonance has completely disappeared. This is because these proton resonances are closest to the carboxylic acid binding group and thus closest to the surface of the TiO_2 NPs.
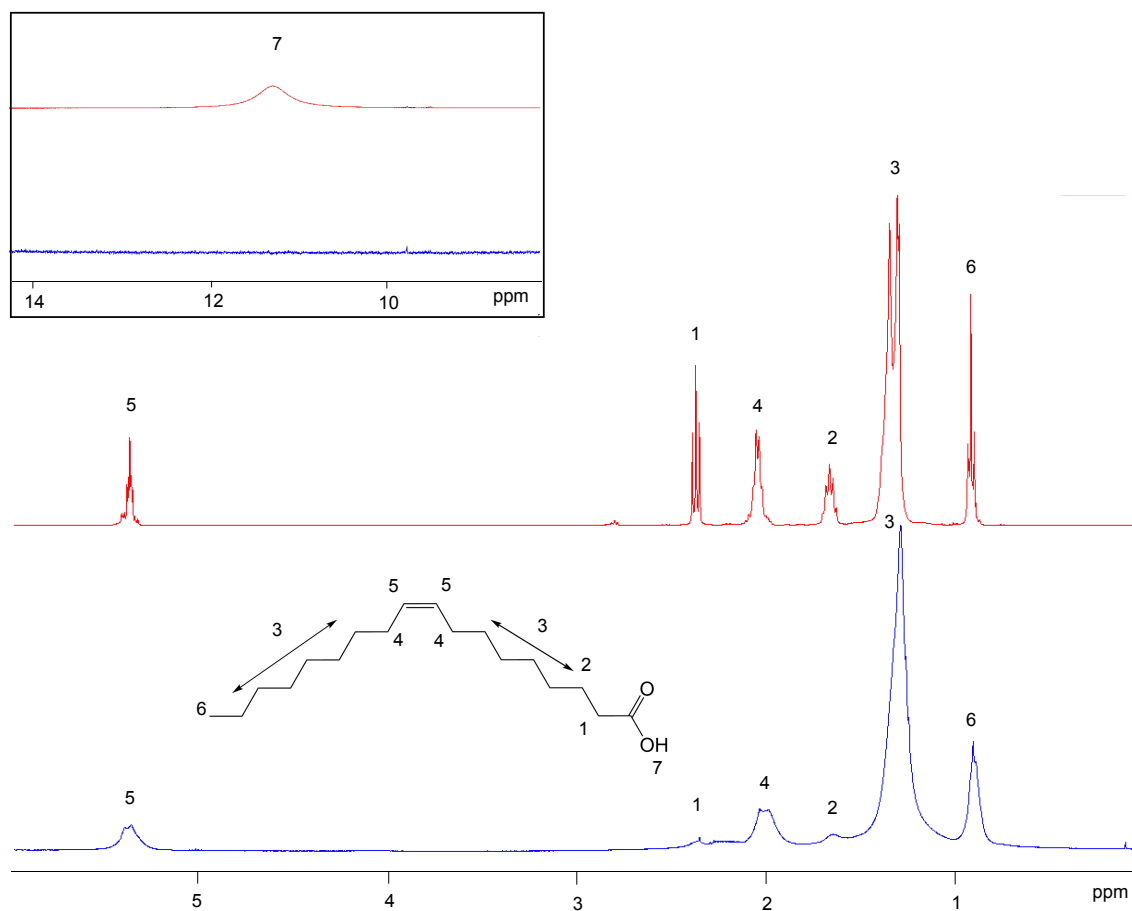
Figure 2.18: ^{1}H NMR of OA-capped TiO$_2$ nanoparticles (blue) and of free OA (red)

The 2D ^{1}H NMR NOESY spectrum of the OA-capped TiO$_2$ NPs provide further evidence that the OA-ligand is bound to the surface (Figure 2.19). The spectrum shows the negative (black) nOe cross-peaks, which are indicative of a bound ligand. Conversely, the 2D ^{1}H NMR NOESY spectrum of the free OA is shown in Figure 2.20. This spectrum features positive (red) NOE cross-peaks which are indicative of the free ligand.
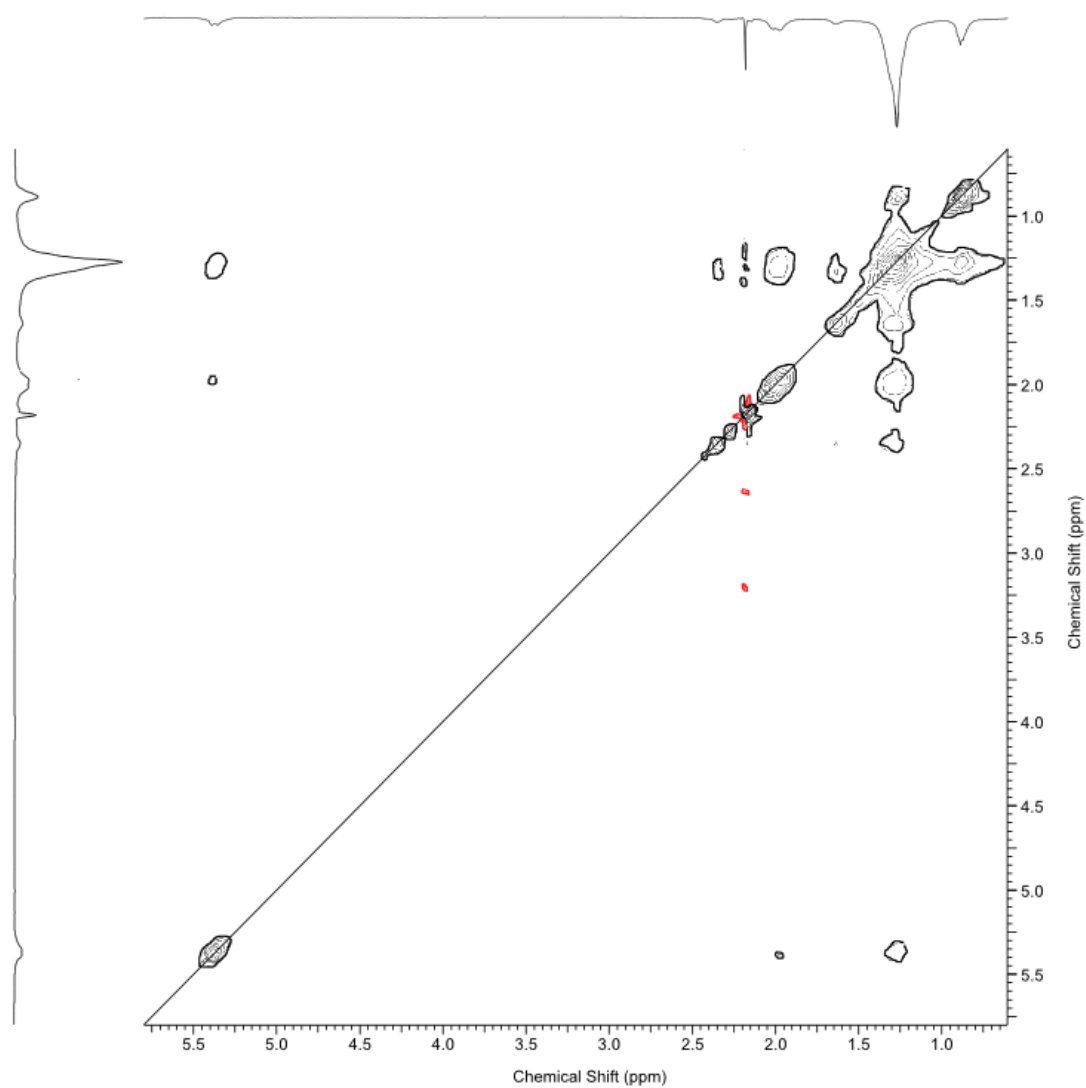
Figure 2.19: ^{1}H NMR NOESY spectrum of OA-capped TiO$_2$ nanoparticles. Red and black denotes positive and negative peaks respectively.
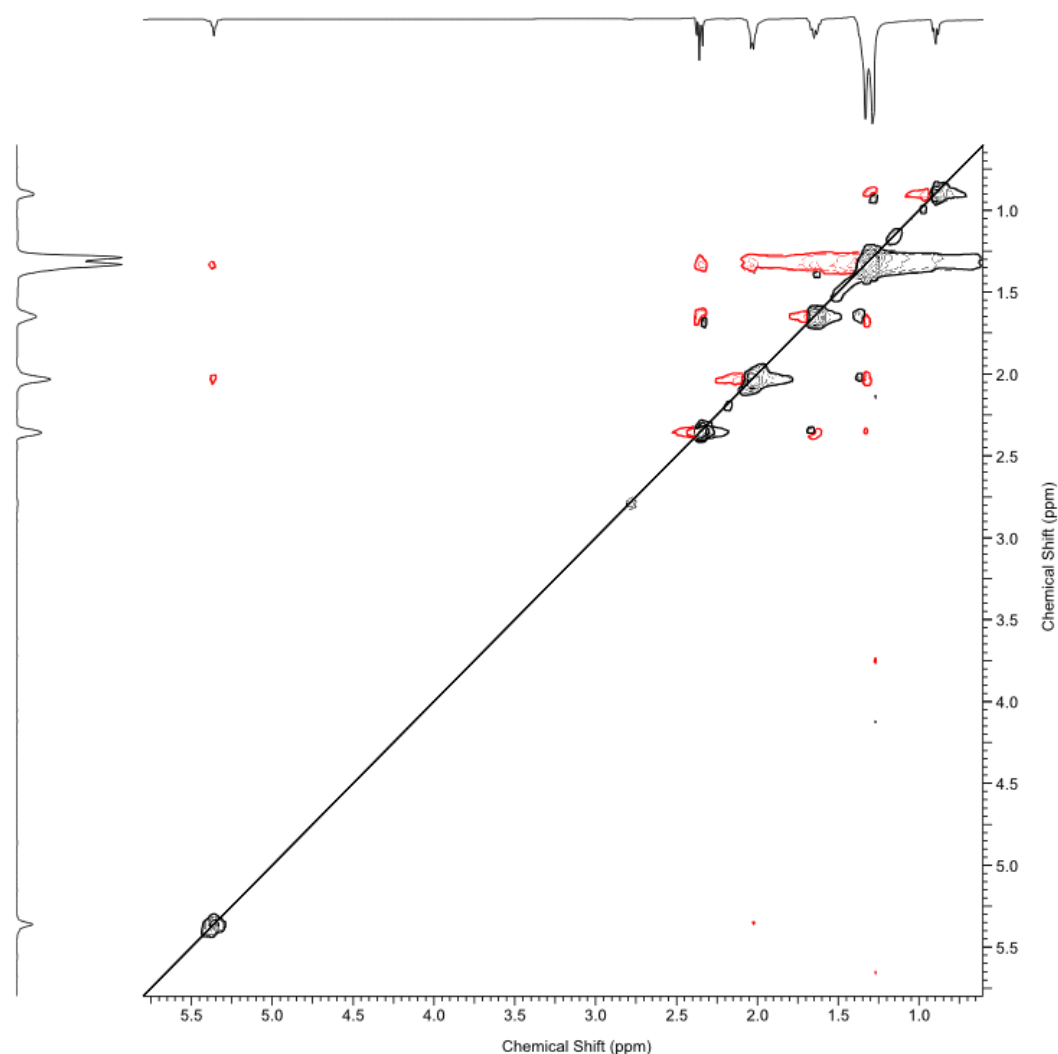
Figure 2.20: ^{1}H NMR NOESY spectrum of free OA. Red and black denotes positive and negative peaks respectively.

A method for the phase transfer of OA-capped TiO$_2$ NPs has been reported by Wilkerson *et al.*[42] The method involves the use of catechols in alkaline, aqueous solutions to prepare water-soluble TiO$_2$ NPs. A catechol is indeed a suitable ligand for stabilising the surface of TiO$_2$ NPs and syntheses have been reported for the preparation of catechol functionalised TiO$_2$ NCs.[45] L-DOPA, a chiral catechol was chosen to attempt this phase transfer. The method reported by Wilkerson et al. proved unsatisfactory as addition of NaOH to a solution of L-DOPA resulted in the immediate presence of a red colour. This red colour was due to the formation of

dopaquinone, the oxidation product of L-DOPA in alkaline conditions. This was confirmed by ^{1}H NMR. Structurally similar catechols such as adrenaline are known to rapidly oxidise in a matter of minutes to the quinone product in the presence of NaOH[46], whereas the phase transfer method reported by Wilkerson *et al.* is reported to take 18 hours to complete. The reported method is thus chemically unfeasible.
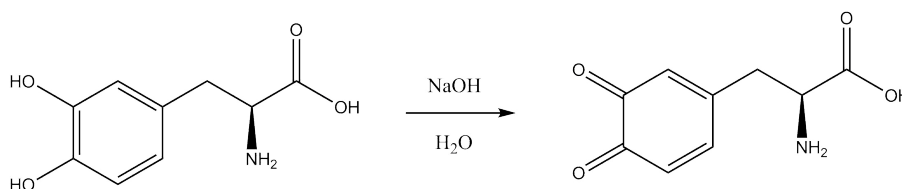
Figure 2.21: Oxidation of L-DOPA to dopaquinone

Initial attempts at performing the phase-transfer procedure followed a previously reported procedure that has been used to prepare aqueous chiral CdS, CdSe, CdTe and doped ZnS QDs[41]. This procedure involves the phase transfer of OA-stabilised QDs in organic solvents to the aqueous phase using a basic solution of amino acids. The OA was surmised to bind to the TiO_2 NP as a carboxylate anion. Hence, it should be possible to perform a simple ligand exchange with the carboxylate groups that are present in amino acids in basic conditions. In this scheme, one x-type ligand as according to the covalent bond classification method[47], would be exchanged for another. It was found that this ligand-exchange did not occur as expected, instead leading to a precipitation and resulting aggregation of the TiO_2 NPs. Once precipitated, the NCs lost their former solubility yielding only opaque suspensions of the NPs once re-suspended in either aqueous or organic solvents. This is most likely due to ion-pair formation between the large excess of Na^+ cations with the surface oleic acid leading to the removal of any stabilising ligand from the NP surface. This leaves behind a high energy NP surface that aggregates with the similarly bare surfaces of other NPs in an attempt to reduce this surface energy

An important difference between the binding mode of OA acid on the surface of MOs and the surface of metal chalcogenides is that in the case of MOs, the charge on the carboxylate ligands is balanced by co-adsorbed protons[48]. This is due to the high Brønsted basicity of the oxygen atoms, which are not present in metal chalcogenides.
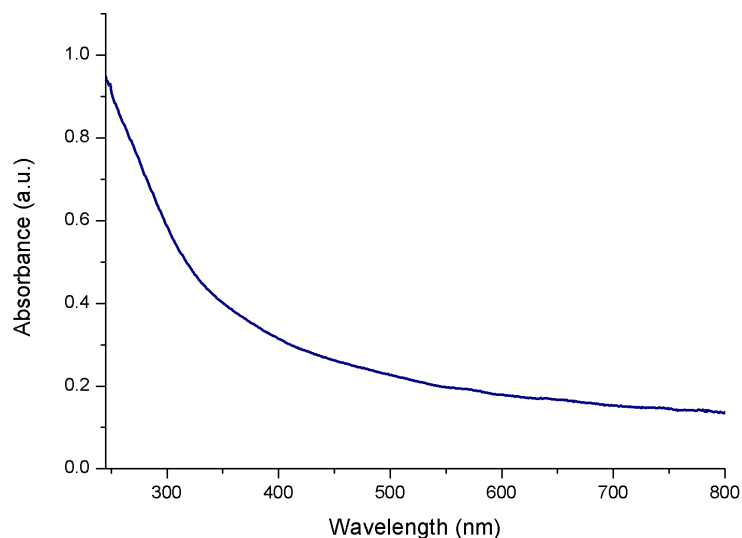
Figure 2.22: UV-vis absorption spectrum of OA-capped TiO_2 NCs

The carboxylic acids are thus dissociatively adsorbed to bind to the MO NCs, giving an overall charge neutral system. In the case of metal chalcogenides, the OA binding mode is that of a carboxylate, an x-type ligand.[49] Thus, different synthetic protocols must be utilised for the phase transfer of metal oxide NPs.

A successful phase transfer of OA-capped TiO_2 NPs was successfully carried out by utilising an aqueous system comprised of either D- or L-disodium tartrate. After this phase transfer step, aqueous soluble TiO_2 NPs are obtained. These NPs are chiroptically-active, which can be seen by examination of the band-edge region of the CD spectrum (Figure 2.23). The CD spectrum is distinctly different from the CD spectrum of the starting disodium salt which does not display any CD
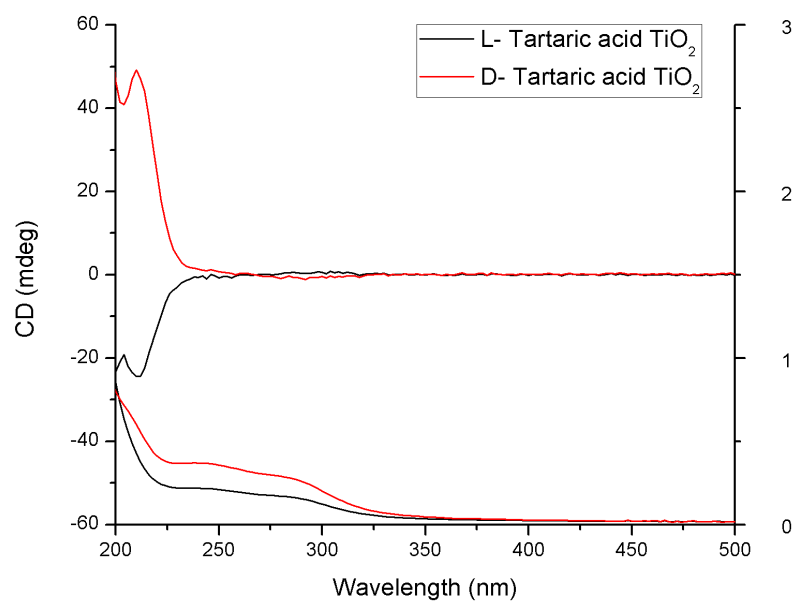
(a) CD and UV-vis spectra of D- and L-tartaric acid functionalised TiO_2 NPs
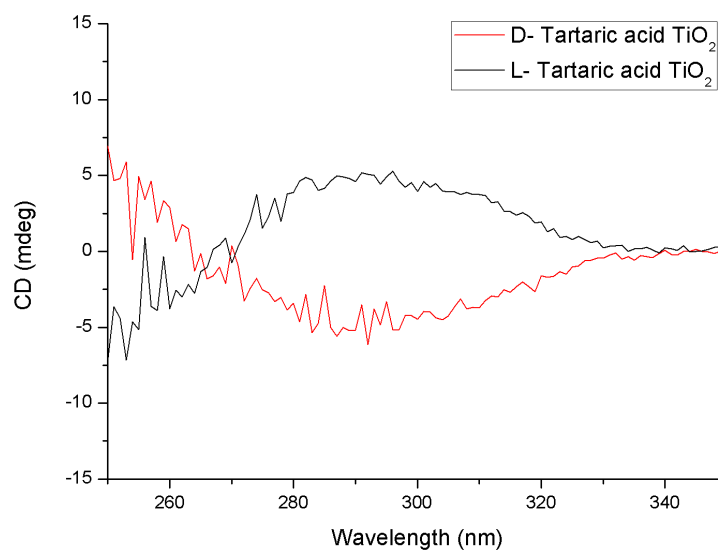
(b) CD spectra of the band-edge region of D- and L-tartaric acid functionalised TiO_2 NPs

Figure 2.23: CD and UV-vis spectra of D- and L-tartaric acid functionalised TiO_2 NPs

signal above 250 nm (Figure 2.25). Interestingly, the spectral shape of the tartaric acid stabilised TiO_2 NPs is similar to the DPEN-capped TiO_2 NPs presented earlier in this chapter (Figure 2.8), with a Cotton effect present in the same region.
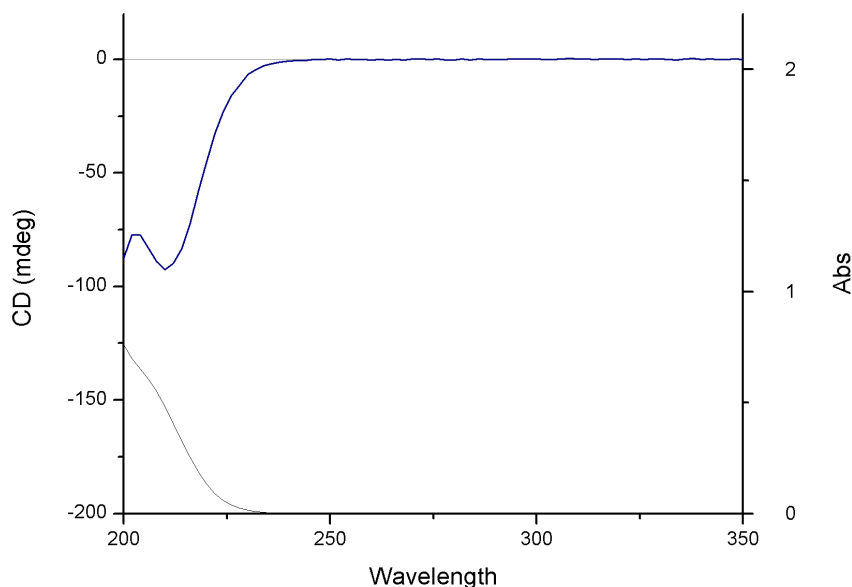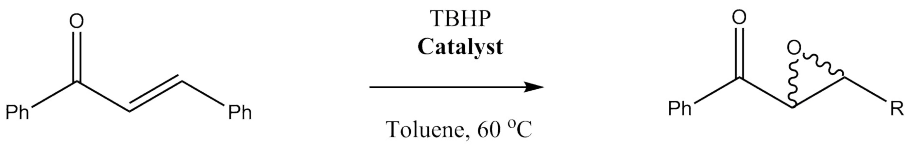
Figure 2.25: CD (navy) and UV-vis (black) spectrum of disodium-L-tartrate

We were not able to discern a difference in the ^{1}H NMR spectrum of the sample obtained after phase transfer and the disodium tartrate starting material. Investigation of the T_1 relaxation times indicated that both samples displayed the same behaviour. This may be due to a large excess of disodium tartrate present in the TiO_2 sample after phase transfer, which is he dominant signal being observed in the ^{1}H NMR analysis. Removal of this excess disodium tartrate by size-exclusion chromatography and subsequent ^{1}H NMR analysis of a pure sample of the chiroptically-active TiO_2 NPs will be the subject of future work.

2.2.3   Catalytic activity

2.2.3.1   Epoxidation

TiO_2 nanoparticles have been shown to a suitable heterogenous for the epoxidation of alkenes.[50,51] Therefore, the chiral TiO_2 NPs were investigated as potential catalysts for an asymmetric epoxidation. Tert-butyl hydroperoxide (TBHP) was chosen as the oxidation agent and trans-chalcone, an α, β -unsaturated ketone, was selected as the alkene. In the latter compound, the alkene is conjugated with a carbonyl

Catalyst	m_{cat} (g)	time (hrs)	Yield (%)	$[\alpha]_D^{25}$
no catalyst	-	72	0	-
P25 TiO$_2$	0.05	24	1	0
P25 TiO$_2$	0.05	48	11	0
P25 TiO$_2$	0.05	72	20	0
D-DPEN (1 eq.) TiO$_2$	0.01	72	1	0

Table 2.2: Catalytic epoxidation of chalcone by TBHP
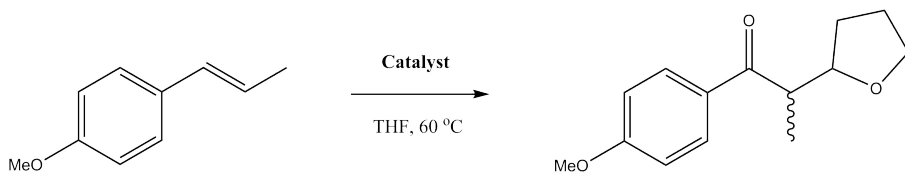
group, which decreases the activation energy to be attacked by nucleophilic species (TBHP) at the β-carbon.

The results of the catalytic investigations of the asymmetric epoxidation are summarised in Table 3.2. The epoxidation reaction was carried out in the presence of a chiral TiO$_2$ NPs. The epoxidation reaction was first tested with bare NPs that have no stabilising ligand on their surface. The results of these initial tests show that the TiO$_2$ NPs are suitable catalysts for the epoxidation reaction, with a yield of 20 % observed. The TiO$_2$ NPs used were commercially available Degussa P25 anatase NPs.

The NPs functionalised with chiral ligands display markedly reduced catalytic activity in all cases. The presence of the chiral ligands leads to reduced yields, accompanied by no enantioselective effect as can be seen by the absence of optical activity in the products of the reactions. The reduction in catalytic activity may be explained by the presence of the chiral ligands on the surface of the NPs. The chiral ligands bind through Lewis-basic centres, these bind to the Lewis-acidic metal centres present on the surface of the NPs. It is these Lewis-acidic centres which catalyse the reaction and once bound to the chiral ligands they are not available to catalyse the epoxidation.

2.2.3.2   Oxyalkylation

The oxyalkylation reaction between vinylarenes and cyclic ethers has been demonstrated by Sun *et al.* to proceed in the presence of metal oxide NPs.[52] High regioselectivity and good yields have been reported in this catalytic system. Thus, chiral TiO_2 NPs were used to catalyse this reaction. In a manner analogous to the epoxidation carried out in the previous section, bare TiO_2 NPs were used to determine their suitablility for catalysing the oxyalkylation reaction. A yield of 8 % was obtained.
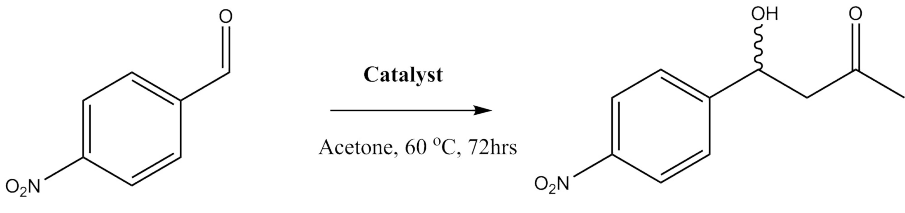
Catalyst	m_{cat} (g)	time (hrs)	Yield (%)	$[\alpha]_D^{25}$
no catalyst	-	48	0	-
P25 TiO_2	0.05	24	8	0
D-DPEN (1 eq.) TiO_2	0.05	24	0	-

Table 2.3: Catalytic oxyalkylation of anethole

2.2.3.3   Aldol

The aldol reaction between acetone and p-nitrobenzaldehyde was also investigated using the chiral TiO_2 NPs as a catalyst. Metal oxide[53,54] and metal chalcogenide[55] NPs funcitonalised with chiral ligands have been demonsrated to be suitable enantioselective catalysts for aldol reactions.

Catalyst	m_{cat} (g)	Yield (%)	$[\alpha]_D^{25}$
no catalyst	-	0	-
P25 TiO$_2$	0.05	8	0
D-DPEN (1 eq.) TiO$_2$	0.05	0	-

Table 2.4: Catalytic aldol reaction using Mn$_3$O$_4$ and TiO$_2$ NPs

Table 3.4 shows the results of the catalytic investigations of TiO$_2$ NPs in the aldol condensation between acetone and p-nitrobenzaldehyde. Bare TiO$_2$ NPs can be seen to catalyse the aldol reaction whereas bare The converse of this can be seen in the case of the NPs that are capped with chiral ligands. TiO$_2$ NPs capped with D-DPEN have no catalytic activity for the aldol reaction.

2.2.4 Chiral polymer templates and 16-2-16 gemini tartrates for the preparation of chiral TiO$_2$

In this part of our work a synthetic system using a chiral polymer complex was chosen for preparation of chiral TiO$_2$ nanostructures. The complex is based on the association of linear polyethylenimine (PEI) with a chiral tartaric acid. This system had been used previously to prepare chiral mesoporous silica[56] and could be conceivably adapted to prepare chiral titania. During the course of these investigations a patent was published detailing this exact synthetic approach, albeit utilising a different choice of titania precursor.[57] Another approach that has been investigated as a potential route to synthesising chiral metal oxides has been the use of cationic bis-quaternary ammonium gemini surfactants having the formula C$_2$H$_4$-1,2-((CH$_3$)2N$^+$C$_{16}$H$_{33}$)$_2$, noted hereafter 16-2-16. These 16-2-16 gemini surfactants have been coordinated to chiral tartrate molecules have been previously utilised to prepare a variety of chiral silica nanostructures.[58]

2.2.4.1 Synthesis of chiral TiO$_2$ using chiral polymer complex

Chiral crystalline complexes derived from the association of a chiral tartaric acid with PEI. Thes complexes was prepared starting from poly(2-ethyl-2-oxazoline), which had M$_n$ ranging from 12,500 to 16,500. The synthetic scheme of the preparation is presented in Scheme 2.2. The TiO$_2$ precursor chosen for the reaction was titanium diisopropoxide bis(acetylacetonate). Hydrolysis of this precursor proceeds relatively slowly in aqueous solutions and it has been used previously for the preparation of chiral TiO$_2$ nanohelices.[59] It is favourable to use a precursor that has a slow rate of hydrolysis as a fast rate would limit the contact time with the chiral polymer template, and thus the transcription of chirality from the chiral polymer template to the inorganic nanomaterial.
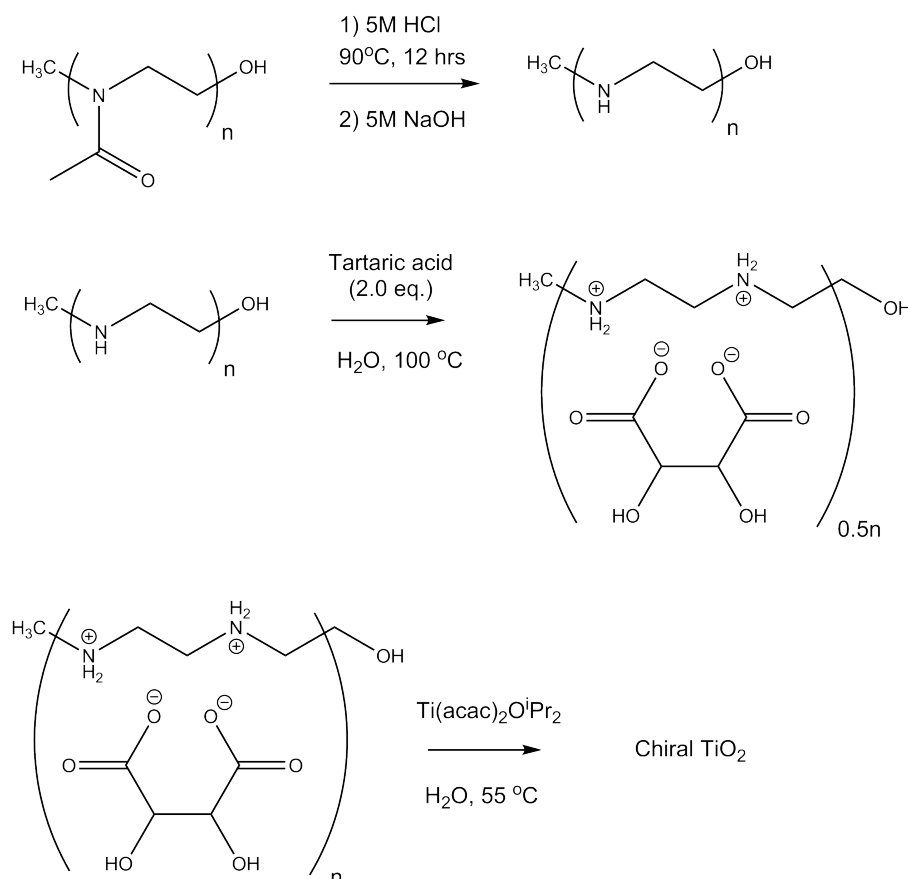
Scheme 2.2: Synthetic scheme for chiral TiO$_2$ using chiral polymer template

SEM imaging (Figure 2.1) of the L-tartaric acid@cPEI TiO$_2$ nanoparticles obtained from the synthesis indicates the formation of roughly spherical nanoparticles with

a size of 60 nm. The TEM images shown in Figure 2.27 also demonstrate this morphology. The sample is composed of amorphous, irregular spherical particles with a similar size regime.
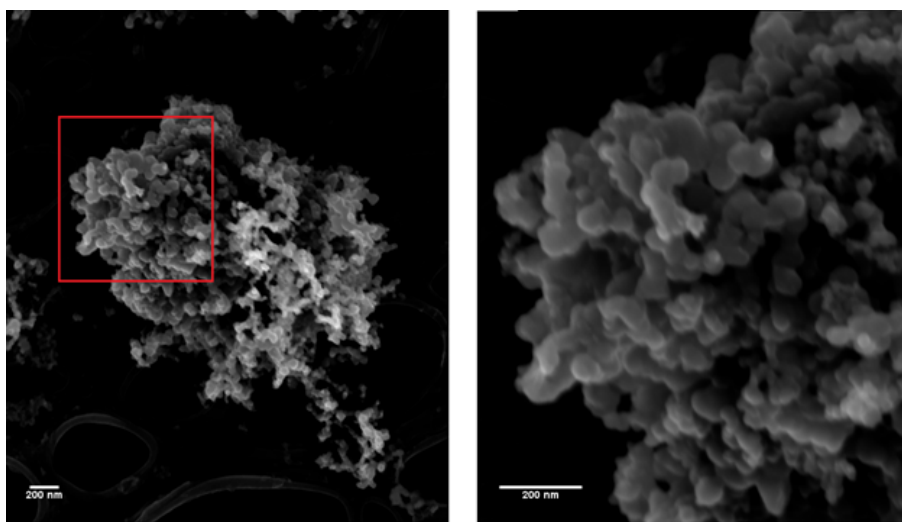
Figure 2.26: SEM images of D-tartaric acid/PEI TiO$_2$ NPs

The CD-spectra of the prepared tartaric acid@cPEI TiO$_2$ nanoparticles are shown in Figure 2.28. A g-factor spectrum comparison between both enantiomers is shown in Figure 2.30. Both these spectra indicate that the TiO$_2$ nanoparticles are chiroptically-active as they display a characteristic a Cotton effect indicative of a chiral species as the absorption peak reaches it maximum at 270 nm. This CD-response can be attributed to the TiO$_2$ as the tartaric acid@PEI chiral templates do not display any CD-response above 250 nm (Figure 2.29).
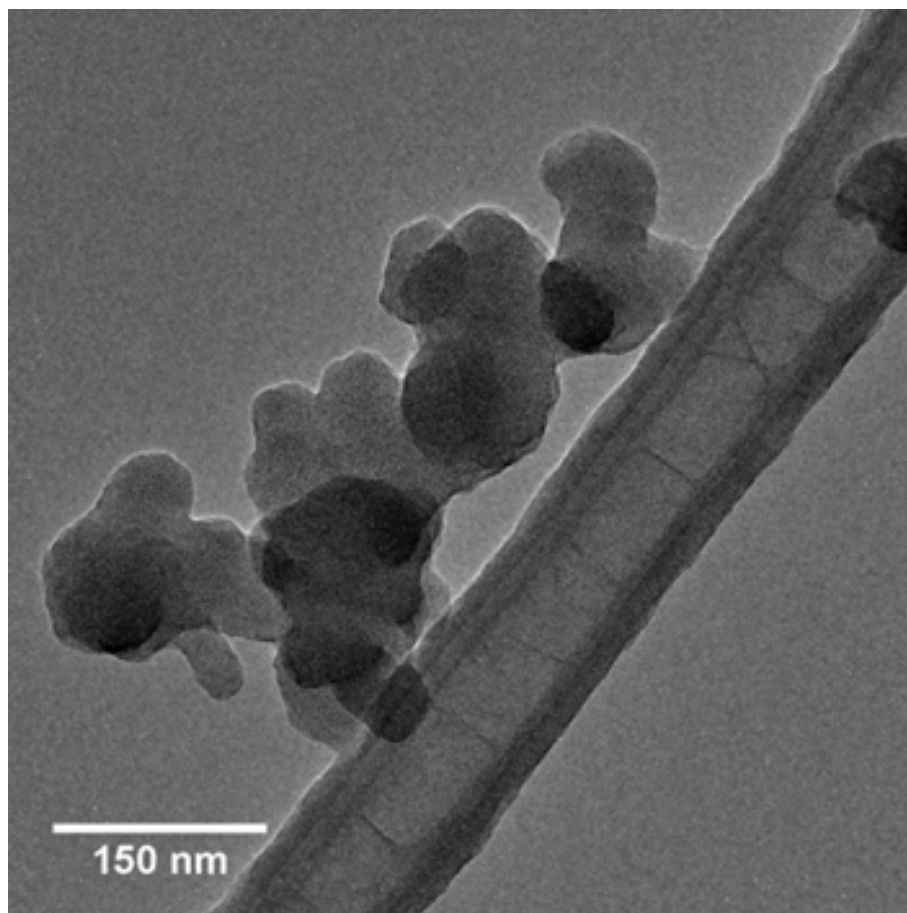
Figure 2.27: TEM image of D-tartaric acid/PEI TiO$_2$ NPs
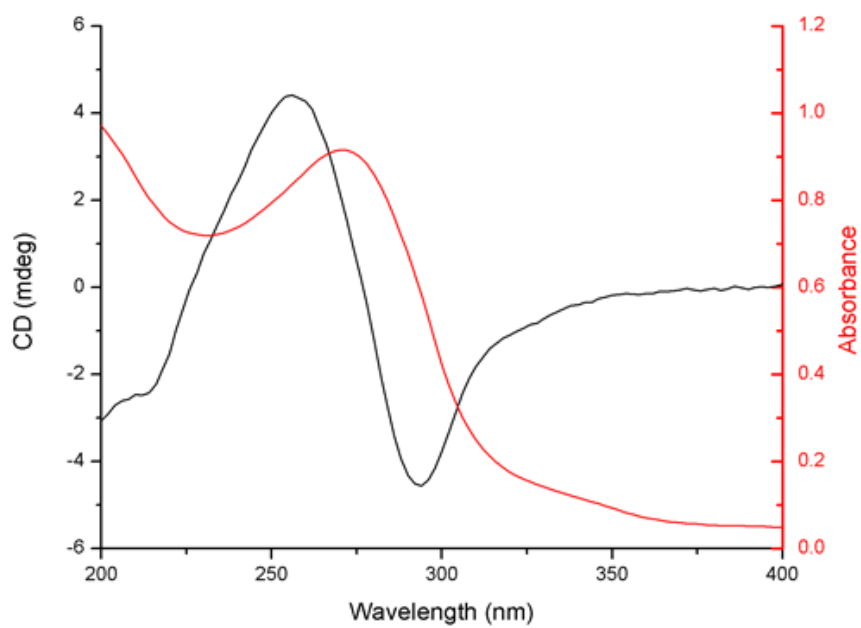
Figure 2.28: CD spectrum (black) and absorption spectrum (red) of D-tartaric acid/PEI
TiO$_2$ NPs
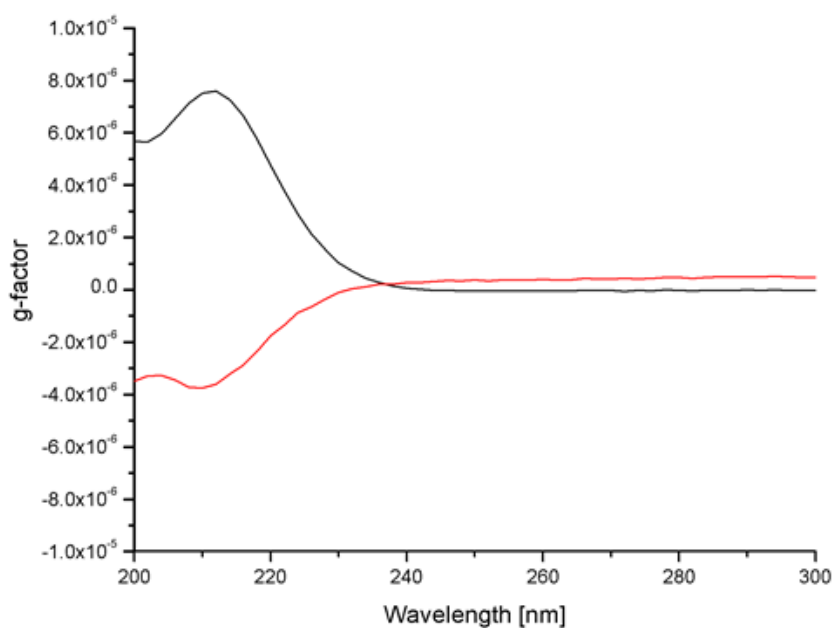
Figure 2.29: g-factor spectra of D- (black) and L- (red) tartaric acid/PEI

Thermo-gravimetric analysis (TGA) and differential thermal analyiss (DTA) were performed on the samples to determine a suitable temperature at which to crystallize the amorphous chiral TiO_2 material. The results of these investigations can be seen in Figure 2.31. There is a large weight loss to approximately 20 % at 700 °C, indicating that the amorphous material was composed mostly of the polymer template. The large exothermic peak at 550 °C indicates the temperature at which the amorphous TiO_2 crystallizes.
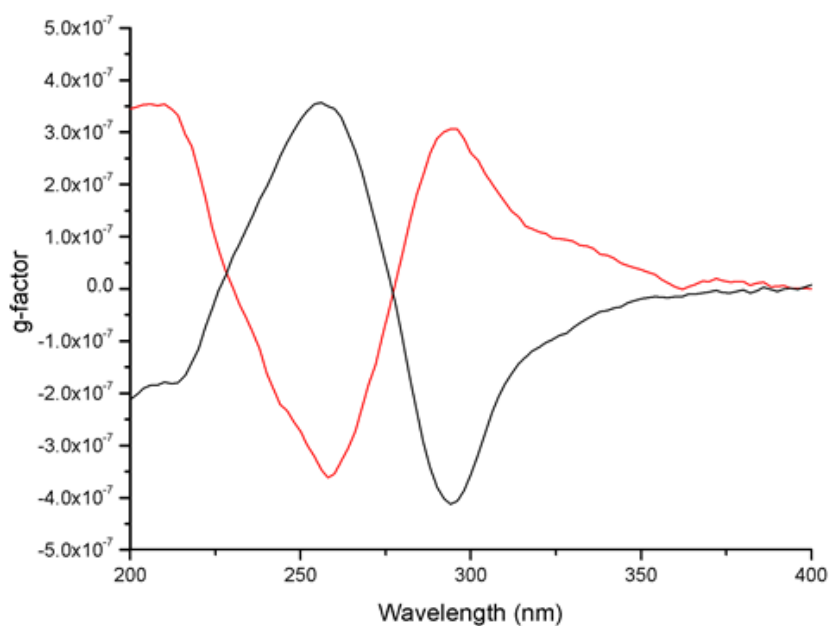
Figure 2.30: g-factor spectra of D- (black) and L- (red) tartaric acid/PEI TiO$_2$ NPs
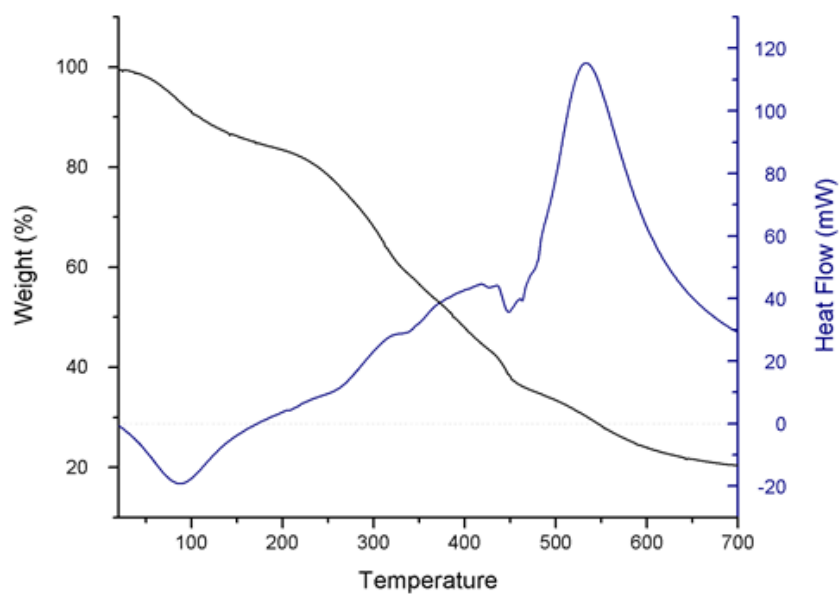
Figure 2.31: Thermo-gravimetric analysis curve (black) and differential thermal analysis curve (blue) of L-tartaric acid/PE TiO$_2$ NPs

The as prepared amorphous products from these syntheses were then calcined for 1 hour at 550 °C in order to obtain a crystalline material (Figure 2.32). Upon
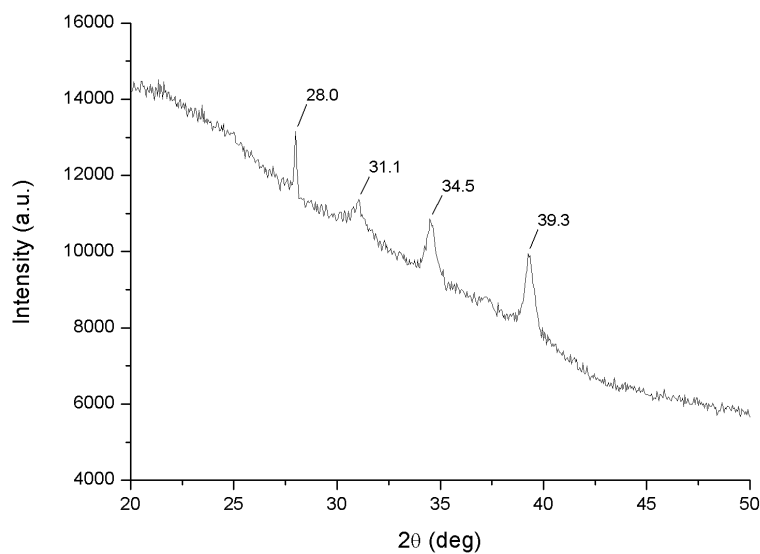
Figure 2.32: XRD spectrum of L-tartaric acid@PEI TiO$_2$ after calcination at 550 °C

crystallization, the TiO$_2$ is no longer chiral as evidenced by the CD spectrum shown in Figure 2.33. The same method has been reported to produce chiral mesoporous silica[60], and does not appear to extend to the production of chiral TiO$_2$. This is in stark contrast to the results reported by Ren-Hua *et al.*[57]
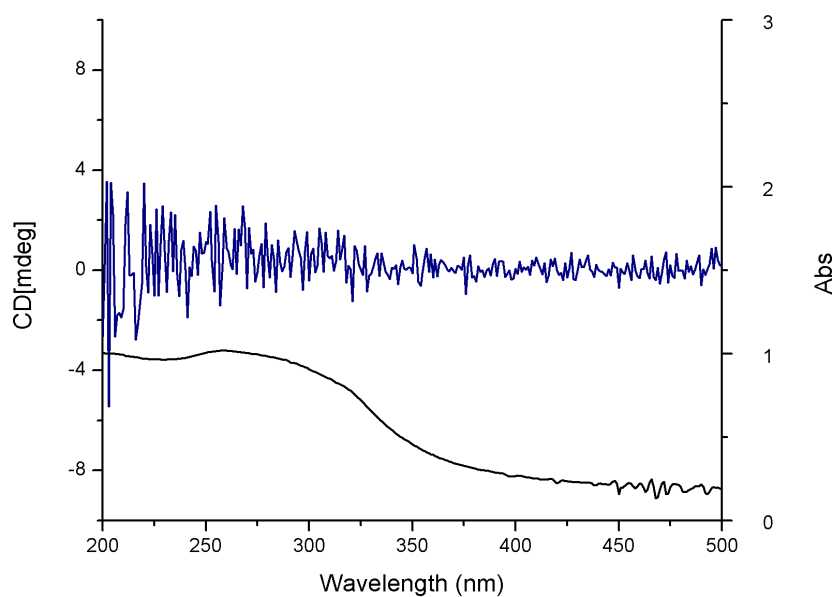
Figure 2.33: CD spectrum (navy) and absorption spectrum (black) of L-tartaric acid/PEI TiO$_2$ NPs after calcination for 1 hour at 550 °C

2.2.4.2   16-2-16 gemini tartrates as emplates for chiral silica and TiO$_2$ nanostructures

Assemblies of 16-2-16 gemini tartrates exhibit a wide array of potential morphologies in both aqueous and organic solutions. The morphology of these micellar structures is dependent on different reaction parameters such as time, temperature, and choice of solvent system (Figure 2.34). These structures have been used to template the formation of chiral silica structures, and the parameters for the said transcription of chirality have been optimised in that case.[58]
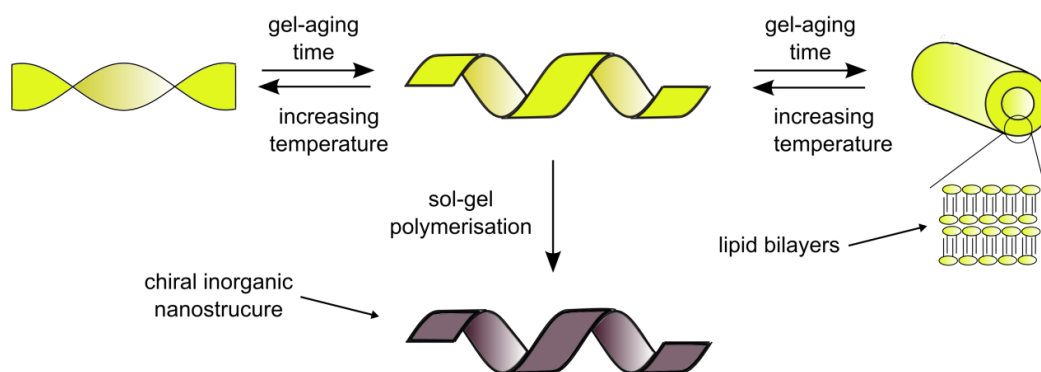
Figure 2.34: Schematic representation of the transcription of chirality from chiral 16-2-16 gemini tartrates in the formation of chiral inorganic nanomaterials

16-2-16 gemini D-tartrate was synthesised according to a previously reported synthetic scheme[61,62] (see Figure 2.3). The structure of the product was confirmed by ^{1}H NMR and mass spectrometry. The as synthesised 16-2-16 gemini D-tartrate was then used for sol-gel transcription of silica nanohelices.

The silica products from this reaction were then investigated by CD-spectroscopy as well as SEM-imaging. The CD-spectrum of the reaction product indicate the formation of a chiral species with a CD-absorbance band that begins at 300 nm. This is quite distinct from the spectrum obtained from the chiral 16-2-16 gemini D-tartrate starting material (Figure 2.7).

SEM images have shown nanostructures with helical morphology (Figure 2.36). The samples were difficult to image as sample degradation occurred under illumination with the electron beam. The helices were then coated with gold to alleviate this
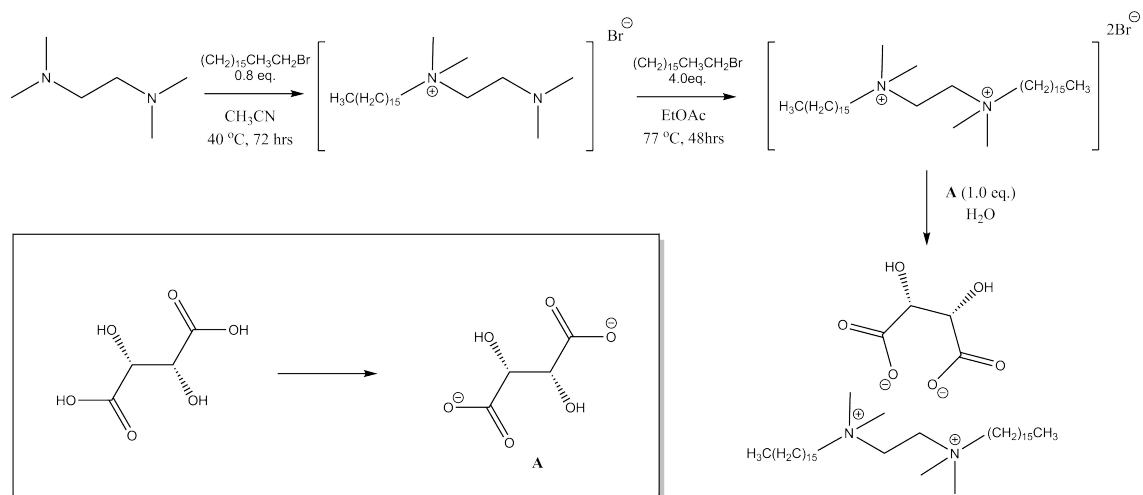
Scheme 2.3: Synthetic scheme for gemini surfactants
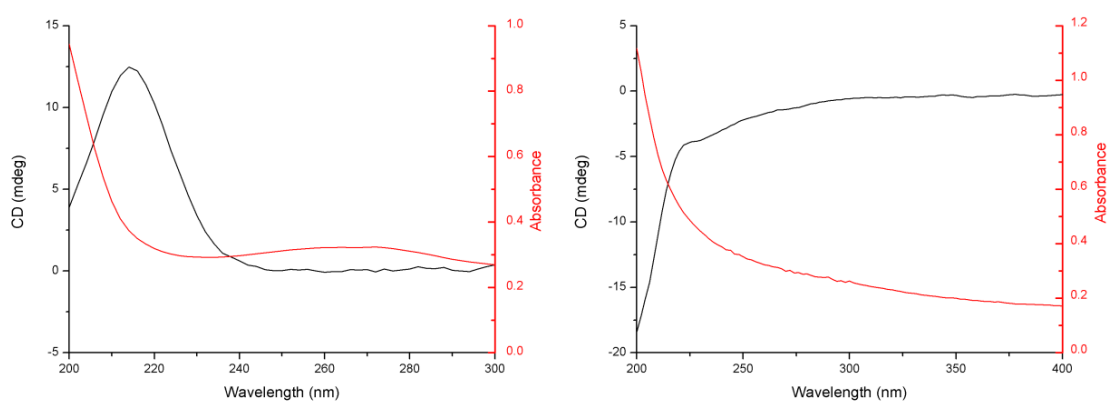
Figure 2.35: CD spectra (black) and corresponding UV-vis spectra (red) of 16-2-16 gemini D- tartrate (left) and 16-2-16 gemini D-tartrate silica nanomaterial (left)

problem. The SEM image in Figure 2.37 shows these results. The sample can be seen to be made up of gold coated rod-like structures in the size range of 150 to 250 nm in length.
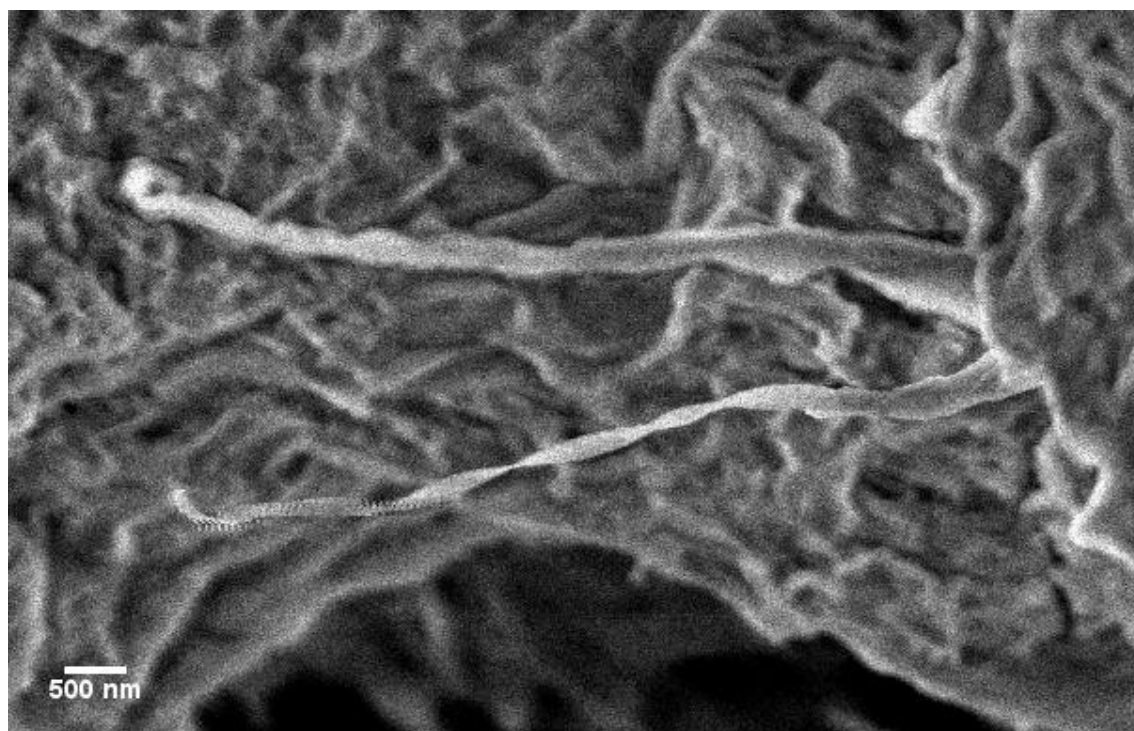
Figure 2.36: SEM image of 16-2-16 gemini D-tartrate silica nanomaterial

With satisfactory results obtained for the production of chiral silica nano-helices, the production of TiO_2 was attempted in a similar manner. In a manner of thinking in line with the previous section on the production of chiral TiO_2 using chiral polymer complexes, titanium diisopropoxide bis(acetylacetonate) was chosen as a TiO_2 precursor. The CD spectrum obtained from this experiment indicates that a chiral material was formed (Figure 2.38). A distinct signal outside of the expected region for the 16-2-16 gemini tartrates was observed. This can be assigned to the formation of a new TiO_2 material.
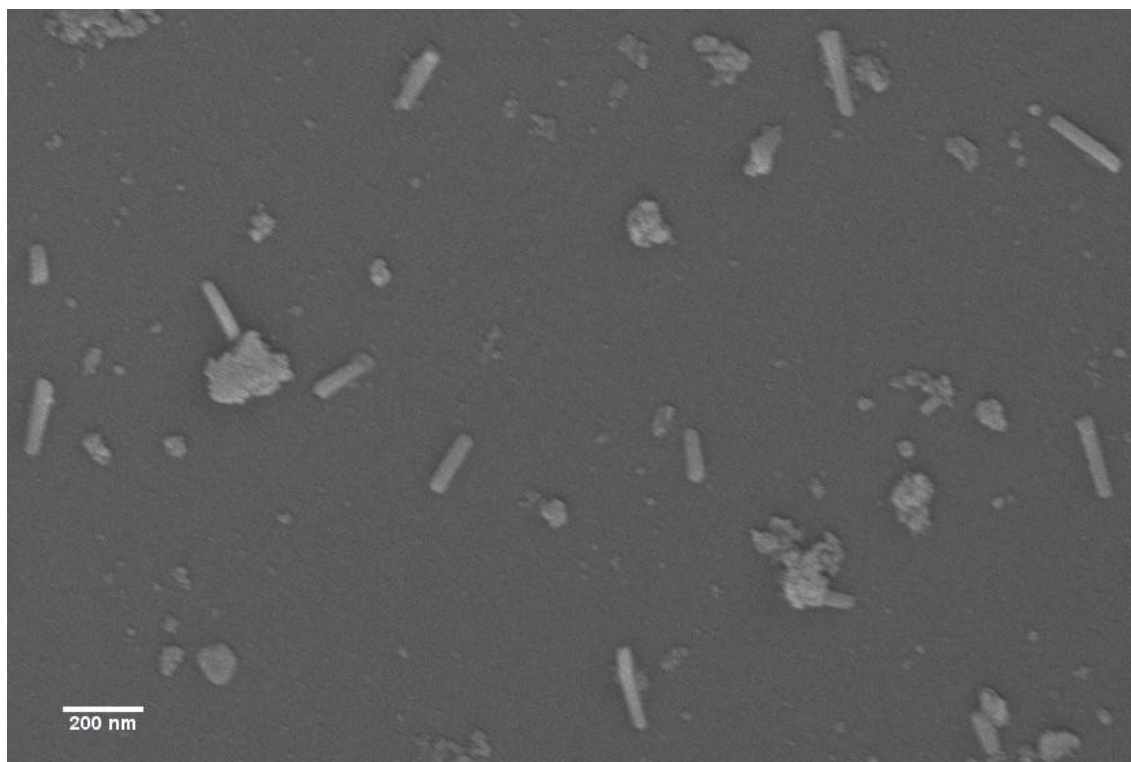
Figure 2.37: SEM image of gold coated 16-2-16 gemini D-tartrate silica nanomaterial
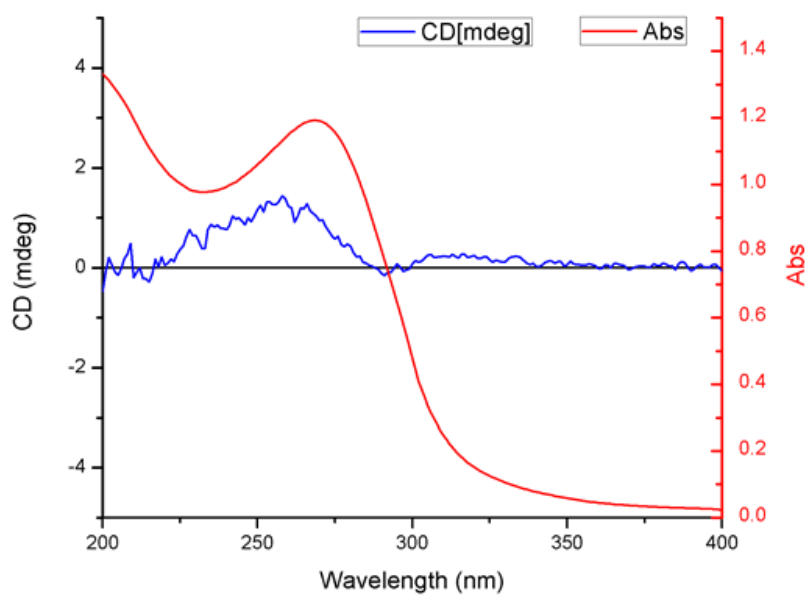
Figure 2.38: CD (blue) and absorption (red) Spectra of 16-2-16 gemini D-tartrate TiO$_2$
nanostructures

SEM images of the obtained nanomaterial show the formation of long wire-like

structures several hundered nanometres in length. A large amount of TiO_2 does appear to have formed independently of the template however, as can be seen from the images in Figure 2.39.
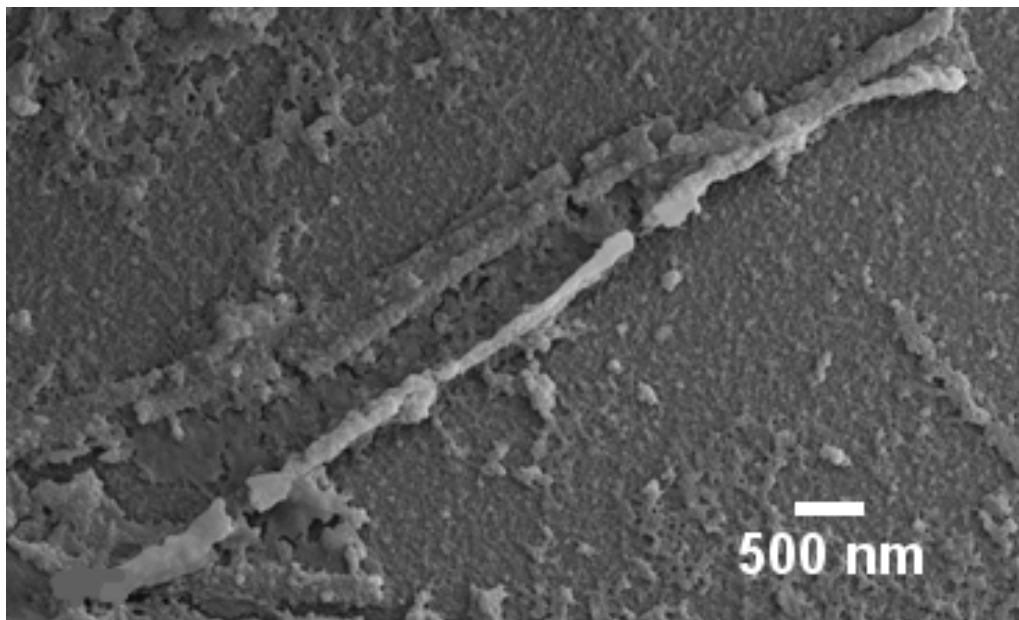
(a) SEM image of 16-2-16 gemini D-tartrate TiO_2 nanomaterial
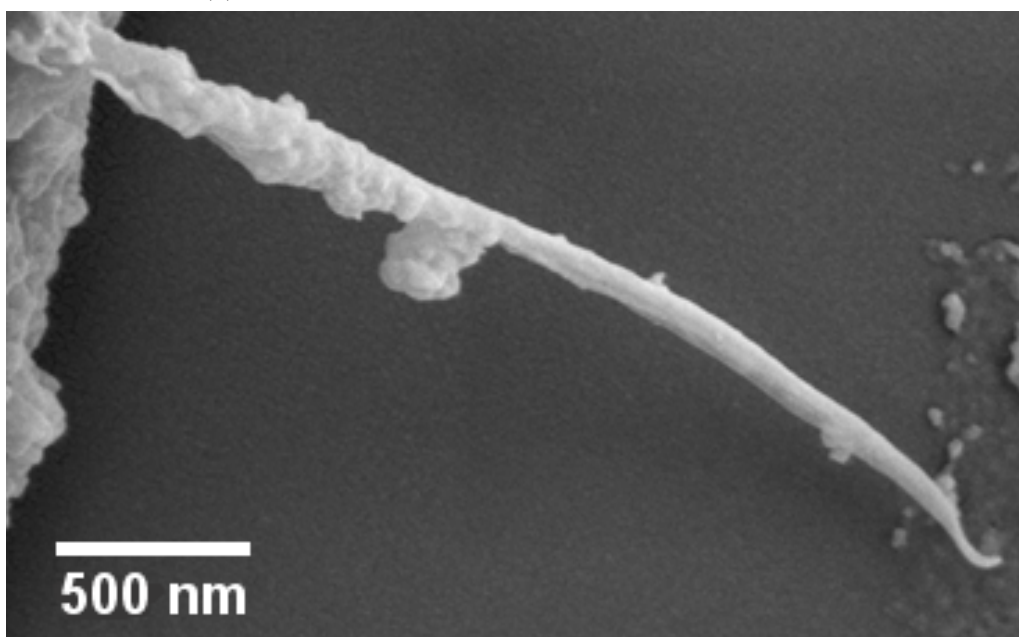
(b) SEM image of 16-2-16 gemini D-tartrate TiO_2 nanomaterial

Figure 2.39: SEM images of 16-2-16 gemini D-tartrate TiO_2 nanomaterial

2.3   Conclusions

Thus, we have developed new chiroptically-active and luminescent TiO_2 nanoparticles that is present an advance in the rapidly emerging field of chiral and luminescent nanomaterials. The results of electron microscopy, dynamic light scattering, and X-ray diffraction provide a complementary picture of the new nanomaterial as being composed of small anatase nanorods that have aggregated into larger dendritic structures. Analysis of the circular dichroism spectra demonstrates that there are two distinct components to this chiroptical activity that can be assigned to an organic component that is due to the presence of the chiral capping ligand and an inorganic component corresponding to the band-edge region of the TiO_2 nanomaterial. This chiral TiO2 nanomaterial differs from those previously reported in the literature as its chirality cannot be assigned as a result of a chiral macrostructure such as a helix.[59]

The luminescent properties of the chiral TiO_2 nanoparticles have also been investigated. There is a broad emission centered upon 439.5 nm with a quantum yield of 3.5 %. This has been assigned as a shallow trap state emission with a biexponential lifetime decay of 6.30 $\pm$ 0.029 and 13.62 $\pm$ 0.079 ns. We believe that these findings contribute to the further development of chiral metal oxide based luminescent nanomaterials, which may find a range of potential applications in chiral sensing, bioimaging, asymmetric catalysis, and chiral resolution of enantiomeric molecules.

These chiroptically-active TiO_2 NPs were also tested for catalytic activity for a range of organic transformations but were found to be catalytically inactive. This is presumably to be due to the DPEN ligand blocking access of the reagents to the catalytic sites present on the surface of the TiO_2 NPs.

Chiral polymer templates made from a tartaric acid and PEI complex were used for the production of an amorphous, chiroptically-active Tio_2 based nanomaterial. The material was not found to be chiroptically-active after removal of the template and crystallisation of the amorphous TiO_2 nanomaterial. 16-2-16 gemini tartrates were also used for the preparation of chiral TiO_2 with a helical morphology. This

synthetic protocol needs to be refined however, and will be the subject of future work.

Water soluble, chiroptically-active TiO $_2$ NPs were also prepared by a phase transfer protocol with tartaric acid. The ligand sphere of these NPs will be further characterised by NMR spectroscopy during the course of future work.

References

(1) Diebold, U. *Surface Science Reports* **2003**, *48*, 53–229.

(2) Wells, R. P. K. In *Metal Oxide Catalysis*; Wiley-VCH Verlag GmbH & Co. KGaA: 2009, pp 755–769.

(3) Zhang, H.; F. Banfield, J. *Journal of Materials Chemistry* **1998**, *8*, 2073–2076.

(4) Carp, O; Huisman, C. L.; Reller, A *Progress in Solid State Chemistry* **2004**, *32*, 33–177.

(5) Scanlon, D. O.; Dunnill, C. W.; Buckeridge, J; Shevlin, S. A.; Logsdail, A. J.; Woodley, S. M.; Catlow, C. R. A.; Powell, M. J.; Palgrave, R. G.; Parkin, I. P.; Watson, G. W.; Keal, T. W.; Sherwood, P; Walsh, A; Sokol, A. A. *Nature Materials* **2013**, *12*, 798–801.

(6) Xu, Y.; Schoonen, M. A. A. *American Mineralogist* **2000**, *85*, 543–556.

(7) Shiraishi, Y.; Hirai, T. *Journal of Photochemistry and Photobiology C: Photochemistry Reviews* **2008**, *9*, 157–170.

(8) Higashimoto, S.; Kitao, N.; Yoshida, N.; Sakura, T.; Azuma, M.; Ohue, H.; Sakata, Y. *Journal of Catalysis* **2009**, *266*, 279–285.

(9) Du, P.; Moulijn, J. A.; Mul, G. *Journal of Catalysis* **2006**, *238*, 342–352.

(10) Pillai, U. R.; Sahle–Demessie, E. *Journal of Catalysis* **2002**, *211*, 434–444.

(11) Yurdakal, S.; Palmisano, G.; Loddo, V.; Augugliaro, V.; Palmisano, L. *Journal of the American Chemical Society* **2008**, *130*, 1568–1569.

(12) Rauf, M. A.; Meetani, M. A.; Hisaindee, S *Desalination* **2011**, *276*, 13–27.

(13) Ho, X.-H.; Kang, M.-J.; Kim, S.-J.; Park, E. D.; Jang, H.-Y. *Catalysis Science & Technology* **2011**, *1*, 923–926.

(14)   Fujishima, A.; Zhang, X.; Tryk, D. A. *Surface Science Reports* **2008**, *63*, 515–582.

(15)   Zhang, W. F.; Zhang, M. S.; Yin, Z; Chen, Q *Applied Physics B* **2000**, *70*, 261–265.

(16)   Tang, H; Berger, H; Schmid, P. E.; Lévy, F; Burri, G *Solid State Communications* **1993**, *87*, 847–850.

(17)   Rex, R. E.; Knorr, F. J.; McHale, J. L. *The Journal of Physical Chemistry C* **2015**, *119*, 26212–26218.

(18)   Choudhury, B; Choudhury, A *Journal of Luminescence* **2013**, *136*, 339–346.

(19)   Abazović, N. D.; Čomor, M. I.; Dramićanin, M. D.; Jovanović, D. J.; Ahrenkiel, S. P.; Nedeljković, J. M. *The Journal of Physical Chemistry B* **2006**, *110*, 25366–25370.

(20)   Yoo, H.; Kim, M.; Bae, C.; Lee, S.; Kim, H.; Ahn, T. K.; Shin, H. *The Journal of Physical Chemistry C* **2014**, *118*, 9726–9732.

(21)   Stevanovic, A; Buttner, M; Zhang, Z; Yates, J. T. *Journal of the American Chemical Society* **2012**, DOI: 10.1021/ja2072737.

(22)   Lv, K. L.; Xiang, Q. J.; Yu, J. G. *Applied Catalysis B-Environmental* **2011**, *104*, 275–281.

(23)   Mercado, C. C.; Knorr, F. J.; McHale, J. L.; Usmani, S. M.; Ichimura, A. S.; Saraf, L. V. *The Journal of Physical Chemistry C* **2012**, *116*, 10796–10804.

(24)   Niederberger, M; Bartl, M. H.; Stucky, G. D. Benzyl alcohol and titanium tetrachloride - A versatile reaction system for the nonaqueous and low-temperature preparation of crystalline and luminescent titania nanoparticles., 2002.

(25)   Tohgha, U.; Deol, K. K.; Porter, A. G.; Bartko, S. G.; Choi, J. K.; Leonard, B. M.; Varga, K.; Kubelka, J.; Muller, G.; Balaz, M. *ACS Nano* **2013**, *7*, 11094–11102.

(26)   Moshe, A. B.; Markovich, G. *Israel Journal of Chemistry* **2012**, *52*, 1104–1110.

(27)   Govorov, A. O.; Gun'ko, Y. K.; Slocik, J. M.; Gerard, V. A.; Fan, Z.; Naik, R. R. *Journal of Materials Chemistry* **2011**, *21*, 16806–16818.

(28)   Li, Y. T.; Song, C. H.; Wang, Y. Q.; Wei, Y; Wei, Y. J.; Hu, Y. Z. *Luminescence* **2007**, *22*, 540–545.

(29)   Sun, C. Q. In *Synthesis, Properties, and Applications of Oxide Nanomaterials*; John Wiley & Sons, Inc.: 2006, pp 7–47.

(30)   Shi, J.; Chen, J.; Feng, Z.; Chen, T.; Lian, Y.; Wang, X.; Li, C. *The Journal of Physical Chemistry C* **2007**, *111*, 693–699.

(31)   Munnix, S; Schmeits, M *Physical Review B* **1985**, *31*, 3369–3371.

(32)   Würth, C.; Grabolle, M.; Pauli, J.; Spieles, M.; Resch-Genger, U. *Nat. Protocols* **2013**, *8*, 1535–1550.

(33)   Su, W.; Zhang, T.; Li, L.; Xing, J.; He, M.; Zhong, Y.; Li, Z. *RSC Advances* **2014**, *4*, 8901–8906.

(34)   Forss, L; Schubnell, M *Applied Physics B* **1993**, *56*, 363–366.

(35)   Iatsunskyi, I.; Pavlenko, M.; Viter, R.; Jancelewicz, M.; Nowaczyk, G.; Baleviciute, I.; Załęski, K.; Jurga, S.; Ramanavicius, A.; Smyntyna, V. *The Journal of Physical Chemistry C* **2015**, *119*, 7164–7171.

(36)   Boens, N. et al. *Anal Chem* **2007**, *79*, 2137–2149.

(37)   Susha, A. S.; Lutich, A. A.; Liu, C. M.; Xu, H; Zhang, R. Q.; Zhong, Y. C.; Wong, K. S.; Yang, S. H.; Rogach, A. L. *Nanoscale* **2013**, *5*, 1465–1469.

(38)   Kumar, J.; Nakashima, T.; Kawai, T. *The Journal of Physical Chemistry Letters* **2015**, *6*, 3445–3452.

(39)   Kumar, J.; Kawai, T.; Nakashima, T. *Chemical Communications* **2017**, *53*, 1269–1272.

(40)   Longhi, G.; Castiglioni, E.; Koshoubu, J.; Mazzeo, G.; Abbate, S. *Chirality* **2016**, *28*, 696–707.

(41)   Moloney, M. P.; Govan, J.; Loudon, A.; Mukhina, M.; Gun'ko, Y. K. *Nat. Protocols* **2015**, *10*, 558–573.

(42)   Wilkerson, R. J.; Elder, T.; Sowinksi, O.; Fostvedt, J. I.; Hoefelmeyer, J. D. *Surface Science* **2016**, *648*, 333–338.

(43)   Joo, J.; Kwon, S. G.; Yu, T.; Cho, M.; Lee, J.; Yoon, J.; Hyeon, T. *The Journal of Physical Chemistry B* **2005**, *109*, 15297–15302.

(44)   Hens, Z.; Martins, J. C. A solution NMR toolbox for characterizing the surface chemistry of colloidal nanocrystals., 2013.

(45)   Niederberger, M.; Garnweitner, G.; Krumeich, F.; Nesper, R.; Cölfen, H.; Antonietti, M. *Chemistry of Materials* **2004**, *16*, 1202–1208.

(46)   West, G. B. *British Journal of Pharmacology and Chemotherapy* **1947**, *2*, 121–130.

(47)   Green, M. L. H. *Journal of Organometallic Chemistry* **1995**, *500*, 127–148.

(48)   DeRoo, J.; Justo, Y.; DeKeukeleere, K.; VandenBroeck, F.; Martins, J. C.; Van-Driessche, I.; Hens, Z. *Angewandte Chemie International Edition* **2015**, *54*, 6488–6491.

(49)   Anderson, N. C.; Hendricks, M. P.; Choi, J. J.; Owen, J. S. *Journal of the American Chemical Society* **2013**, DOI: 10.1021/ja4086758.

(50)   Qi, J. Y.; Yang, Q. Y.; Liu, Z. Y.; Li, X. J. *Chemical Journal of Chinese Universities - Chinese* **1999**.

(51)   Choudhary, V. R.; Jha, R.; Jana, P. *Catalysis Communications* **2008**, *10*, 205–207.

(52)   Sun, H.; Zhang, Y.; Guo, F.; Zha, Z.; Wang, Z. *The Journal of Organic Chemistry* **2012**, *77*, 3563–3569.

(53)   Kantam, M. L.; Ramani, T.; Chakrapani, L.; Kumar, K. V. *Tetrahedron Letters* **2008**, *49*, 1498–1501.

(54)   Choudary, B. M.; Chakrapani, L.; Ramani, T.; Kumar, K. V.; Kantam, M. L. *Tetrahedron* **2006**, *62*, 9571–9576.

(55)   Shah, E.; Soni, H. P. *RSC Advances* **2013**, *3*, 17453–17461.

(56)   Matsukizono, H.; Jin, R.-H. *Angewandte Chemie International Edition* **2012**, *51*, 5862–5865.

(57)   Jin Ren-Hua; Matsukizono, H. Method for producing chiral metal oxide structure, and chiral porous structure., 2014.

(58)   Delclos, T.; Aimé, C.; Pouget, E.; Brizard, A.; Huc, I.; Delville, M.-H.; Oda, R. *Nano Letters* **2008**, *8*, 1929–1935.

(59)   Liu, S.; Han, L.; Duan, Y.; Asahina, S.; Terasaki, O.; Cao, Y.; Liu, B.; Ma, L.; Zhang, J.; Che, S. *Nat Commun* **2012**, *3*, 1215.

(60)   Matsukizono, H.; Jin, R.-H. *Angewandte Chemie International Edition* **2012**, *51*, 5862–5865.

(61)   Oda, R.; J. Candau, S.; Huc, I. *Chemical Communications* **1997**, 2105–2106.

(62)   Brizard, A.; Berthier, D.; Aimé, C.; Buffeteau, T.; Cavagnat, D.; Ducasse, L.; Huc, I.; Oda, R. *Chirality* **2009**, *21*, E153–E162.

Chapter 3

Chiroptically-Active Mn_3O_4 Nanoparticles

3.1 Introduction

Manganese oxide nanomaterials are widely used in electrode materials,[1,2] magnetic devices[3] and catalysis.[4] Among the manganese oxides, Mn_3O_4 is one of the most unique due to having the greatest stability as well its mixed-valence state. Mn_3O_4 is a complex oxide containing both di- and tri-valent manganese ions. Its formula can be represented as $Mn^{2+}Mn^{3+}_2O_4$. It is an example of a spinel-oxide, the structure of which can be seen in Figure 3.1.

Mn_3O_4 has found many applications in catalysing organic transformations. Examples of these applications include the photocatalytic degradation of organic dyes,[5,6] various selective oxidations,[7–10] and has been found to catalyse the regioselective synthesis of a variety of 3, 4-disubstituted coumarin derivatives.[11]

Mn_3O_4 is also a promising material for potential biomedical applications as it has reported antibacterial[12–14] and anticancer properties[15,16]. It is also suitable as an MRI contrast agent, having twice the relaxivity of commercial Gd-based contrast agents.[17,18] These dual properties have been utilised in single nanomedicine systems delivering both a therapeutic and diagnostic element.[19,20] The main aim of this part

of our research is to deveop new chiral Mn_3O_4 based nanomaterials, investigate their properties and explore them as potential catalysts in asymmetric synthesis.
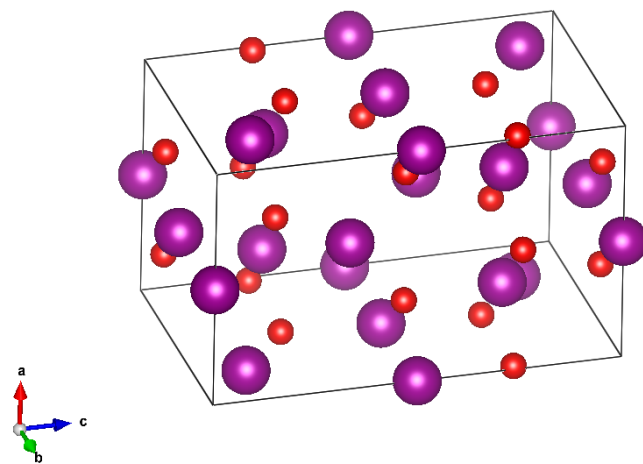
Figure 3.1: The unit cell of Mn_3O_4. Manganese atoms are marked purple whereas oxygen atoms are marked red.

3.2 Results and Discussion

3.2.1 Preparation of chiral Mn_3O_4 NPs using phenylalanol ligands

For the preparation of chiral Mn_3O_4, an aqueous system comprised of sodium dodecyl sulfate (SDS), (S)-(-) or (R)-(+)-phenylalaninol and $MnCl_2.4H_2O$ was chosen. A copper-based system analogous to this has been previously used to synthesise chiral CuO nanoflowers[21] and aqueous surfactant controlled syntheses have been widely reported for the formation of manganese oxide nanoparticles.[6,22,23] SDS was chosen as a structure directing agent for controlling the particle to produce a monodisperse sample. SDS exhibits high ampiphilicity in aqueous solutions, as well as the electrostatic interaction between positively charged manganese ions and negatively charged sulfate headgroups. The (S)-(-) and (R)-(+)-phenylalaninol were chosen as symmetry breaking ligands required to produce a chiral nanomaterial. These ligands have been proposed to have a cooperative assembly effect from the benzene ring interacting with the hydrophobic tail of the SDS and the amino alcohol groups chelating to the metal ions (manganese in this case).[21] SEM images (Figure 3.2) of the Mn_3O_4 NPs obtained from this synthesis indicate that the sample has a wide size and morphology distribution. Octahedral nanoparticles with a size range of 30 to 125 nm can be observed as well as larger platelet-like structures that can be several hundred nm in diameter.

The Raman spectra (Figure 3.3) obtained from the samples show peaks at 305, 360 and 645 cm^{-1}, which are in good agreement with the literature reports for nanoparticulate samples of Mn_3O_4.[24,25] The sharp peak at 645 cm^{-1} is particularly associated with Mn_3O_4 and can be assigned to the A_{1g} mode, corresponding to Mn-O breathing vibrations. This peak is typical of spinel structures such as Mn_3O_4.

The XRD pattern of the (S)-(-)-phenylalaninol nanoparticles in Figure 3.4 is consistent with the assignment of a spinel-type crystal structure from results of the Raman spectra. There are major peaks at 32.3, 36.1 and 59.8. These peaks correspond to the (211), (103) and (224) reflections of Mn_3O_4. These and the other peaks are in
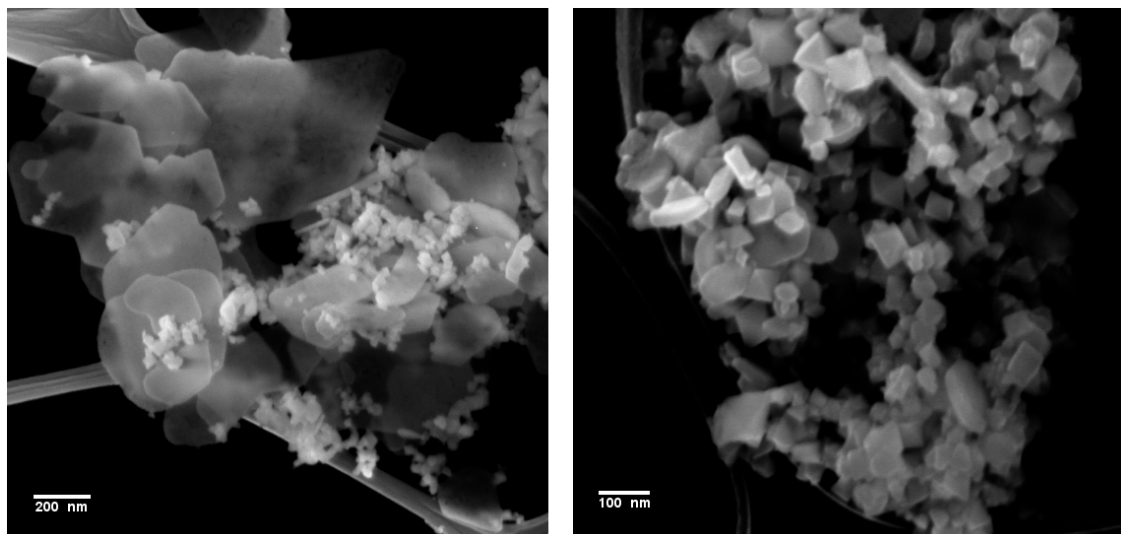
Figure 3.2: SEM images of (R)-(+)-phenylalaninol Mn_3O_4 (left) and (S)-(-)-phenylalaninol Mn_3O_4 (right) nanoparticles
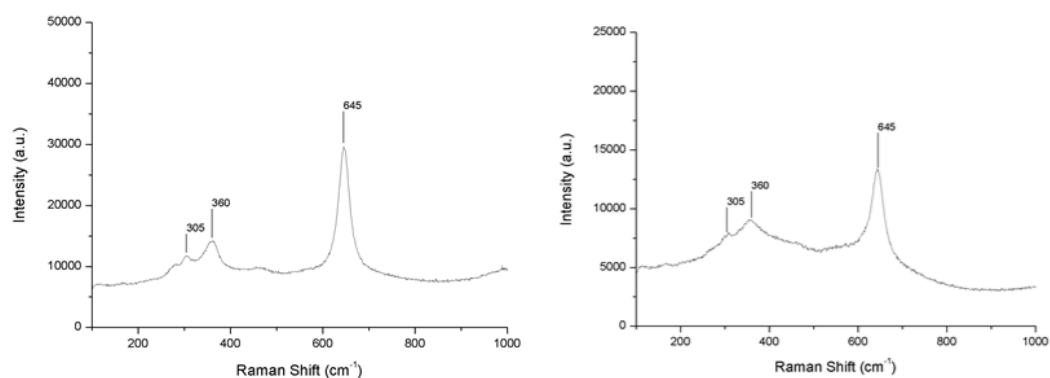
Figure 3.3: Raman spectra of (S)-(-)-phenylalaninol Mn_3O_4 (left) and (R)-(+)-phenylalaninol Mn_3O_4 (right) nanoparticles

agreement with the expected literature values.[26]

Circular dichroism measurements performed on the Mn_3O_4 nanoparticles indicate that they are chiroptically-active, with mirror-image CD spectra obtained as shown in Figure 3.5. The direction of the CD absorbance bands is dependent on whether (S)-(-) or (R)-(+) - phenylalaninol was used during the synthesis. It is important to note that the CD absorbance band with a peak at 325 nm is outside of the region observed for the CD response of the ligand as seen in Fig. 3.5. This indicates that the inorganic component of the nanoparticles is chiral.

76

The CD signals can be attributed to either a chiral surface structure or an induced circular dichroism effect due to presence of chiral phenylalaninol ligands bound to the surface of the Mn_3O_4 nanoparticles. The former mechanism involves a chiral geometric arrangement of the metal oxide whereas the latter argument relies on electronic transitions influenced by the asymmetric orbitals of the chiral capping ligand. It should be stressed that these two mechanisms for the origin of CD in nanomaterials can both be found to be present at the same time in chiral systems.[27] This complicates the assignment of the origin of chirality in the prepared chiral Mn_3O_4 nanoparticles.
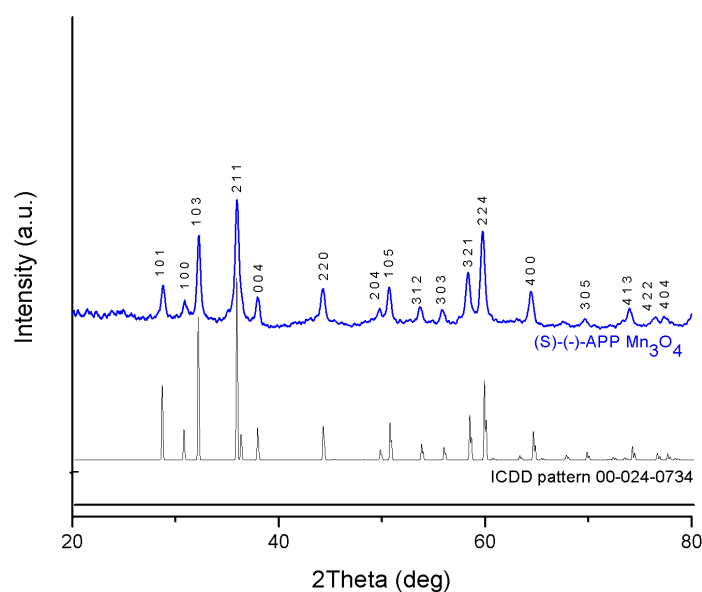
Figure 3.4: XRD pattern of (S)-(-)-phenylalaninol Mn_3O_4 nanoparticles
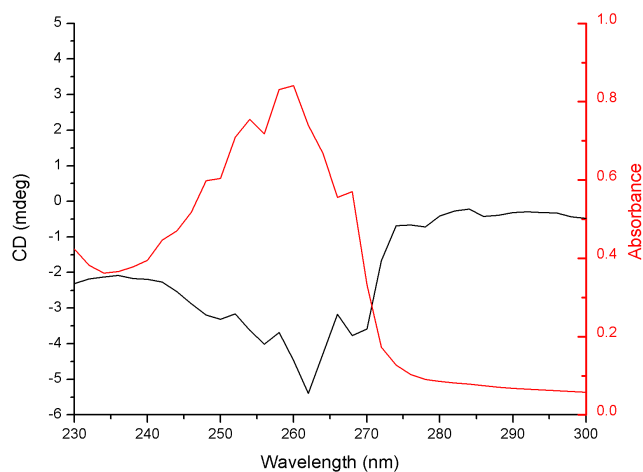
Figure 3.6:   CD spectrum (black) and UV- absorption spectrum (red) of (S)-(-)-phenylalaninol
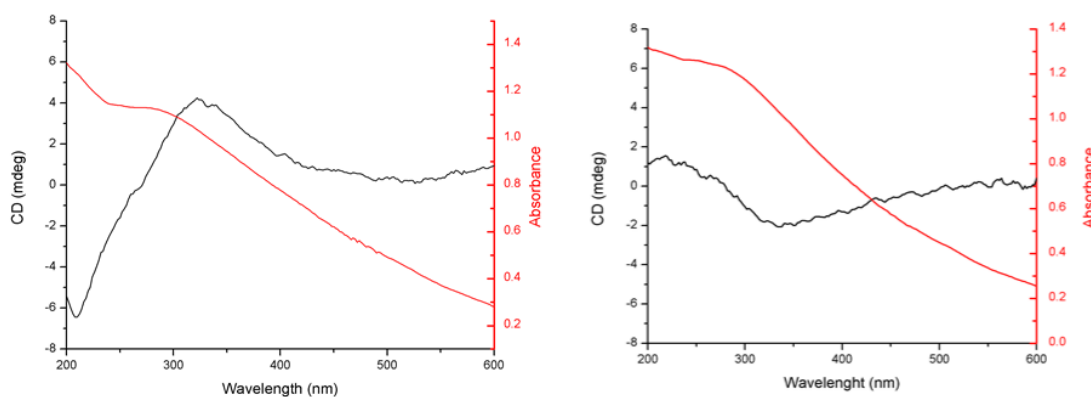
Figure 3.5: CD spectra (black) and UV- absorption spectra (red) of (S)-(-)-phenylalaninol Mn_3O_4 (left) and (R)-(+)-phenylalaninol Mn_3O_4 (right) nanoparticles

3.2.2   Preparation of chiral Mn_3O_4 NPs using other ligands

To investigate the scope of the reaction to produce chiral Mn_3O_4 nanoparticles, a number of different ligands were employed. Amino acids were used as as chiral ligands as there are a number of reports of amino acids being successfully used to prepare chiral nanomaterials.[28–32]

Another group of ligands that were used are a number of "priveliged" ligands from

the field of asymmetric homogeneous catalysis. Previously it has been reported that these ligands can be used to treat MgO or CuO nanoparticles to prepare a asymmetric heterogenous catalyst. The ligands chosen from this class of "priveliged" ligands to prepare chiral Mn_3O_4 include DPEN, BINOL, proline and diaminocyclohexane. A final selected ligandwas (-)-cinchonidine. This was chosen as it has been used to successfully prepare Pt and Au asymmteric hetereogenous catalysts.[33–37] The results of these investigations are summarised in Table 3.1. All of the chiral ligands utilised in the synthesis resulted in chiral Mn_3O_4 NPs except in the case of 2,2'-bis(diphenylphosphino)-1,1'-binaphthyl (BINAP).

Chiral Ligand	Induced optical activity in Mn_3O_4 NPs
Phenylalanol	Yes
Phenylalanine	Yes
Proline	Yes
Tryptophan	Yes
DPEN	Yes
BINOL	Yes
Diaminocyclohexane	Yes
Cinchonidine	Yes
BINAP	No

Table 3.1: Chiral ligands used to synthesise Mn_3O_4 NPs

The CD spectra shown in Figure 3.7 demonstrate that the Mn_3O_4 NPs are chiropticallyactive and we can clearly see the expected mirror image CD signals. The exception to this is in the case of the (-)-cinchonidine functionalised Mn_3O_4 NPs, where only one enantiomer of cinchonidine has been used to synthesise the NPs. These (-)-cinchonidine functionalised Mn_3O_4 NPs display a weak, positive CD signal in the inorganic region of the spectrum which can be ascertained by comparing spectrum (f) in Figure 3.7 with the CD spectrum of the free (-)-cinchonidine (Figure 3.8h, Apppendix A).

A direct, normalised comparison between the CD spectra of the Mn_3O_4 NPs func-
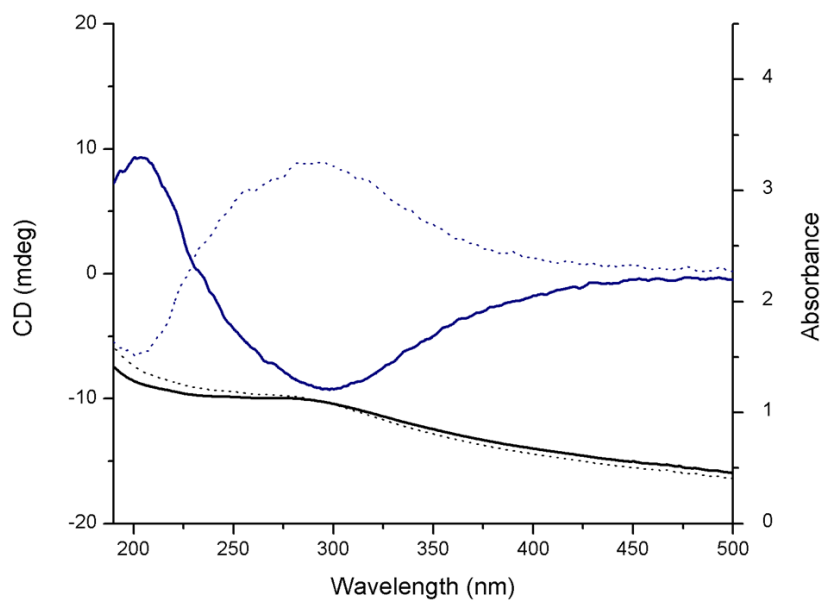
(a) CD spectra (blue) and UV-vis spectra (black) of D- (dotted line) and L- (solid line) phenylalanine functionalised Mn_3O_4 nanoparticles
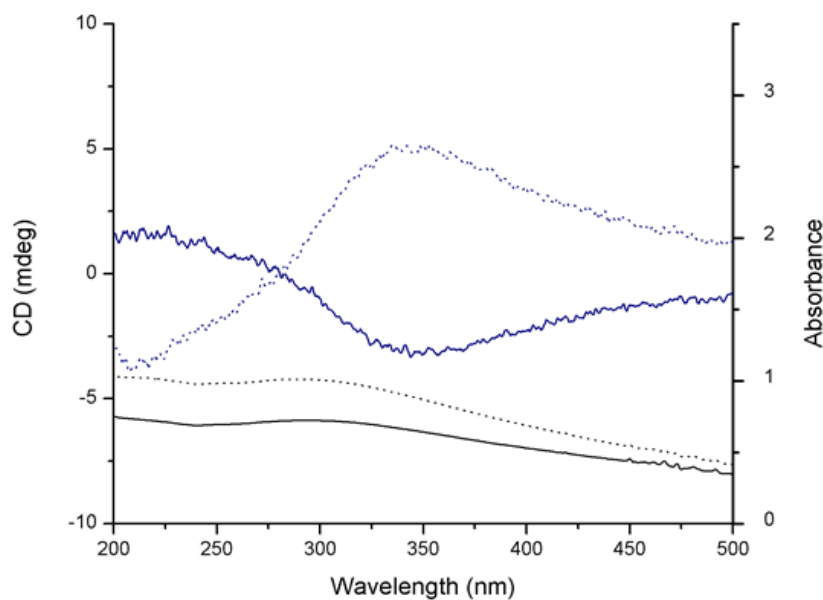
(b) CD spectra (blue) and UV-vis spectra (black) of D- (dotted line) and L- (solid line) proline functionalised Mn_3O_4 nanoparticles

Figure 3.7: CD and g-factor spectra of Mn_3O_4 NPs functionalised with chiral ligands

]
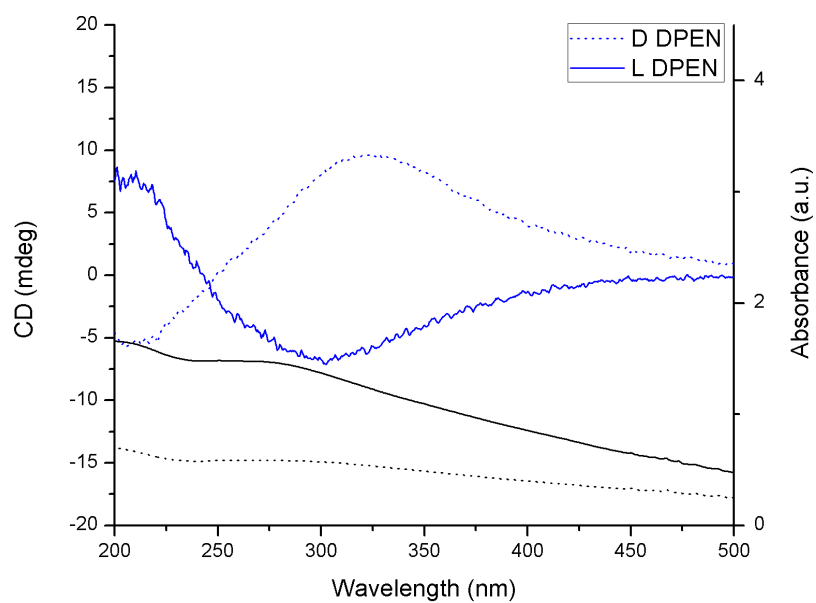
(c) CD and UV-vis spectra of DPEN functionalised Mn_3O_4 NPs
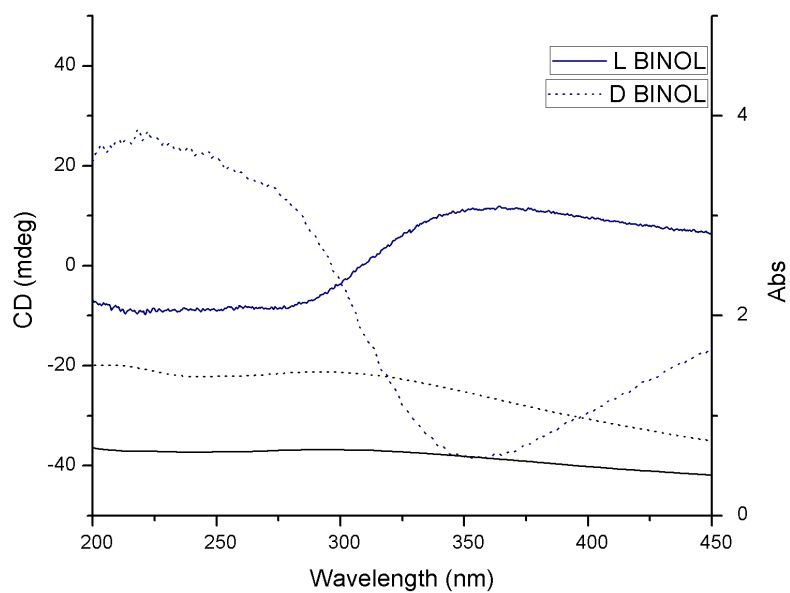
(d) CD and UV-vis spectra of BINOL functionalised Mn_3O_4 NPs
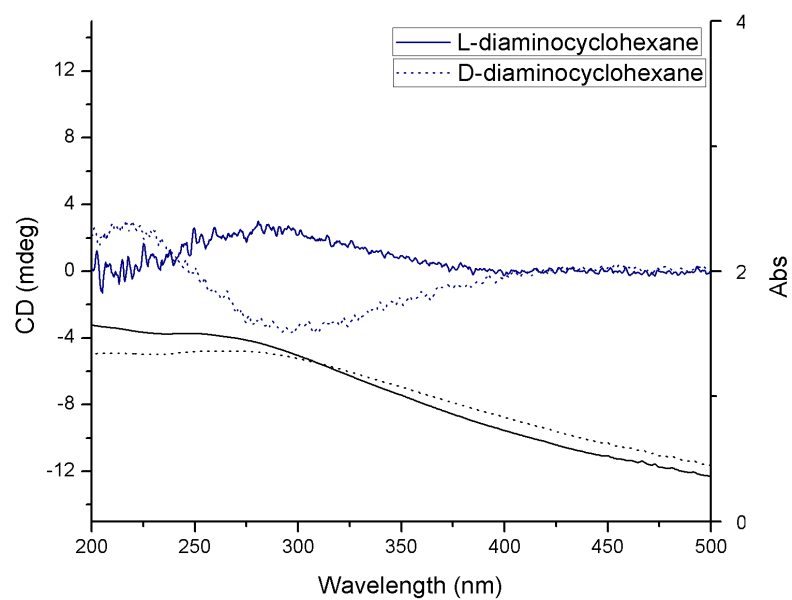
(e) CD and UV-vis spectra of diaminocyclohexane functionalised Mn_3O_4 NPs
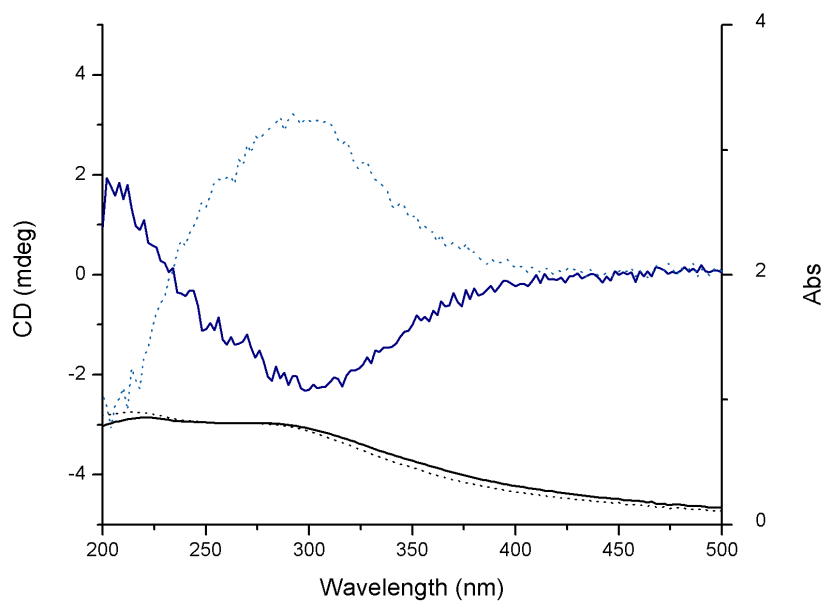
(f) CD spectra (blue) and UV-vis spectra (black) of D- (dotted line) and L- (solid line) tryptophan functionalised Mn_3O_4 nanoparticles
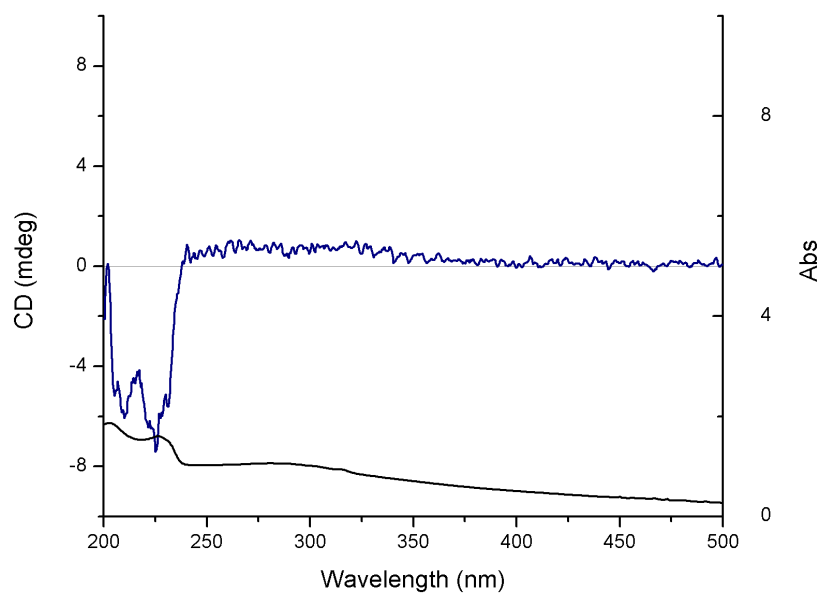
(g) CD spectrum (navy) and UV-vis spectra (black) of (-)-cinchonidine functionalised Mn_3O_4 nanoparticles
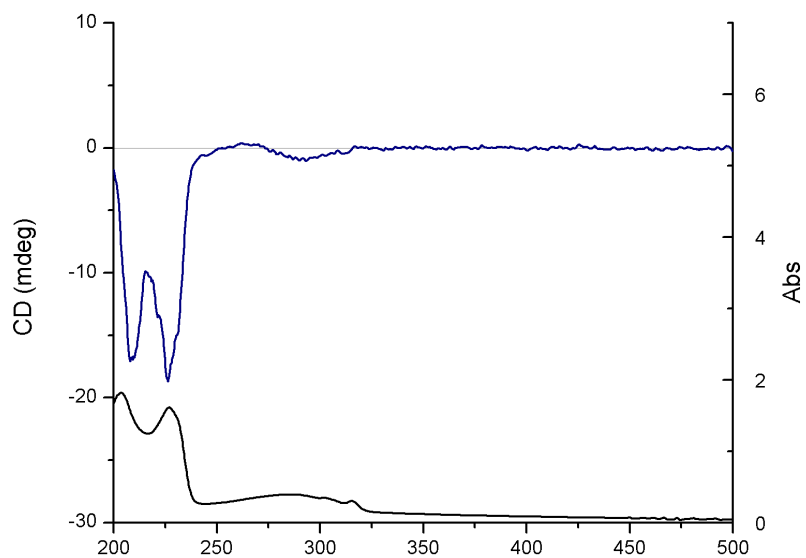
(h) CD spectrum (navy) and UV- absorption spectrum (black) of (-)-cinchonidine

tionalised with chiral ligands can be seen in the g-value curves in Figure 3.9. It can be seen that the intensity of the signals as well as the crossover point in the spectrum varies depending on which chiral ligand is used, phenylalanine functionalised Mn_3O_4 NPs can be seen to have a crossover point of 230 nm, whereas the BINOL functionalised Mn_3O_4 NPs can be seen to have a crossover point of 303 nm. A shift in crossover point has previously been attributed to a change in size in the case of CdS and CdSe quantums dots, with a corresponding shift in the location of the excitonic peaks in the UV-vis spectra[38]. The shift of crossover point cannot be due to the same mechanism in the case of the chiroptically-active Mn_3O_4 NPs. They all have a similar size and do not possess an excitonic peak: they instead have a broad peak in the Mn_3O_4 band-edge region of the spectrum centred on ≈ 300 nm. The differences in crossover point may be explained the fact that a ligand may couple strongly to a metal center, so as to create new electronic states with metal-ligand character, these ligands are known as non-innocent ligands.[39] In the case of the Mn_3O_4-ligand complexes, the mixed-character state that forms delocalises not only over the metal to which the ligand binds, but also over the entire crystal lattice of the Mn_3O_4, such that binding of the ligand creates a new electronic structure without distinct Mn_3O_4 or ligand phases.[40]
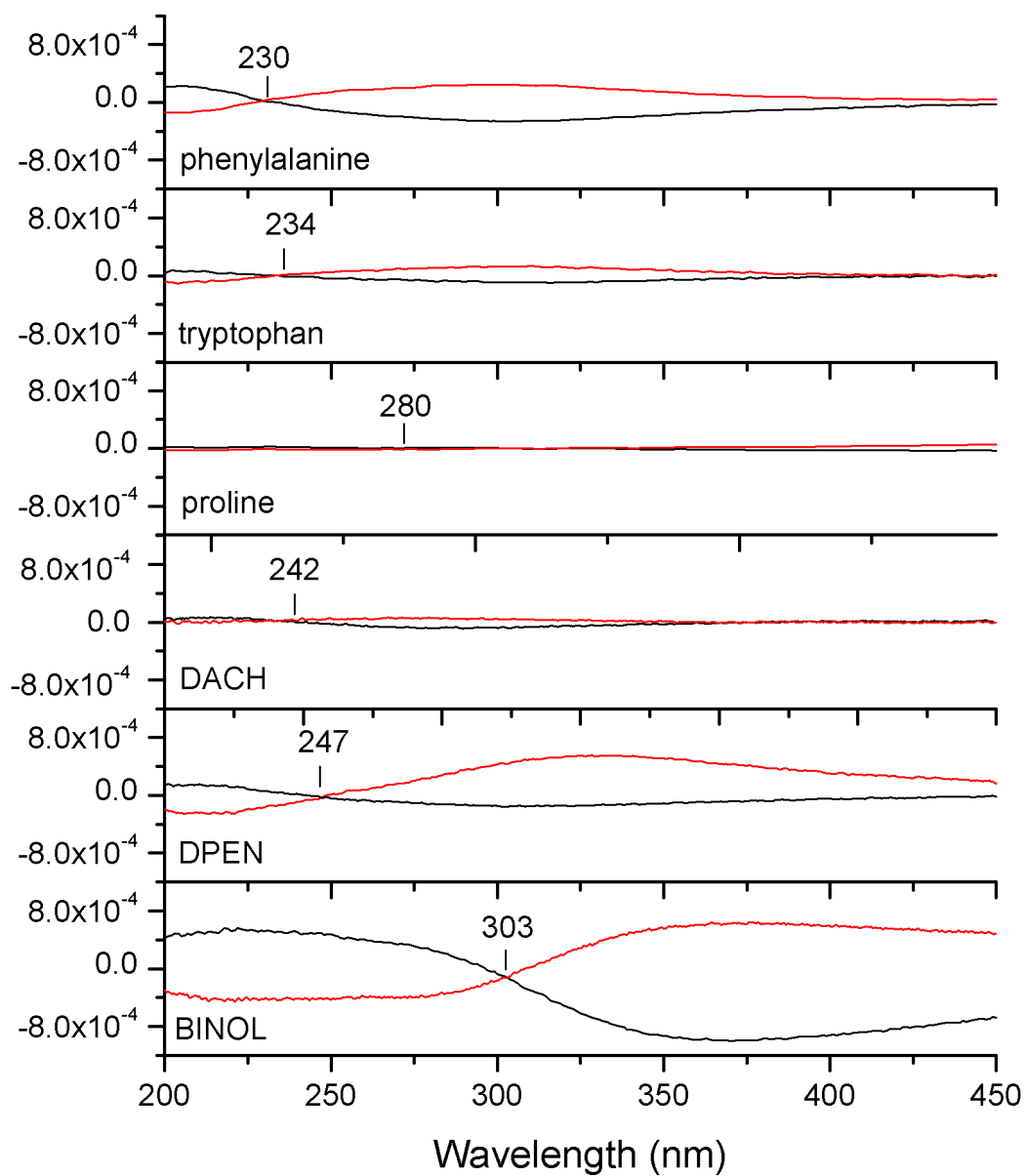
Figure 3.9: g-value spectra of Mn_3O_4 NPs functionalised with chiral ligands, the crossover wavelength is marked in each case

When these systems involving chiral ligands are probed by CD spectroscopy, this new electronic structure can be split into two hybrid levels each preferentially excited by opposite circular polarisations of light, giving rise to the crossover point in the spectrum. The energy of this crossover point is thus related to the energy of the original Mn_3O_4-ligand complex. It can be seen that chiral ligands with the same expected binding motif (as in the case of phenylalanine and tryptophan) exhibit similar crossover points, as they can be expected to have similar Mn_3O_4ligand electronic states.
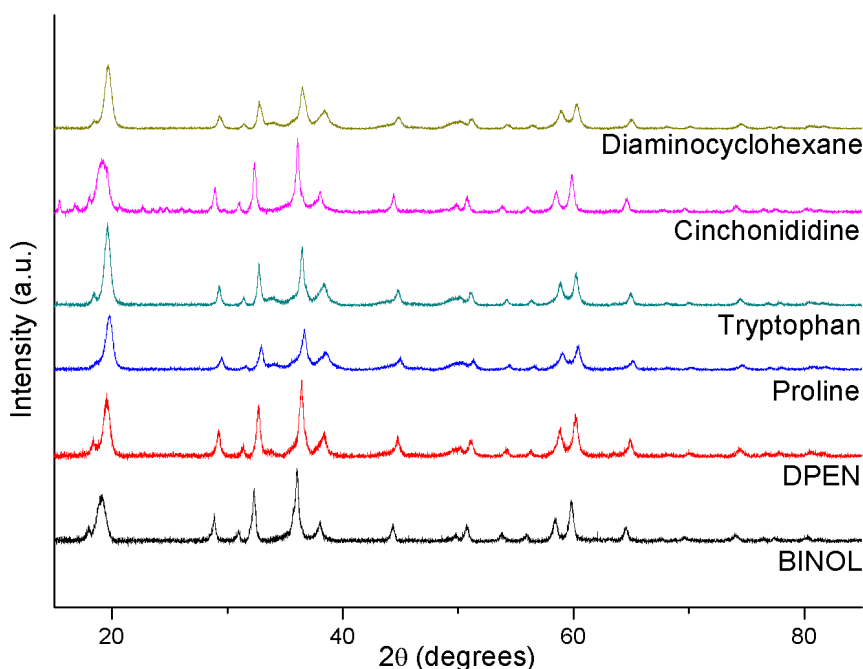
Figure 3.10: XRD patterns of Mn_3O_4 NPs functionalised with chiral ligands

The XRD patterns of the Mn_3O_4 NPs functionalised with chiral ligands can be seen in Figure 3.10. All of the different samples have the same crystal structure which matches the expected pattern for Mn_3O_4, see Figure 3.4.

TEM images of the phenyalalanine functionalised Mn_3O_4 NPs are shown in Figure 3.11. According to the TEM the nanoparticles have a square to rectangular platelet morphology.
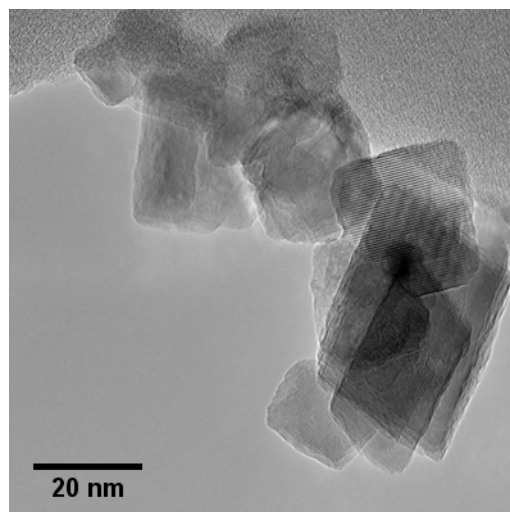
(a) D-phenylalanine functionalised Mn_3O_4
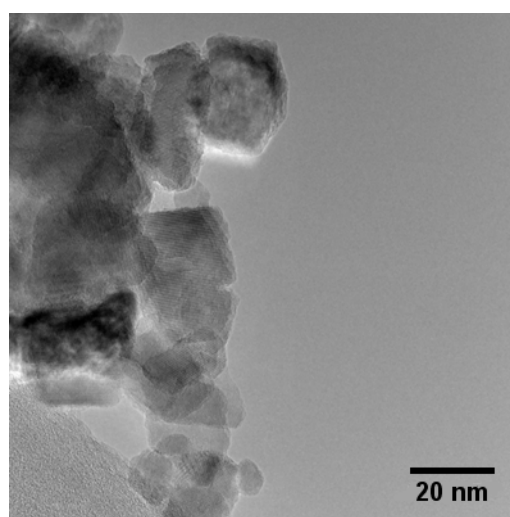
(b) L-phenyalanine functionalised Mn_3O_4

Figure 3.11: TEM images of proline functionalised Mn_3O_4

An investigation was also carried out to test the dependence of the g-value signal strength with the concentration of ligand used in the synthesis. Figure 3.12 displays the dependence of the g-value spectrum with the number of equivalents of BINOL used in the synthesis of the Mn_3O_4 NPs. It can be seen that the signal strength reduces by approximately by half each time the number of BINOL equivalents is halved in the synthesis. This can be explained by a more "sparse" packing of ligand on the crytalline surface of the NPs. The effects of this can be seen in differing reaction yields in the catalytic investigations in the following section.
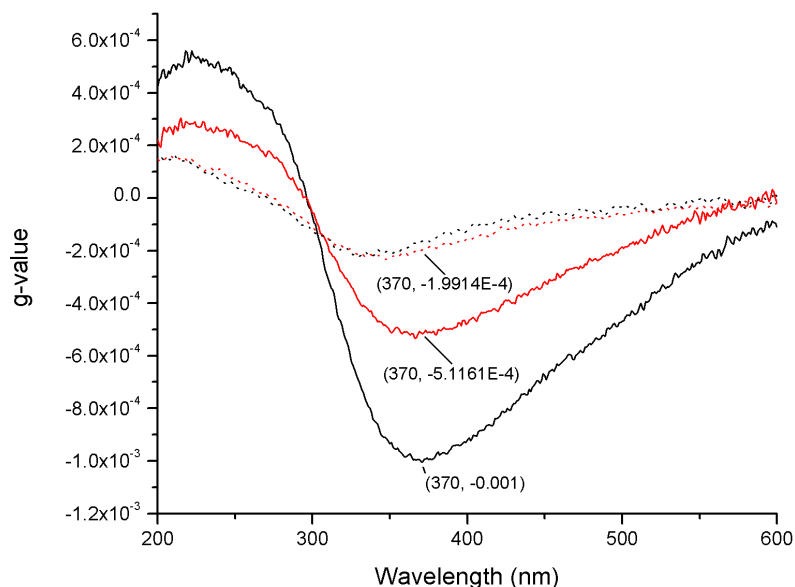
Figure 3.12: g-value spectra of D-BINOL functionalised Mn_3O_4 nanoparticles. 1 eq (black line), 0.5 eq (red line), 0.25 eq (black dotted line) and 0.125 eq (red dotted line)

3.2.3   Catalytic activity

3.2.3.1   Epoxidation

Previously, Mn_3O_4 nanoparticles have been shown to be suitable heterogenous catalysts for the epoxidation of alkenes.[41] Therefore, the chiral Mn_3O_4 NPs were investigated as potential catalysts for an asymmetric epoxidation. Tert-butyl hydroperoxide (TBHP) was chosen as the oxidation agent and trans-chalcone, an α, β -unsaturated ketone, was selected as the alkene. In the latter compound, the alkene is conjugated with a carbonyl group, which decreases the activation energy to be attacked by nucleophilic species (TBHP) at the β-carbon.

The results of the catalytic investigations of the asymmetric epoxidation are summarised in Table 3.2. The epoxidation reaction was carried out in the presence of selected chiral Mn_3O_4 NPs. The epoxidation reaction was first tested with bare NPs that have no stabilising ligand on their surface. The results of these initial tests show that the and Mn_3O_4 NPs are suitable catalysts for the epoxidation reaction, with a
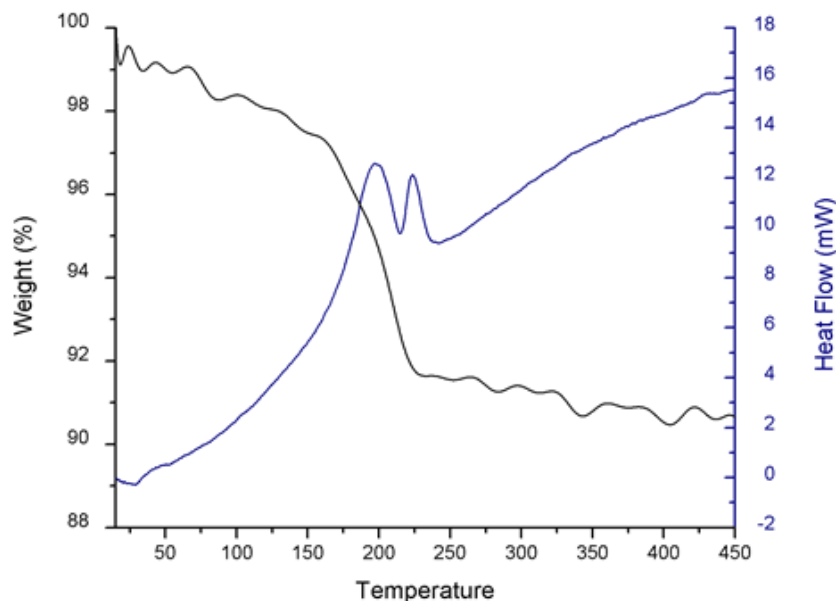
Figure 3.13: TGA (black) and DTA (blue) curves of L-phenylalanine functionalised Mn_3O_4 NPs

yield of 20 % observed. The Mn_3O_4 NPs were prepared by heating at 250 °C for 1 hour to remove the ligands from the NP surface. This temperature was chosen after inspection of the TGA/DTA curves for the Mn_3O_4 NPs (Figure 3.13).

The NPs functionalised with chiral ligands display markedly reduced catalytic activity in all cases. The presence of the chiral ligands leads to reduced yields, accompanied by no enantioselective effect as can be seen by the absence of optical activity in the products of the reactions. The reduction in catalytic activity may be explained by the presence of the chiral ligands on the surface of the NPs. The chiral ligands bind through Lewis-basic centres, these bind to the Lewis-acidic metal centres present on the surface of the NPs. It is these Lewis-acidic centres which catalyse the reaction and once bound to the chiral ligands they are not available to catalyse the epoxidation.

Catalyst	m_{cat} (g)	time (hrs)	Yield (%)	$[\alpha]_D^{25}$
no catalyst	-	72	0	-
Mn_3O_4	0.03	24	11	0
Mn_3O_4	0.03	48	20	0
D-DPEN (1 eq.) Mn_3O_4	0.03	48	3	0
D-BINOL (1 eq.) Mn_3O_4	0.03	48	5	0
D-diaminocyclohexane (1 eq.) Mn_3O_4	0.03	48	5	0

Table 3.2: Catalytic epoxidation of chalcone by TBHP

3.2.3.2 Oxyalkylation

The oxyalkylation reaction between vinylarenes and cyclic ethers has been demonstrated by Sun *et al.* to proceed in the presence of Mn_3O_4 NPs.[9] High regioselectivity and good yields have been reported in this catalytic system. Thus, chiral Mn_3O_4 were used to catalyse this reaction. In a manner analogous to the epoxidation carried out in the previous section, bare Mn_3O_4 and TiO_2 NPs were used to determine their suitablility for catalysing the oxyalkylation reaction. Yields of 8 and 24 % were obtained, respectively.

It was observed that the reaction did not proceed in the cases where a chiral capping ligand was present on the Mn_3O_4 NPs. This may be due to the chiral ligands binding to and "blocking" access to the catalytic metal centres on the surface of the NPs. To test this assumption, a series of D-BINOL functionalised Mn_3O_4 NPs were prepared which had varying amounts of the D-BINOL capping ligand present. These were shown by their g-value spectra to have varying amounts of optical activity, as expected by the varying amounts of D-BINOL used in their preparation (Figure 3.12). As the amount of D-BINOL present on the surface of the nanoparticles is decreased, the yield of the oxyalkylation starts to increase. This lends weight to the assertion that the presence of the chiral capping ligands on the surface of the NPs is

Catalyst	m_{cat} (g)	time (hrs)	Yield (%)	$[\alpha]_D^{25}$
no catalyst	-	48	0	-
Mn_3O_4	0.05	24	24	-
D-DPEN (1 eq.) Mn_3O_4	0.05	48	0	-
D-proline (1 eq.) Mn_3O_4	0.05	48	0	-
D-diaminocyclohexane (1 eq.) Mn_3O_4	0.05	48	0	-
D-BINOL (1 eq.) Mn_3O_4	0.05	48	0	-
D-BINOL (0.5 eq.) Mn_3O_4	0.05	48	0	-
D-BINOL (0.25 eq.) Mn_3O_4	0.05	48	< 1	0
D-BINOL (0.125 eq.) Mn_3O_4	0.05	48	3	0

Table 3.3: Catalytic oxyalkylation of anethole

"'blocking" access of the reagents to the catalytic centres on the surface of the NPs, leading to no catalytic effects being present. The products from these reactions did not exhibit any optical activity, thus there is no enantioselective catalysis taking place.

3.2.3.3   Aldol

The aldol reaction between acetone and p-nitrobenzaldehyde was also investigated using chiral Mn_3O_4 and TiO_2 NPs as catalysts. Metal oxide[42,43] and metal chalcogenide[44] NPs funcitonalised with chiral ligands have been demonsrated to be suitable enantioselective catalysts for aldol reactions.

Table 3.4 shows the results of the catalytic investigations of Mn_3O_4 and TiO_2 NPs in the aldol condensation between acetone and p-nitrobenzaldehyde. Bare Mn_3O_4 have no catalytic activity for the aldol reaction. D-proline funcionalised Mn_3O_4 NPs however, can be seen to catalyse the aldol reaction.

Catalyst	m_{cat} (g)	Yield (%)	$[\alpha]_D^{25}$
no catalyst	-	0	-
Mn_3O_4	0.05	0	-
D-proline (1 eq.) Mn_3O_4	0.05	10	0
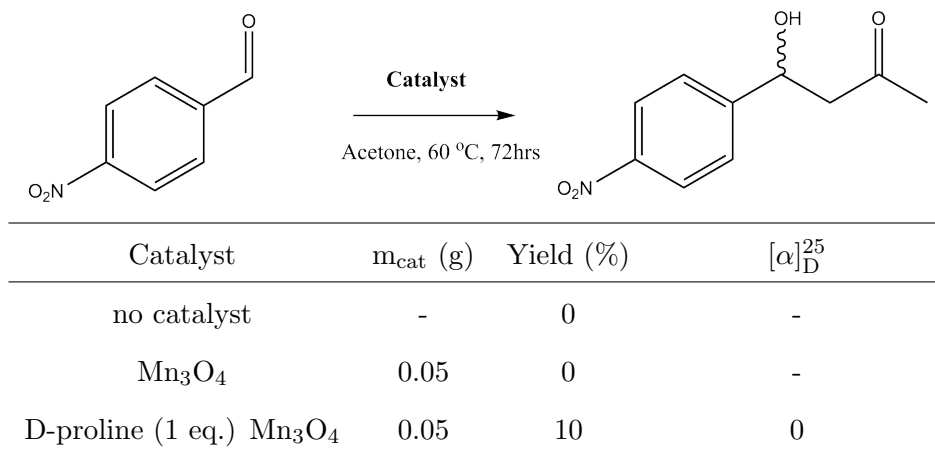
Table 3.4: Catalytic aldol reaction using Mn_3O_4 and TiO_2 NPs

Investigation of the L-proline functionalised Mn_3O_4 NPs after the aldol conden-station indicates that they are losing their optical activity during the course the the reaction (Figure 3.14). The g-value spectra of the NPs after the reaction has flattened-out and almost lost the characteristic Cotton-effect that is present in the g-value spectra of the chiral Mn_3O_4 NPs. This may be explained due to the L-proline on the surface of the Mn_3O_4 NPs dissociating into the reaction solution during heating. The "free" L-proline can deprotonate the acetone and catalyse the aldol reaction.[45]
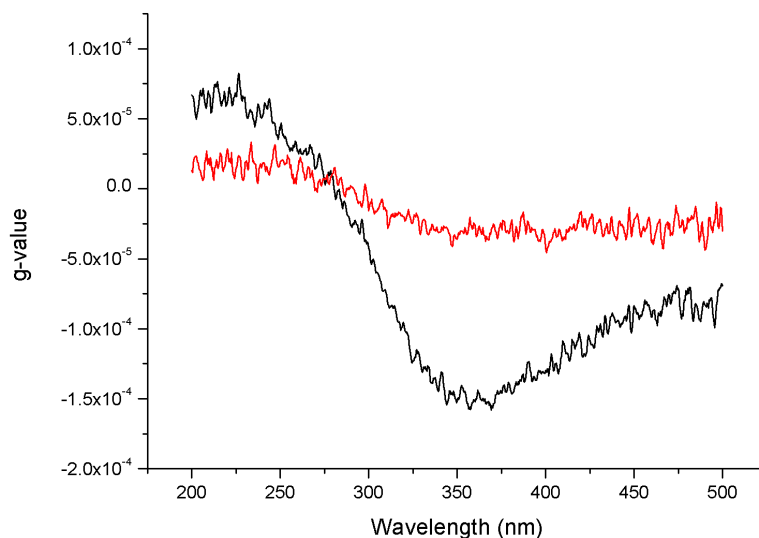
Figure 3.14: g-value spectra of (-)-proline functionalised Mn_3O_4 nanoparticles, before (black) and after (red) catalytic aldol reaction

3.2.4 Electrochemical Oxidation

It has been reported that the surface of metal oxide nanoparticles may be "imprinted" with a suitable ligand during synthesis.[46,47] The ligand can be removed by a heat treatment step and the resulting "molecular imprint" is left behind on the metal oxide suface. These metal oxides then exhibit preferential photocatalytic degradation of the imprint molecule. This has even been shown to be the case in the photoelectrochemical oxidation of D- or L-phenylalanine by a chiral ZnO surface that has itself been molecularly imprinted by either D- or L-phenylalanine as seen in Fig 3.15.[48] The exact nature of this "molecular imprint" is poorly understood however.

Mn_3O_4 nanoparticles can be used as part of a working electrode for a variety of electrochemical redox reactions.[2,49] Using the concepts of molecular imprinting outlined above, it is possible to test the nature of the chirality that is present on the surface of the Mn_3O_4 nanoparticles. If there exists a "molecular imprint" of a the chiral ligand (an amino acid, for example) on the surface of the Mn_3O_4, then it is
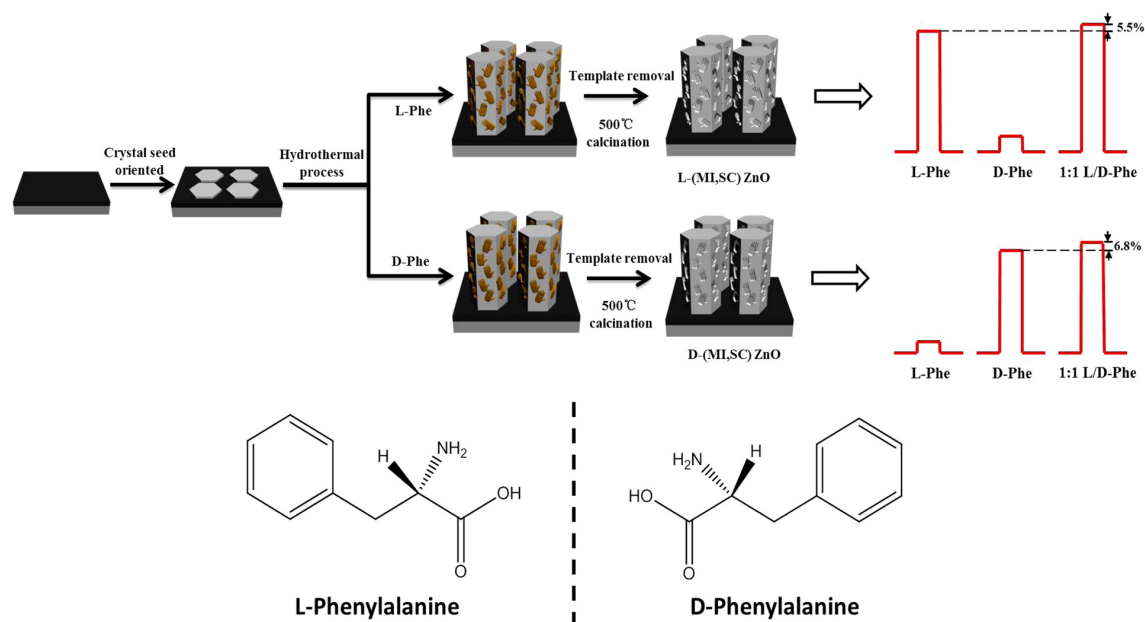
Figure 3.15: Enantioselective photoelectrochemical oxidation of D- or L-phenylalanine by a chiral ZnO surface. Figure reproduced from Chen *et al.*[48]

conceivably possible to discern this by using a chiral Mn_3O_4 nanoparticles as part of a working electrode for electrochemical redox reactions in the manner shown by Chen *et al.*[48] It is expected that a working electrode made from nanoparticles that have a chiral "molecular imprint" on their surface would exhibit preferential redox behaviour for that particular enantiomer due to molecular recognition . This would manifest itself as a higher current response in the cyclic voltagramm.

Working electrodes 1 cm^2 in area were prepared by applying a film of L- or D-tryptophan functionalised Mn_3O_4 NPs on conductive indium tin oxide coated glass using the doctor blade technique. The working electrodes were then tested in an electrochemical redox reaction against a solution of 10 nM D-tryptophan. The results of the electrochemical redox reaction can be seen in Figure 3.16. According to the data that there is no statistically significant difference between the working electrodes made from either the D- or L-tryptophan functionalised Mn_3O_4 NPs. Thus the conclusion of this result is that there is no chiral "imprint" present and the chiroptical activity is solely due to the presence of the ligand. This is especially clear when looked at in conjunction with the loss of CD after calcination of the chiroptically-active Mn_3O_4 NPs (Figure 3.17)
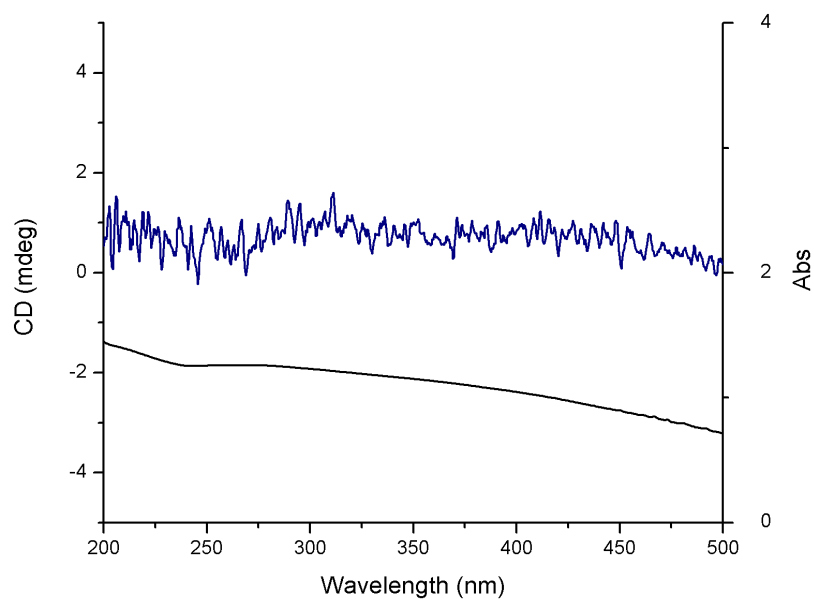
Figure 3.17: CD spectrum (navy) and UV- absorption spectrum (black) of (-)-proline functionalised Mn_3O_4 after 1 hour at 175 °C
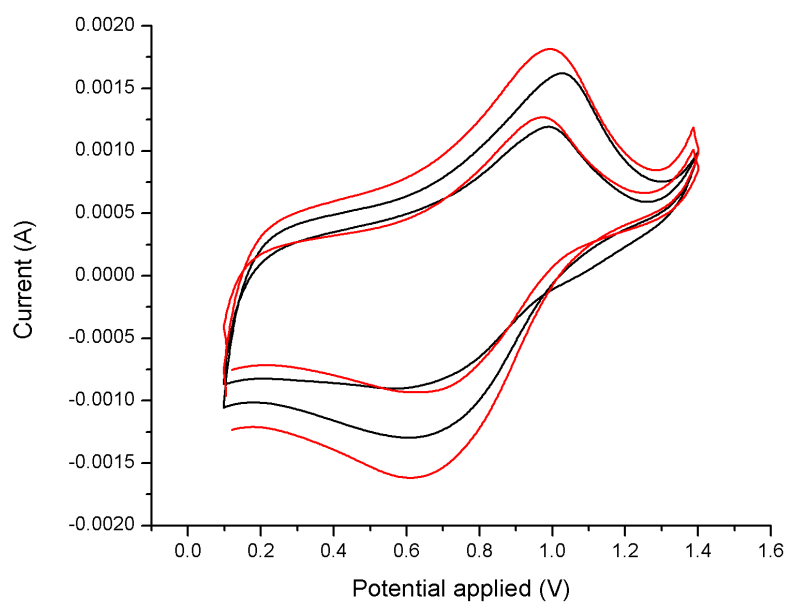
Figure 3.16: Cyclic voltagramm of D- (black) and L- (red) tryptophan functionalised Mn_3O_4 working electrode vs 10 nM D-tryptophan

3.2.5 Biological activity

This section of our work was carried out by a collaborator, Dr Rebecca Reilly (UCD). Mn_3O_4 NPs have been reported in the literature to possess properties making them suitable for both antibacterial and anticancer applications.[12–16] Chiroptically-active Mn_3O_4 NPs functionalised with L- or D-proline, the synthesis and characterisation of which have been detailed earlier in this chapter were investigated for potential anti-cancer properties.

BT-549 cells are an aggressive triple-negative breast cancer (TNBC) cell line. Reduction of (3-(4,5-dimethylthiazol-2-yl)-2,5-diphenyltetrazolium (MTT) to formazan crystals is a measure of metabolism. When cells are active, they convert MTT to formazan which results in a colour change from yellow to purple.[50] When cells die or have reduced viability as a result of incubation with an agent, they lose the conversion ability, i.e. more intense purple corresponds to increased viability.

An initial investigation was carried out to test the activity of the L-proline and D-proline functionalised Mn_3O_4 NPs. BT-549 cells were treated with NPs at concentrations ranging from 5 µg/ml to 640 µg/ml for 24 hours. After treatment optical density of each treatment condition was read at 590 nm on a Spectramax M3 microplate reader. This analysis was performed using four technical replicates. There was no reduction in cell viability in the treatment conditions. In treatment conditions: 5, 80, 160, 320 and 640 µg/ml there was a significant increase in optical density. This may explained as being due to difficulties with solubility and as a result skewed optical readings. The NPs themselves are interfering with the analysis due in part to their poor solubility, making this technique unsatisfactory to discover any potential anticancer activity present. This was the case in both the D- and L-proline functionalised Mn_3O_4 NPs. The results of these investigations can be seen in Figure 3.18 Possible improvements to this he use of lipofectamine transfection method to enhance uptake of nanoparticles into cells.
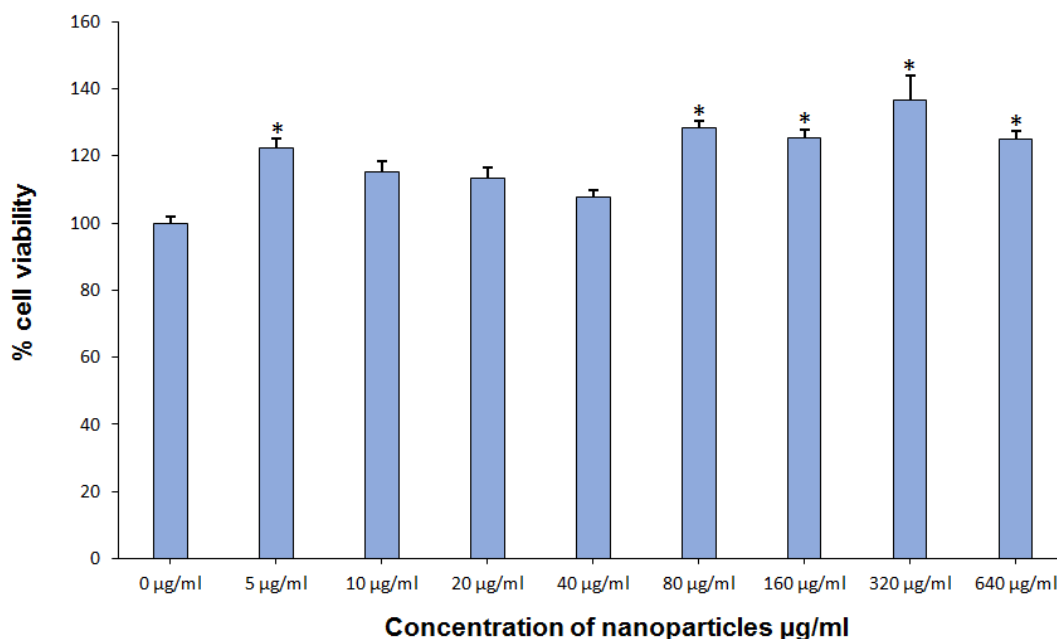
Figure 3.18: Results of MTT assay, asterisk indicates statistical significance

3.2.6 Crystallisation of chiral MOF

It has been reported that a chiral crystalline nanomaterial may be prepared by using a homochiral metal organic framework (MOF) as a template.[51] This synthetic strategy was followed in an attempt to create a chiral manganese oxide material starting from a chiral MOF template. A chiral MOF was first prepared from mangansese chloride and sodium L-tartrate according to a procedure previously reported in the literature.[52] The XRD pattern obtained from the synthesis matches the reported literature result (Figure 3.19), thus confirming the identity of the chiral MOF.[52] The chiral MOF was then analysed by diffuse-reflectance circular dichroism (DR-CD) and displays an expected CD signal as seen in Figure 3.19.

The chiral MOF was then analysed by DTA and TGA to determine the temperature at which decomposition and subsequent crystallisation to the oxide takes place. It can be seen from the DTA curve in Figure 3.21 that there are two exothermic peaks at 352 and 392 degrees at which crystallisation takes place. The chiral MOF was then calcined at 400 °C for 1 hour and the products analysed again by DR-CD. It can be seen from these investigations that the product is no longer chiroptically-active
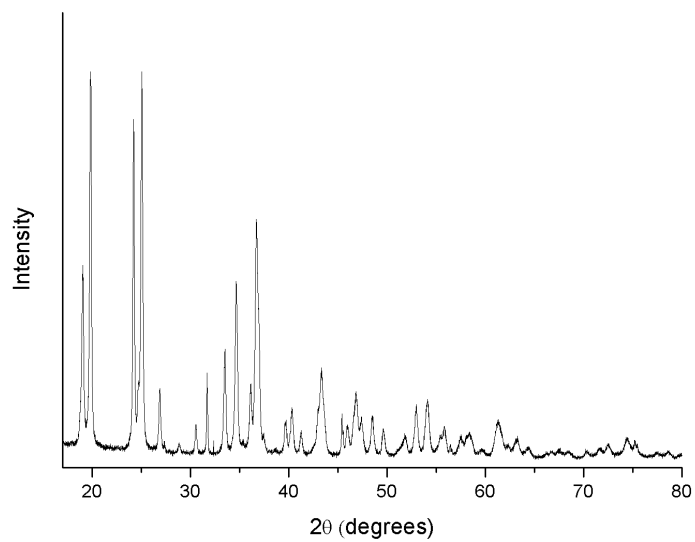
(a) XRD pattern of chiral MOF
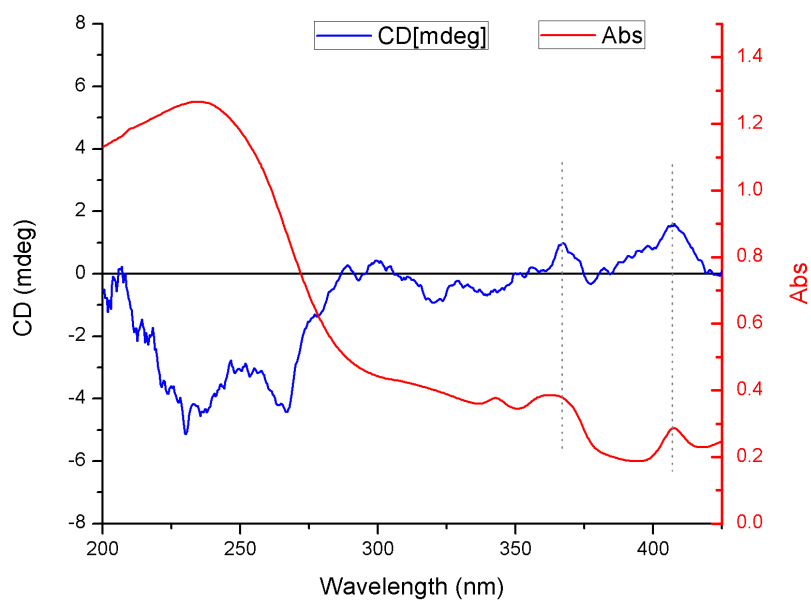
(b) DR-CD (blue) and corresponding UV-vis (red) of chiral Mn-based MOF

Figure 3.19: XRD and CD characterisation of chiral MOF
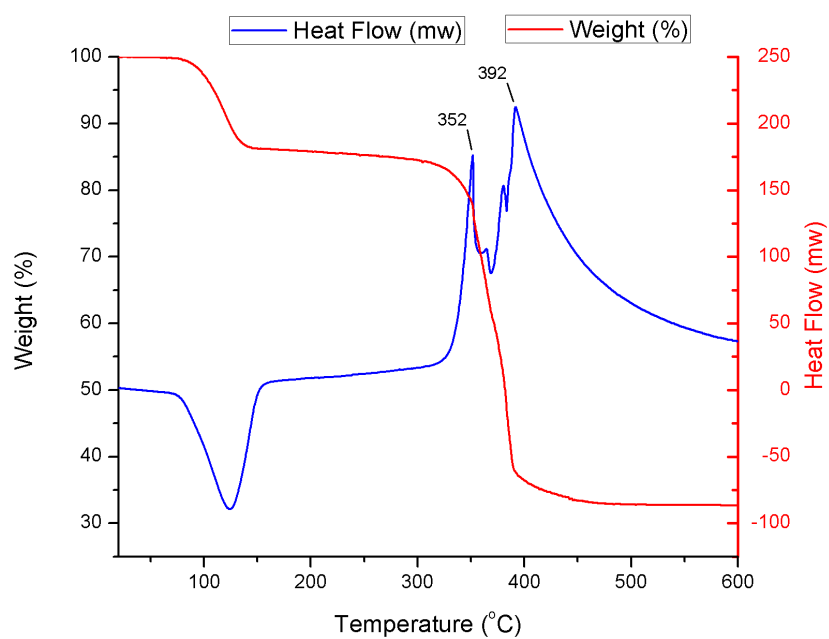
Figure 3.21: TGA (red) and DTA (blue) curves of chiral Mn-based MOF

(Figure 3.22). Thus, this technique is an unsuitable method for the preparation of a chiral nanomaterial in this case.
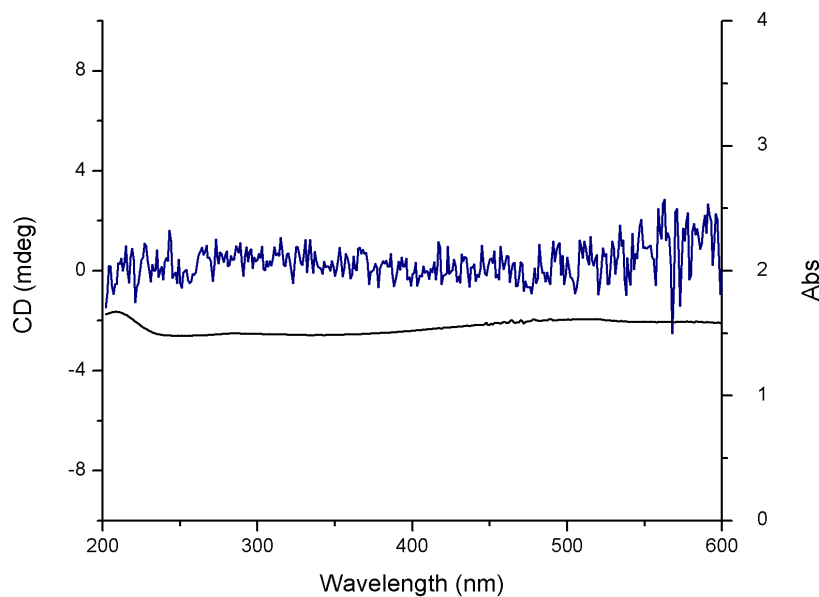
Figure 3.22: DR-CD (blue) and DR UV-vis (black) of chiral Mn-based MOF calcined at 400 °C for 1 hour

3.3   Conclusions

Thus, a range of novel chiroptically-active Mn_3O_4 NPs have been prepared using functionalisation with a variety of chiral ligands. Through the catalytic investigations that were carried out, it is evident that the presence chiral capping ligands lead to a reduction in the catalytic properties of the Mn_3O_4 NPs. The chiroptically-active Mn_3O_4 NPs were also used successfully as part of a working electrode for the electrochemical oxidation of L-tryptophan, but again there was no enantioselective effect present. The chiroptically-active Mn_3O_4 NPs were also tested for activity against against breast cancer cells, the results of this investigation was inconclusive. Finally, a chiral MOF was also investigated as a means to prepare a chiral metal oxide, the resulting material did not display any chiroptical activity.

References

(1) Armstrong, A. R.; Bruce, P. G. *Nature* **1996**, *381*, 499–500.

(2) Wang, Y.-g.; Cheng, L.; Li, F.; Xiong, H.-m.; Xia, Y.-y. *Chemistry of Materials* **2007**, *19*, 2095–2101.

(3) Salazar-Alvarez, G.; Sort, J.; Suriñach, S.; Baró, M. D.; Nogués, J. *Journal of the American Chemical Society* **2007**, *129*, 9102–9108.

(4) Bai, Z.; Sun, B.; Fan, N.; Ju, Z.; Li, M.; Xu, L.; Qian, Y. *Chemistry – A European Journal* **2012**, *18*, 5319–5324.

(5) Ahmed, K. A. M.; Huang, K. *Arabian Journal of Chemistry*, DOI: `http://dx.doi.org/10.1016/j.arabjc.2014.08.014`.

(6) Chen, C.; Jian, H.; Mai, K.; Ren, Z.; Wang, J.; Fu, X.; Fan, C.; Sun, C.; Qian, G.; Wang, Z. *European Journal of Inorganic Chemistry* **2014**, *2014*, 3023–3029.

(7) Ahmed, K. A. M.; Zeng, Q.; Wu, K.; Huang, K. *Journal of Solid State Chemistry* **2010**, *183*, 744–751.

(8) Qi, B.; Lou, L.-L.; Yu, K.; Bian, W.; Liu, S. *Catalysis Communications* **2011**, *15*, 52–55.

(9) Sun, H.; Zhang, Y.; Guo, F.; Zha, Z.; Wang, Z. *The Journal of Organic Chemistry* **2012**, *77*, 3563–3569.

(10) Sun, H.-y.; Hua, Q.; Guo, F.-f.; Wang, Z.-y.; Huang, W.-x. *Advanced Synthesis & Catalysis* **2012**, *354*, 569–573.

(11) Sun, H.; Zhang, Y.; Guo, F.; Yan, Y.; Wan, C.; Zha, Z.; Wang, Z. *European Journal of Organic Chemistry* **2012**, *2012*, 480–483.

(12) Chowdhury, A. N.; Azam, M. S.; Aktaruzzaman, M.; Rahim, A. *Journal of Haz-ardous Materials* **2009**, DOI: `10.1016/j.jhazmat.2009.07.129`.

(13) Belkhedkar, M.; Ubale, A. *Journal of Molecular Structure* **2014**, DOI: `10.1016/j.molstruc.2014.03.050`.

(14) Chen, Q.; Wei, C.; Gao, F.; Pang, H.; Lu, Q. *Nanoscale* **2013**, DOI: `10.1039/c3nr03453d`.

(15) Khan, S.; Ansari, A.; Khan, A.; Abdulla, M.; Al-Obeed, O.; Ahmad, R. *MedChem-Comm* **2016**, DOI: `10.1039/c6md00219f`.

(16) Gotić, M.; Ivanković, S.; Musić, S.; Prebeg, T. **2009**, DOI: `10.1135/cccc2009047`.

(17) Pan, D; Schmieder, A. H.; Wickline, S. A.; Lanza, G. M. *Tetrahedron* **2011**, DOI: `10.1016/j.tet.2011.07.076`.

(18) Xiao, J.; Tian, X. M.; Yang, C.; Liu, P.; Luo, N. Q.; Liang, Y.; Li, H. B.; Chen, D. H.; Wang, C. X.; Li, L.; Yang, G. W. *Scientific Reports* **2013**, DOI: `10.1038/srep03424`.

(19) Wang, A.; Guo, M.; Wang, N.; Zhao, J.; Qi, W.; Muhammad, F.; Chen, L.; Guo, Y.; Nguyen, N.-T.; Zhu, G. *Nanoscale* **2014**, DOI: `10.1039/c3nr05687b`.

(20) Savla, R.; Garbuzenko, O. B.; Chen, S.; Rodriguez-Rodriguez, L.; Minko, T. *Phar-maceutical Research* **2014**, DOI: `10.1007/s11095-014-1436-x`.

(21) Duan, Y.; Liu, X.; Han, L.; Asahina, S.; Xu, D.; Cao, Y.; Yao, Y.; Che, S. *Journal of the American Chemical Society* **2014**, *136*, 7193–7196.

(22) Jana, S.; Basu, S.; Pande, S.; Ghosh, S. K.; Pal, T. *The Journal of Physical Chem-istry C* **2007**, *111*, 16272–16277.

(23) Leem, G.; Sarangi, S.; Zhang, S.; Rusakova, I.; Brazdeikis, A.; Litvinov, D.; Lee, T. R. *Crystal Growth & Design* **2008**, *9*, 32–34.

(24) Rusakova, I.; Ould-Ely, T.; Hofmann, C.; Prieto-Centurión, D.; Levin, C. S.; Halas, N. J.; Lüttge, A.; Whitmire, K. H. *Chemistry of Materials* **2007**, *19*, 1369–1375.

(25) Sambasivam, S; Li, G. J.; Jeong, J. H.; Choi, B. C.; Lim, K. T.; Kim, S. S.; Song, T. K. *Journal of Nanoparticle Research* **2012**, *14*, 1–9.

(26) X-ray Diffraction pattern of Haussmanite., English, 1972.

(27) Elliott, S. D.; Moloney, M. P.; Gun'ko, Y. K. *Nano Letters* **2008**, *8*, 2452–2457.

(28)   Moloney, M. P.; Govan, J.; Loudon, A.; Mukhina, M.; Gun'ko, Y. K. *Nat. Protocols*
        2015, *10*, 558–573.

(29)   Tohgha, U.; Varga, K.; Balaz, M. *Chemical Communications* **2013**, *49*, 1844–1846.

(30)   Govan, J. E.; Jan, E.; Querejeta, A.; Kotov, N. A.; Gun'ko, Y. K. *Chemical Com-
        munications* **2010**, DOI: `10.1039/c0cc00930j`.

(31)   Nakashima, T.; Kobayashi, Y.; Kawai, T. *Journal of the American Chemical Society*
        2009, DOI: `10.1021/ja902800f`.

(32)   Gun'ko, Y.; Kelly, J.; Moloney, M. *CHEMICAL COMMUNICATIONS* **2007**, DOI:
        `10.1039/b704636g`.

(33)   Blaser, H. U.; Studer, M. Cinchona-modified platinum catalysts: From ligand accel-
        eration to technical processes., 2007.

(34)   Studer, M.; Burkhardt, S.; Blaser, H.-U. *Chemical Communications* **1999**, DOI:
        `10.1039/A905113I`.

(35)   Sutherl, I. M.; Ibbotson, A; Moyes, R. B.; Wells, P. B. *Journal of Catalysis* **1990**,
        125, 77 –88.

(36)   Blaser, H. U.; Jalett, H. P.; Wiehl, J *Journal of Molecular Catalysis* **1991**.

(37)   Meheux, P. A.; Ibbotson, A.; Wells, P. B. *Journal of Catalysis* **1991**, DOI: `10.
        1016/0021-9517(91)90297-H`.

(38)   Ben-Moshe, A.; Teitelboim, A.; Oron, D.; Markovich, G. *Nano Letters* **2016**, DOI:
        `10.1021/acs.nanolett.6b03143`.

(39)   Ray, K.; Petrenko, T.; Wieghardt, K.; Neese, F. Joint spectroscopic and theoretical
        investigations of transition metal complexes involving non-innocent ligands., 2007.

(40)   Frederick, M. T.; Amin, V. A.; Weiss, E. A. *Journal of Physical Chemistry Letters*
        2013, DOI: `10.1021/jz301905n`.

(41)   Askarinejad, A.; Bagherzadeh, M.; Morsali, A. *Applied Surface Science* **2010**, *256*,
        6678–6682.

(42)   Kantam, M. L.; Ramani, T.; Chakrapani, L.; Kumar, K. V. *Tetrahedron Letters*
        2008, *49*, 1498–1501.

(43)   Choudary, B. M.; Chakrapani, L.; Ramani, T.; Kumar, K. V.; Kantam, M. L. *Tetra-
        hedron* **2006**, *62*, 9571–9576.

(44)   Shah, E.; Soni, H. P. *RSC Advances* **2013**, *3*, 17453–17461.

(45)   List, B.; Lerner, R. A.; Barbas III, C. F.; Barbas, C. F.; III *J. Am. Chem. Soc.*
        2000, DOI: `10.1021/ja994280y`.

(46)   Luo, X.; Deng, F.; Min, L.; Luo, S.; Guo, B.; Zeng, G.; Au, C. *Environmental Science*
        & Technology **2013**, *47*, 7404–7412.

(47)   Sharabi, D.; Paz, Y. *Applied Catalysis B: Environmental* **2010**, *95*, 169–178.

(48)   Chen, C.; Shi, H.; Zhao, G. *The Journal of Physical Chemistry C* **2014**, *118*, 12041–
        12049.

(49)   Dong, R.; Ye, Q.; Kuang, L.; Lu, X.; Zhang, Y.; Zhang, X.; Tan, G.; Wen, Y.; Wang,
        F. *ACS Applied Materials and Interfaces* **2013**, DOI: `10.1021/am402257y`.

(50)   Mosmann, T. *Journal of Immunological Methods* **1983**, DOI: `10.1016/0022-`
        `1759(83)90303-4`.

(51)   Kuang, X.; Ma, Y.; Zhang, C.; Su, H.; Zhang, J.; Tang, B. *Chemical Communications*
        2015, *51*, 5955–5958.

(52)   Saha, R.; Roychowdhurry, A.; Steele, I. M.; Biswas, S.; Kumar, S. *J. Indian Chem*
        Soc. **2013**, *90*, 1043–1052.

Chapter 4

Chiroptically-Active ZnO Nanoparticles

4.1 Introduction

ZnO is a conventional wide band gap semiconductor (3.37 eV) that has attracted attention as a potential candidate for a variety of biomedical applications, such as antibacterial agents,[1,2] biological imaging,[3] and a particular emphasis on anti-cancer applications.[4–6] The interest in ZnO is driven by it's multi-modal properties as there are three distinct ways in which it can be applied: for targeted cellular imaging due to it's luminescent properties,[7,8] for it's ability to induce cell apoptosis selectively in cancerous cells,[9–12] and finally as a drug delivery vehicle.[13,14]

The mechanism of cellular apoptosis has been attributed to two different mechanisms, the generation of reactive oxygen species (ROS) due to the presence of ZnO NPs which then induce cellular damage in the surrounding medium,[10] or as a consequence of the release of Zn^{2+} in the acidic interior of a cancerous cell.[12–14] One of the hallmarks of a cancerous cell is a lower pH due to lactate secretion from an increased rate of anaerobic glycolysis when compared to healthy cells, which are not acidic.[15,16] The reason for this selective phenomenon is clear when one looks at the dependence of pH upon the fraction of Zn^{2+} ions existing as the aqueous ion
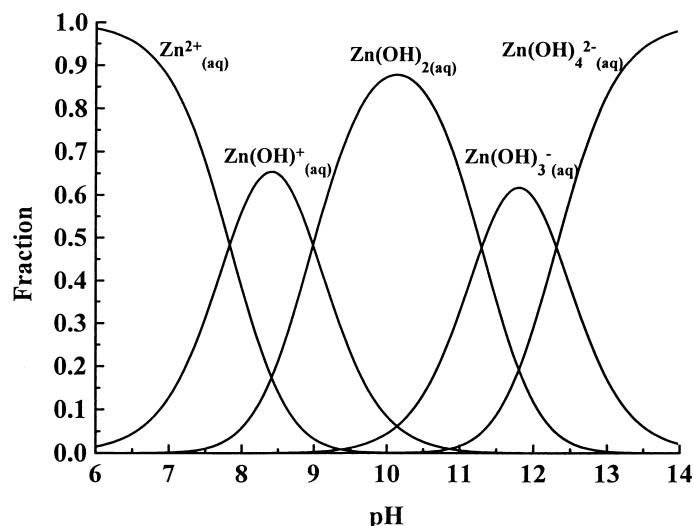
Figure 4.1: Fraction of Zn (II) ions species existing as Zn^{2+}(aq), $Zn(OH)^+$(aq), $Zn(OH)_2$(aq), $Zn(OH)^-_3$(aq) and $Zn(OH)^{2-}_4$(aq) over a range of pH at 25°C. Figure reproduced from Degen *et al.*[19]

in solution (Figure 4.1). It can be seen that ZnO largely exists as aqueous Zn^{2+} ions in weakly acidic to weakly basic environments. It has also been demonstrated ZnO QDs exhibit significant cytotoxic effects only after dissolution, preferentially killing cancer cells.[17,18] This lends further credence to this mechanism of action. This pathway has been proposed as a method to deliver a synergistic therapy whereby a therapeutic drug is encapsulated in a ZnO matrix and only selectively released in the acidic medium of a tumour by the dissolution of the ZnO. Thus there is a dual effect of the cytotoxicity of the Zn^{2+} ions and the therapeutic action of the drug.[13,14]

ZnO is also an interesting material due to it's luminescent properties, with the luminescence being dependent on the band gap energy which can be tuned by changing the size of the ZnO NP.[20–23] A model for determining the dependence of the band gap of ZnO with size has been derived from analysis of the electronic structure of bulk ZnO obtained from the full potential linearised augmented plane wave method using fatbands, density of states and partial density of states has been presented by the equation from Viswanatha *et al*:[20]

$$E = E_g + 100(72.4r^2 + 82.8r - 0.8)^{-1}$$
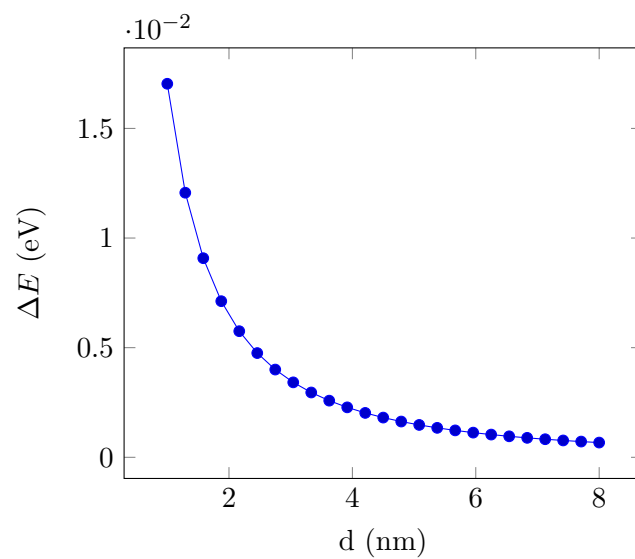
Figure 4.2: Change in band gap energy as a function of ZnO size using equation from Visawantha *et al.*[20]

Thus ZnO nanomaterial are very attractive due to their unique properties outlined above, making them suitable candidates for both chiroptical and biomedical applications. The main goal of this part of the project is to develop new chiroptically-active ZnO nanostructures and investigate their properties using various instrumental techniques.

4.2 Results and Discussion

Chiroptically-active ZnO NPs have been prepared using a sol-gel synthetic route. Similar syntheses of non-chiral ZnO NPs have been reported in the literature enabling one to obtain a ZnO QDs of varying sizes and wavelengths of photoluminescence.[22,23] The chiral component for this synthesis was chosen to be various amino acids with a long carbon chains to enable solvation in the ethanol used in the the previously reported syntheses. Modified amino acids have previously been used widely to successfully prepare various chiral luminescent quantum dots.[24–28] A variety of amino acid derivatives consisting of an amino acid functionalised with an 18-C chain at the N-position were first synthesised. The synthetic protocols to prepare these various derivatives is shown in Scheme 4.1. A DCC-coupling was chosen to synthesise the N-stearoyl-alanine derivative[29]. However, this synthetic protocol was unsatisfactory for the synthesis of the N-stearoyl-cysteine derivative. This is because the DCC-coupling may also proceed at the S-position, giving a mixture of products and thus poor yields. A benzotriazole-mediated synthesis was instead chosen as this reaction proceeds solely at the N- and not the S-position and gave the desired product in high yields.[30,31] To synthesise the N-stearoyl-glutamic acid derivative, the methyl ester protected glutamate was reacted with in basic conditions with stearoyl chloride.[32] Subsequent deprotection gave N-stearoyl-glutamic acid in high yields. With the N-stearoyl amino acid derivatives synthesised, N-stearoyl glutamic acid was used for the production of chiroptically-active ZnO NPs. The synthesis of ZnO NPs proceeded through the Zinc glutamate complex as shown in Scheme 4.2. This was refluxed in EtOH together with one equivalent of $LiOH.H_2O$ to form the ZnO NPs.

The obtained ZnO NPs exhibited a broad blue photoluminescence with an excitonic peak located at $\approx$ 305 nm in the UV-vis spectrum, indicating the presence of quantum confined ZnO NPs (Figure 4.3). The PL is a broad, defect type luminescence which is typical for ZnO, although there is no consensus on the origin of these emission bands at the current time.[22,33,34] The CD-spectra of the N-stearoyl-glutamic acid functionalised ZnO QDs indicate that they are chiroptically-active, Figure 4.4
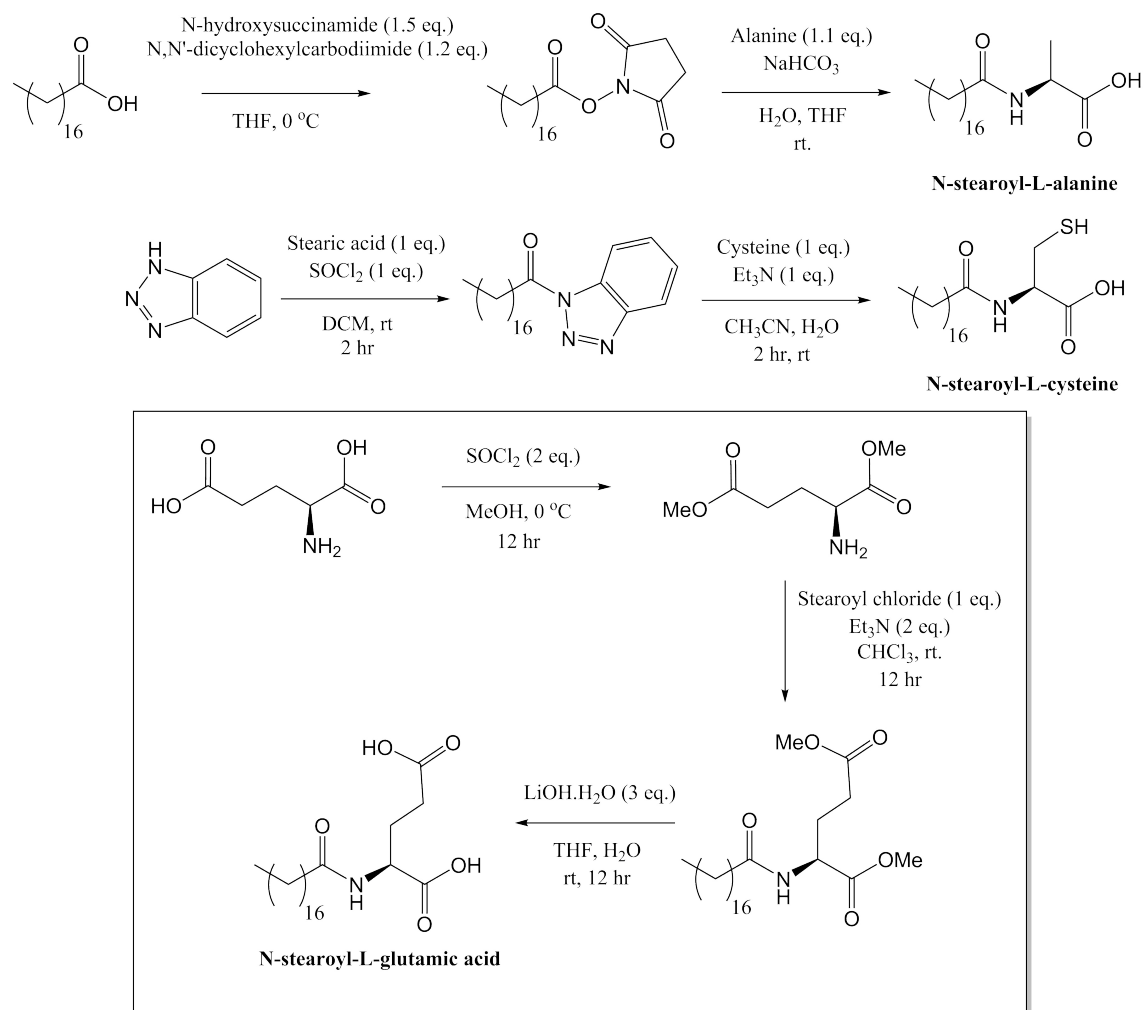
Scheme 4.1: Synthetic protocol for the production of N-stearoyl amino acid ligands
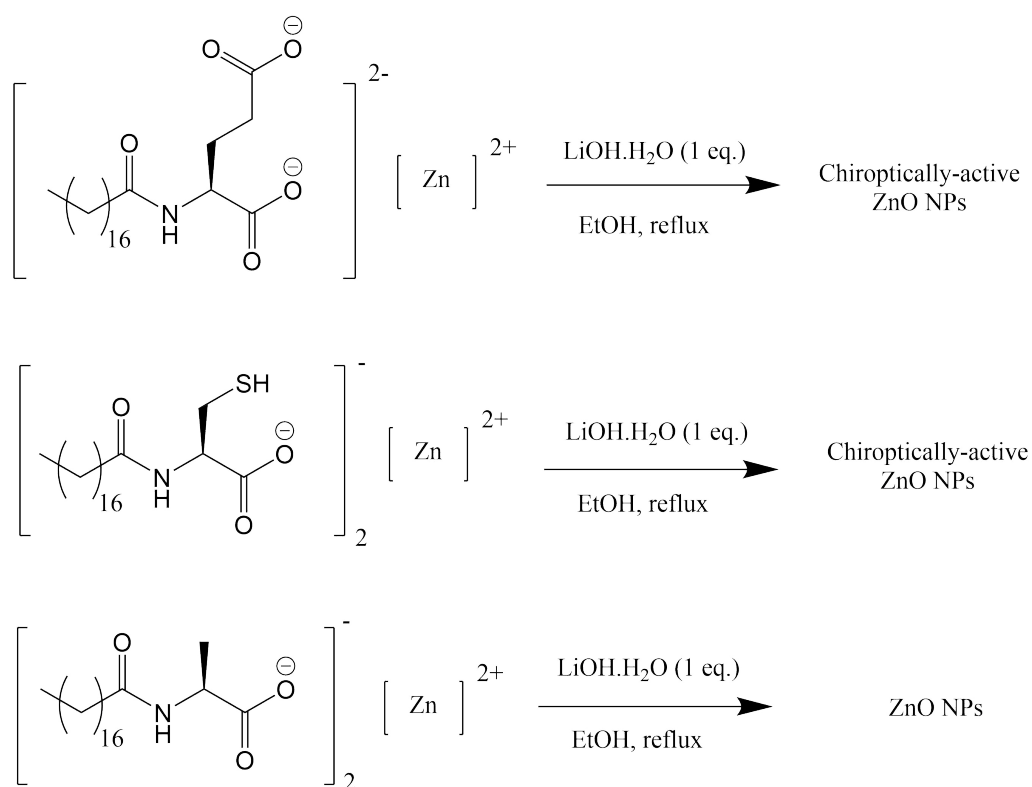
Scheme 4.2: Synthetic protocol for the production of N-stearoyl-amino acid functionalised ZnO nanoparticles
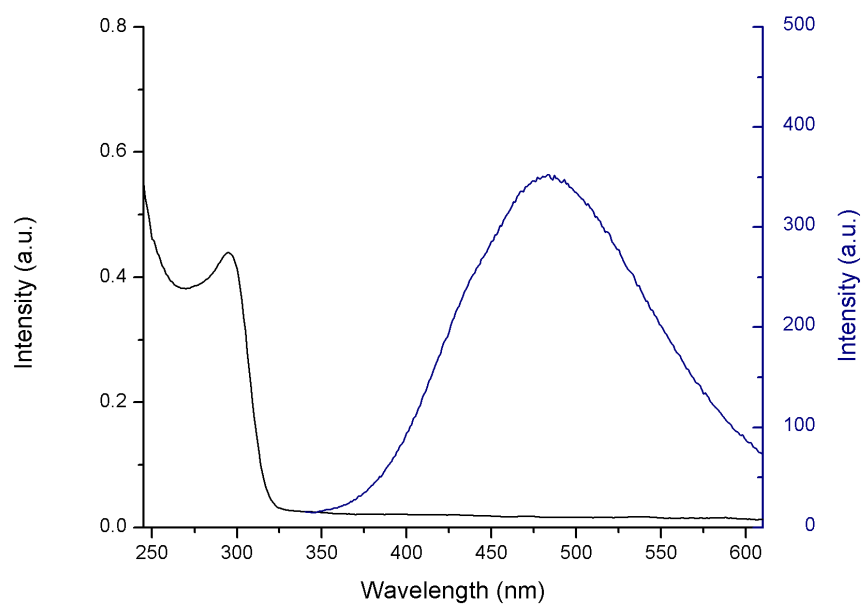
Figure 4.3: Photoluminescence (blue) and UV-vis (black) spectrum of ZnO particles 24 hrs after reaction
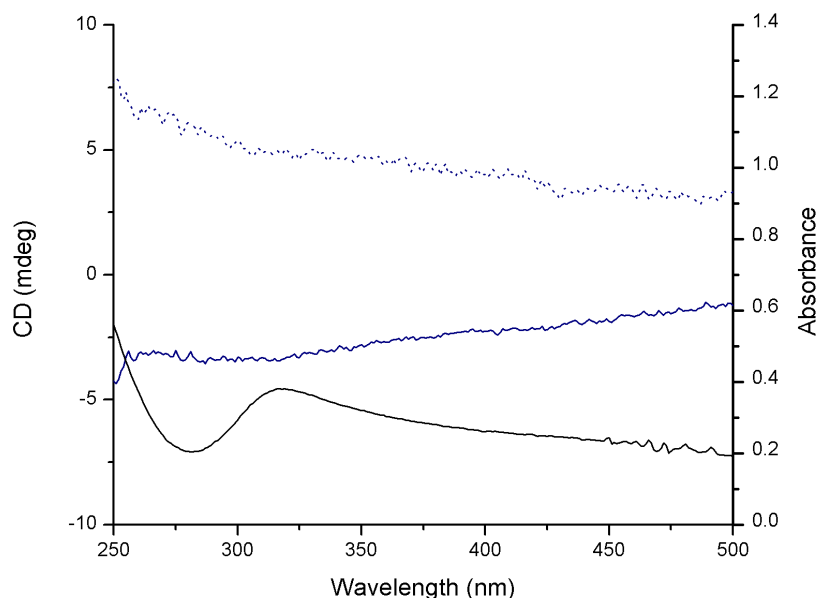
Figure 4.4: CD (blue) and absorption (black) spectra of D- (dotted) and L- (solid) N-stearoyl zinc glutamic acid ZnO

shows that the ZnO QDs exhibit the expected mirror image spectra for left- and right-handed enantiomers. The shape of the CD and UV-vis spectral lines are quite distinct from the CD and UV-vis of the starting Zn glutamate complexes which can be seen in Figure 4.5. This confirms the formation of a new chiroptically-active material when compared to the CD spectrum of the starting Zn glutamate complex (Figure 4.5).

ZnO NPs were also synthesised using N-stearoyl-L-alanine and N-stearoyl-L-cysteine as stabilising ligands (Scheme 4.2) The CD spectra of the ZnO NPs indicate that they are chiroptically-active in the band edge region of ZnO for the N-stearoyl-L-cysteine functionalised ZnO NPs (Figure 4.6) but not in the case of the N-stearoyl-L-alanine functionalised ZnO NPs (Figure 4.7). An explanation for the lack of induced CD in the N-stearoyl-L-alanine functionalised ZnO NPs is that the chiral centre in the alanine ligand consists of a single methyl group which does not directly interact with the ZnO surface. For a semiconductor NP to exhibit chiroptical activity due to the presence of a chiral ligand, the HOMOs of the semiconductor NP must overlap with the asymmetric orbitals of a chiral ligand.[35] In the case of N-stearoyl-L-alanine,
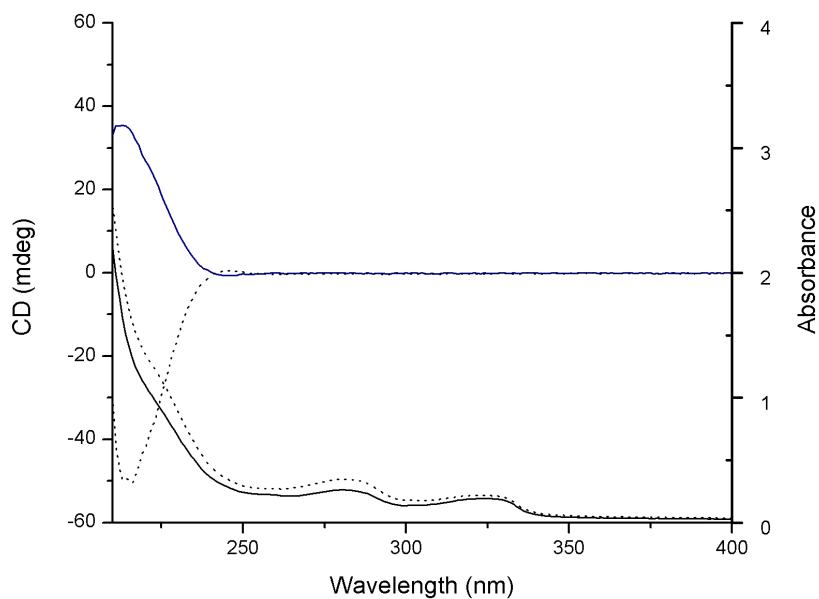
Figure 4.5: CD (blue) and absorption (black) spectra of D- (dotted) and L- (solid) N-stearoyl zinc glutamate complexes

there is only one binding site (the carboxylic acid group), around which the entire molecule may rotate leaving no asymmetric orientation of the ligand orbitals. There are two possible binding sites in the case of N-stearoyl-L-cysteine (a thiol and a carboxylic acid) and N-stearoyl-glutamic acid (two carboxylic acids). These two binding groups interact with the ZnO surface, locking in "conformational rigidity" and the asymmetry of the ligand orbitals, which is a requirement for induced circular dichroism.[36]

The XRD patterns of the N-stearoyl-amino acid functionalised ZnO NPs indicate that they are of the zincite phase (Figure 4.8). The TEM images of the N-stearoyl-amino acid functionalised ZnO NPs are shown in Figure 4.9. The images indicate that the obtained NPs are crystalline in nature and have a size ranging between 3-4 nm.

It is interesting to note that only the N-stearoyl-glutamic acid functionalised ZnO NPs exhibited photoluminescence. This may be attributed to experimental variation or to the influences of the different surface modifications upon the luminescence
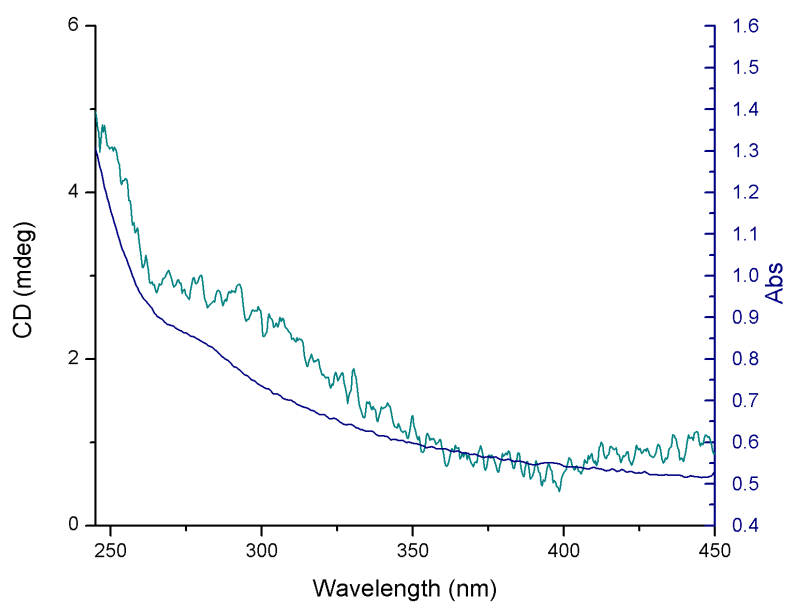
Figure 4.6: CD (green) and absorption (blue)spectra of N-stearoyl-L-cysteine ZnO NPs
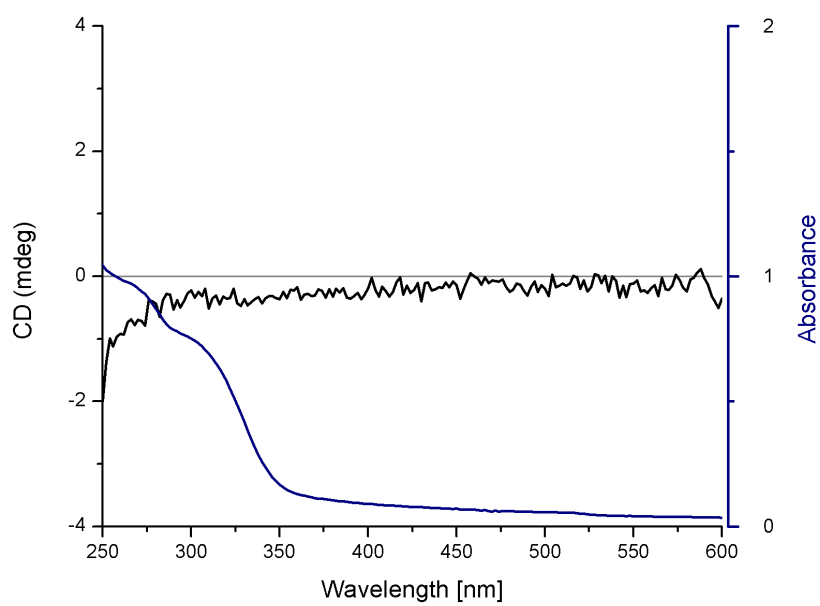
Figure 4.7: CD (black) and absorption (blue) spectra of N-stearoyl-L-alanine ZnO NPs
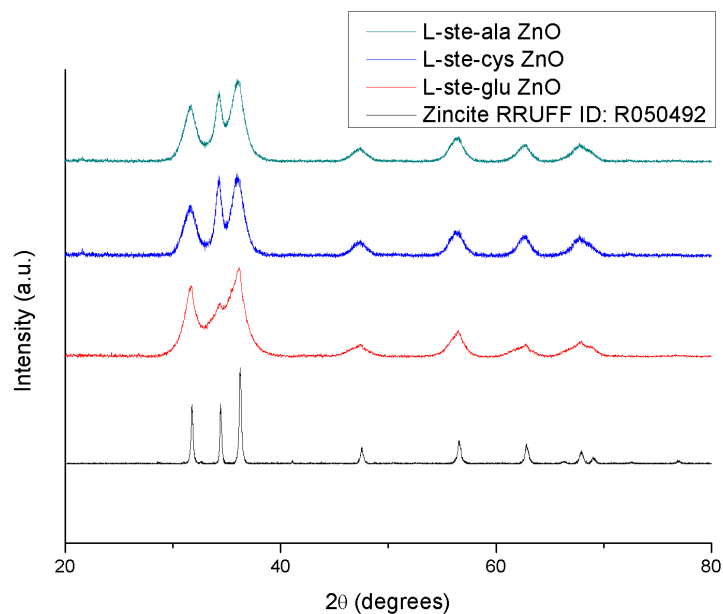
Figure 4.8: XRD patterns of N-stearoyl-amino acid functionalised ZnO NPs

of the ZnO.[37] In either case, further study of this phenomenon is needed to fully understand this behaviour.

4.3 Conclusions

This work has demonstrated the possibility of the development of chiroptically-active and luminescent ZnO NPs. We believe that chiroptical activity of the ZnO NPs is dependent on the binding behaviour of the chiral ligand. These aspects require further studies, computer modelling and are to be explored in the future. Also, it will be important to investigate biological behaviour of chiroptically-active and luminescent ZnO NPs in vitro for potential biosensing and bioimaging applicaitons. This will be the subject of our future work.
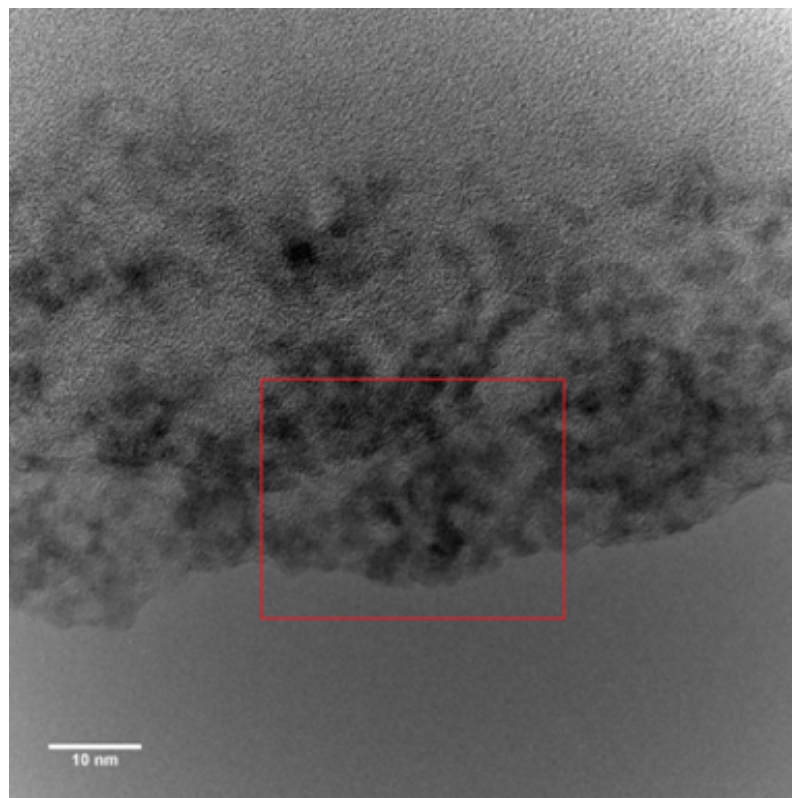
(a) TEM image of N-stearoyl-L-glutamic acid functionalised ZnO NPs
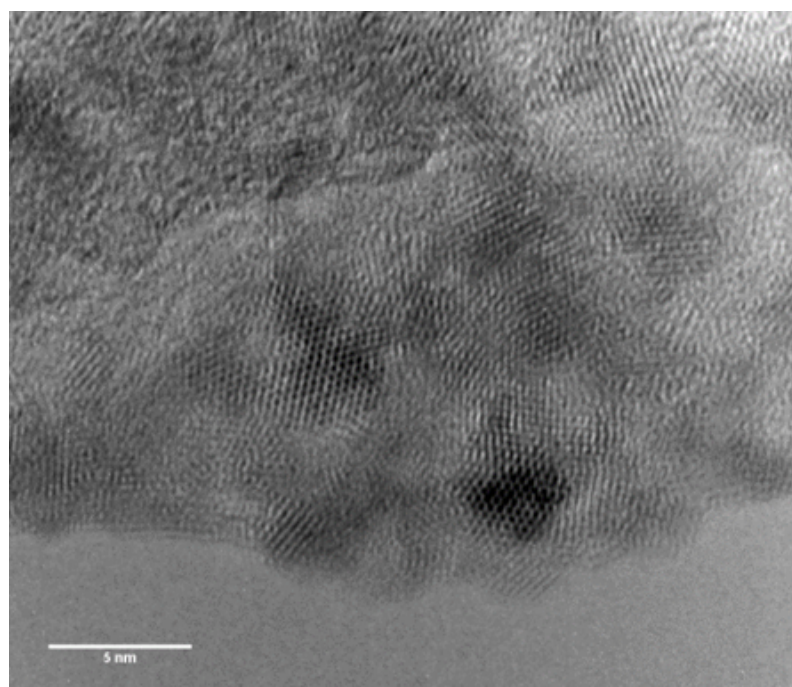
(b) TEM image of area inside red rectangle above

Figure 4.9: TEM image of N-stearoyl-L-glutamic acid functionalised ZnO NPs
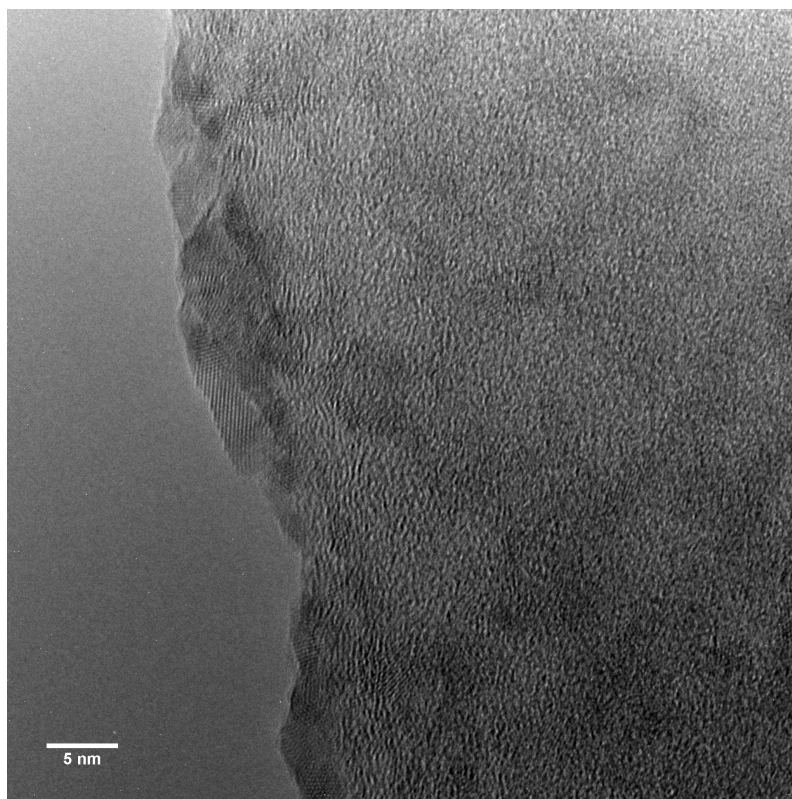
(c) TEM image of N-stearoyl-L-cysteine functionalised ZnO NPs
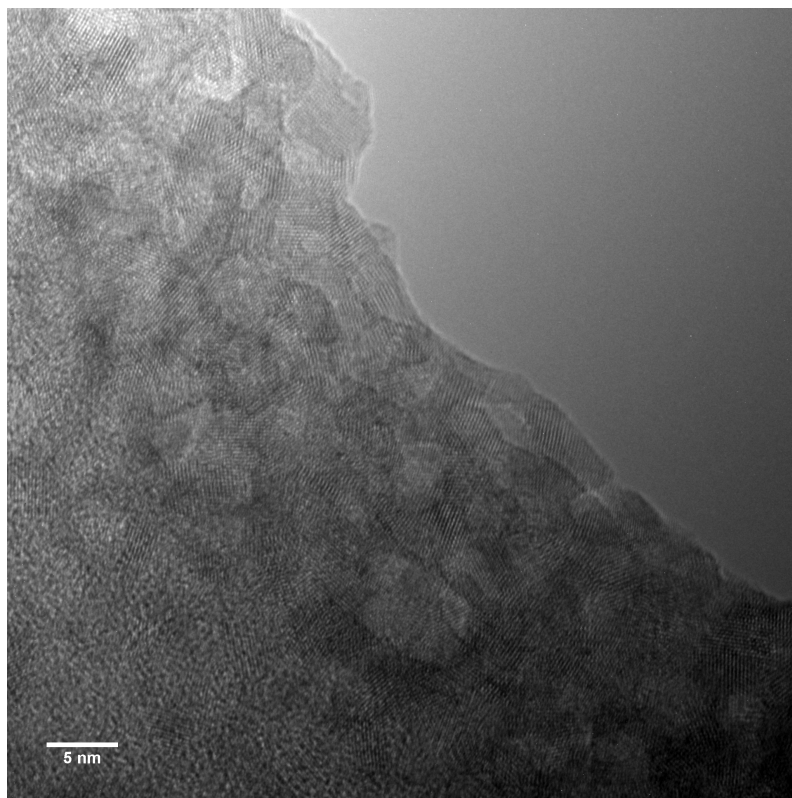
(d) TEM image of N-stearoyl-L-alanine functionalised ZnO NPs

References

(1) Ma, J. Z.; Hui, A. P.; Liu, J. L. Research progress on antibacterial materials of nano-ZnO., 2014.

(2) Sun, X. W.; Yang, Y., *Zno nanostructures and their applications*, 2012.

(3) Manaia, E. B.; Kaminski, R. C. K.; Caetano, B. L.; Briois, V.; Chiavacci, L. A.; Bourgaux, C. *European Journal of Nanomedicine* **2015**, DOI: `10.1515/ejnm-2014-0047`.

(4) Zhang, Y; Nayak, T.; Hong, H; Cai, W *Current Molecular Medicine* **2013**, DOI: `10.2174/1566524013666131111130058`.

(5) Mirzaei, H.; Darroudi, M. *Ceramics International* **2016**, DOI: `10.1016/j.ceramint.2016.10.051`.

(6) Bogdan, J.; Pławińska-Czarnak, J.; Zarzyńska, J. *Nanoscale Research Letters* **2017**, DOI: `10.1186/s11671-017-2007-y`.

(7) Ma, Y.-Y.; Ding, H.; Xiong, H.-M. *Nanotechnology* **2015**, DOI: `10.1088/0957-4484/26/30/305702`.

(8) Xiong, H.-M.; Xu, Y.; Ren, Q.-G.; Xia, Y.-Y. *Journal of the American Chemical Society* **2008**, *130*, 7522–7523.

(9) Wilhelmi, V.; Fischer, U.; Weighardt, H.; Schulze-Osthoff, K.; Nickel, C.; Stahlmecke, B.; Kuhlbusch, T. A. J.; Scherbart, A. M.; Esser, C.; Schins, R. P. F.; Albrecht, C. *PLoS ONE* **2013**, DOI: `10.1371/journal.pone.0065704`.

(10) Akhtar, M. J.; Ahamed, M.; Kumar, S.; Majeed Khan, M. A.; Ahmad, J.; Alrokayan, S. A. *International Journal of Nanomedicine* **2012**, DOI: `10.2147/IJN.S29129`.

(11)   Gao, F.; Ma, N.; Zhou, H.; Wang, Q.; Zhang, H.; Wang, P.; Hou, H.; Wen, H.; Li, L. *International journal of nanomedicine* **2016**, DOI: `10.2147/IJN.S107021`.

(12)   Zhang, J.; Qin, X.; Wang, B.; Xu, G.; Qin, Z.; Wang, J.; Wu, L.; Ju, X.; Bose, D. D.; Qiu, F.; Zhou, H.; Zou, Z. *Cell Death and Disease* **2017**, DOI: `10.1038/cddis.2017.337`.

(13)   Cai, X.; Luo, Y.; Zhang, W.; Du, D.; Lin, Y. *ACS Applied Materials and Interfaces* **2016**, DOI: `10.1021/acsami.6b04933`.

(14)   Rasmussen, J. W.; Martinez, E.; Louka, P.; Wingett, D. G. *Expert opinion on drug delivery* **2010**, DOI: `10.1517/17425247.2010.502560`.

(15)   Kato, Y.; Ozawa, S.; Miyamoto, C.; Maehata, Y.; Suzuki, A.; Maeda, T.; Baba, Y. *Cancer Cell International* **2013**, DOI: `10.1186/1475-2867-13-89`.

(16)   Swietach, P.; Vaughan-Jones, R. D.; Harris, A. L.; Hulikova, A. *Philosophical Transactions of the Royal Society B: Biological Sciences* **2014**, DOI: `10.1098/rstb.2013.0099`.

(17)   Xia, T.; Kovochich, M.; Liong, M.; Zink, J. I.; Nel, A. E. *ACS Nano* **2008**, DOI: `10.1021/nn700256c`.

(18)   Nel, A. E.; Mädler, L.; Velegol, D.; Xia, T.; Hoek, E. M. V.; Somasundaran, P.; Klaessig, F.; Castranova, V.; Thompson, M. *Nature Materials* **2009**, DOI: `10.1038/nmat2442`.

(19)   Degen, A.; Kosec, M. *Journal of the European Ceramic Society* **2000**, DOI: `10.1016/S0955-2219(99)00203-4`.

(20)   Viswanatha, R.; Sapra, S.; Satpati, B; Satyam, P. V.; Dev, B. N.; Sarma, D. D. *Journal of Materials Chemistry* **2004**, DOI: `10.1039/b310404d`.

(21)   Zhao, D.; Song, H.; Hao, L.; Liu, X.; Zhang, L.; Lv, Y. *Talanta* **2013**, *107*, 133–139.

(22)   Zhang, L.; Yin, L.; Wang, C.; lun, N.; Qi, Y.; Xiang, D. *The Journal of Physical Chemistry C* **2010**, *114*, 9651–9658.

(23)   Zhang, L.; Yin, L.; Wang, C.; Lun, N.; Qi, Y. *ACS Applied Materials & Interfaces* **2010**, *2*, 1769–1773.

(24)   Moloney, M. P.; Govan, J.; Loudon, A.; Mukhina, M.; Gun'ko, Y. K. *Nat. Protocols* **2015**, *10*, 558–573.

(25)   Tohgha, U.; Varga, K.; Balaz, M. *Chemical Communications* **2013**, *49*, 1844–1846.

(26)   Govan, J. E.; Jan, E.; Querejeta, A.; Kotov, N. A.; Gun'ko, Y. K. *Chemical Communications* **2010**, DOI: `10.1039/c0cc00930j`.

(27)   Nakashima, T.; Kobayashi, Y.; Kawai, T. *Journal of the American Chemical Society* **2009**, DOI: `10.1021/ja902800f`.

(28)   Gun'ko, Y.; Kelly, J.; Moloney, M. *CHEMICAL COMMUNICATIONS* **2007**, DOI: `10.1039/b704636g`.

(29)   Sivasamy, A.; Krishnaveni, M.; Rao, P. G. *Journal of the American Oil Chemists' Society* **2001**, DOI: `10.1007/s11746-001-0361-5`.

(30)   Katritzky, A. R.; Tala, S. R.; Abo-Dya, N. E.; Gyanda, K.; El-Gendy, B. E.-D. M.; Abdel-Samii, Z. K.; Steel, P. J. *The Journal of Organic Chemistry* **2009**, *74*, 7165–7167.

(31)   Katritzky, A. R.; Zhang, Y.; Singh, S. K. *Synthesis* **2003**, *2003*, 2795–2798.

(32)   Yao, L. Y.; Lin, Q.; Niu, Y. Y.; Deng, K. M.; Zhang, J. H.; Lu, Y. *Molecules* **2009**, DOI: `10.3390/molecules14104051`.

(33)   Fu, Y.-S.; Du, X.-W.; Kulinich, S. A.; Qiu, J.-S.; Qin, W.-J.; Li, R.; Sun, J.; Liu, J. *Journal of the American Chemical Society* **2007**, *129*, 16029–16033.

(34)   Willander, M.; Nur, O.; Sadaf, J. R.; Qadir, M. I.; Zaman, S.; Zainelabdin, A.; Bano, N.; Hussain, I. *Materials* **2010**, DOI: `10.3390/ma3042643`.

(35)   Tohgha, U.; Deol, K. K.; Porter, A. G.; Bartko, S. G.; Choi, J. K.; Leonard, B. M.; Varga, K.; Kubelka, J.; Muller, G.; Balaz, M. *ACS Nano* **2013**, *7*, 11094–11102.

(36)   Allenmark, S. *Chirality* **2003**, *15*, 409–422.

(37)   Norberg, N. S.; Gamelin, D. R. *Journal of Physical Chemistry B* **2005**, DOI: `10.1021/jp0535285`.

Chapter 5

CeO$_2$ Nanoparticles for Ligand-Assisted Catalysis Applications

5.1 Introduction

5.1.1 Ligand-accelerated catalysis

Ligand-accelerated catalysis was first proposed by K. Barry Sharpless[1], with the theory stemming from his work on asymmetric oxidations, for which he shared the Nobel prize in 2001. In ligand-accelerated oxidation the presence of a ligand increases the rate of a catalytic process, a representation of this process can be seen in Figure 5.1

Figure 5.1: Ligand accelerated catalysis

Ligand-accelerated catalysis is defined as taking place when:

$$\frac{v_{C/L}}{v_C} > 1$$

$$ee = 1 - \frac{2}{LAE + 1} * 100$$
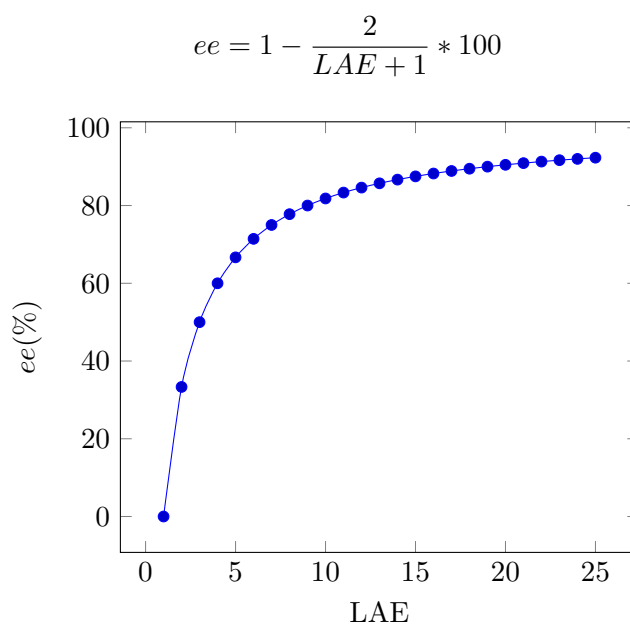
Figure 5.2: LAE vs enantiomeric excess %. The blue dots represent integer values of the LAE parameter from 1 to 25.

Where 'C' and 'L' refer to 'Catalyst' and 'Ligand' respectively. A further parameter can be derived, which is known as the Ligand-acceleration effect (LAE). This is given by:

$$LAE = \frac{k_1 K_{eq}[ligand]}{k_o}$$

$K_{eq}[ligand]$ in the above equation refers to the catalyst/ligand binding constant. If the accelerating ligand also affects the stereochemical outcome of the reaction, then it is possible to produce products of a desired enantiomer. This is the essence of using chiral ligands to generate asymmetric catalysts. High levels of enantioselectivity (ee > 90 %) can be achieved when LAE > 20. An idealised representation of this process is shown in Figure 5.2.

5.1.2 Aims: CeO$_2$ base catalyst by ligand self assembly

It is possible to prepare a basic heterogeneous catalyst by mixing a metal oxide with an appropriate ligand. This method was proposed by Tamura *et al.* and involves mixing CeO2$_2$ nanoparticles with pyridine based ligands with two adjacent Lewis-basic sites[2]. The CeO$_2$ surface is composed of adjacent Lewis acidic (Cerium)

and Lewis basic (Oxygen) sites. When mixed with pyridine derivatives such as 2-cyanopyridine, which has a Lewis basic cyano-group at the -2 position, a catalytic site appropriate for base catalysed reactions is formed. This may be theorised to be due to the formation of a Lewis-adduct between the pyridine nitrogen and Cerium atoms on the surface of the nanoparticles. This in turn pushes the cyano-group and oxygen atoms on the CeO_2 surface into close proximity, generating the active base site as seen in Figure 5.3. The resulting catalytic material was seen to exhibit a dramatic activity rate enhancement for hydromethoxylation of acrylonitrile. The reaction rate was increased $> 2,000$-fold compared with only CeO2 or 2-cyanopyridine.[2]
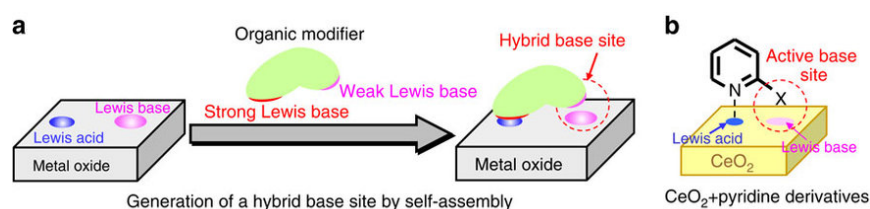
Figure 5.3: Generation of a hybrid base site by self assembly. Figure reproduced from Tamura *et al.*[2].

This catalytic system thus appears to be an ideal candidate to which one can apply the principles of Ligand-accelerated catalysis. If it is possible to design a ligand which can stereochemically alter the binding around the active base site, then a rate increase of $> 2,000$-fold would result in a similarly large LAE. Extrapolating from Figure 5.2, this would theoretically result in % ee's of 100%. Therefore the aim for this part of our work was to develop a new CeO_2 NP-based system for ligand accelerated catalysis. The chiral ligand that was selected as a initial candidate for this purpose was a PyBox-type ligand based on the structure of 2-cyanopyridine. The ligand has an oxazoline ring in place of the cyano-group. This oxazoline ring has a chiral centre at the 2-position beside the Lewis basic nitrogen atom. This was chosen to introduce steric hindrance on one side of the active base site as shown in Figure 5.4.
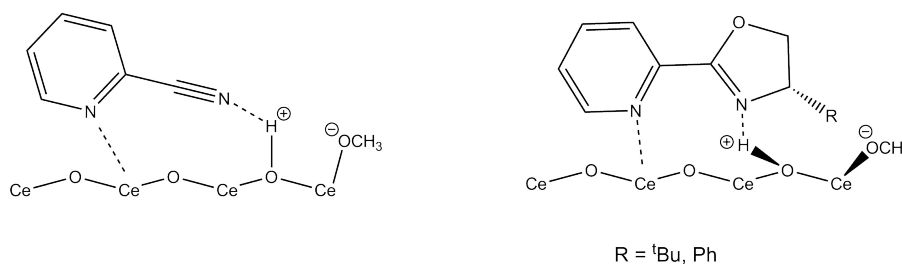
Figure 5.4: Formation of active base site with 2-cyanopyridine and chiral oxazoline-base ligand

5.2 Results and Discussion

CeO_2 nanopowder was obtained from Nanostructured and Amorphous Materials Inc. The size distribution was described as 20 to 30 nm in size at 99.5 % purity. The X-Ray diffraction pattern obtained (Figure 5.5) identifies the sample as matching the cubic fluorite structure of CeO_2. SEM imaging (Figure 5.6) confirmed that the sample was made up of NPs in the expected size range.
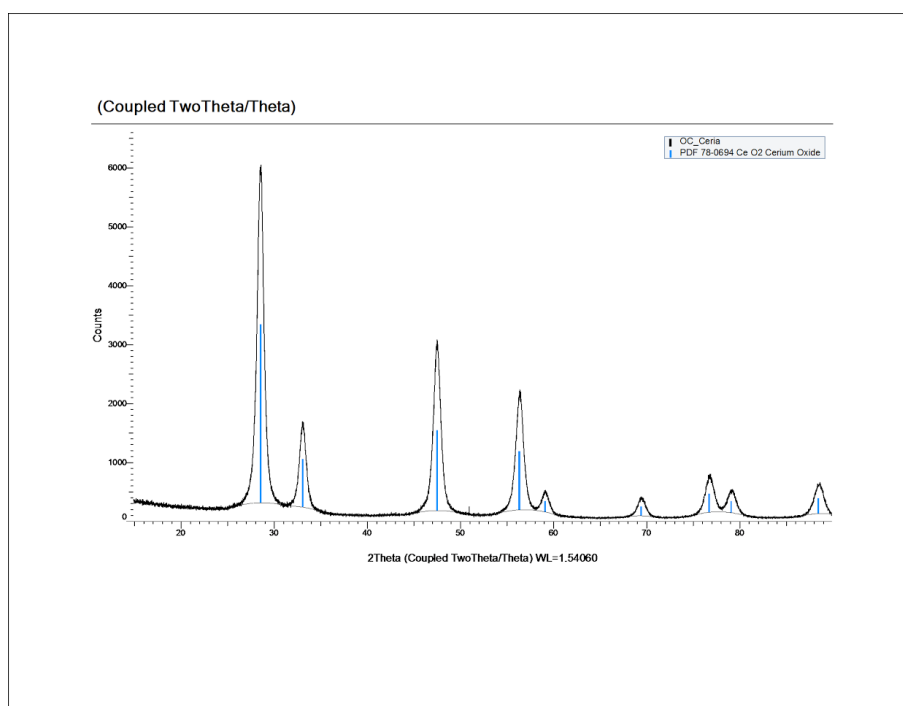
Figure 5.5: XRD pattern of CeO_2 NPs
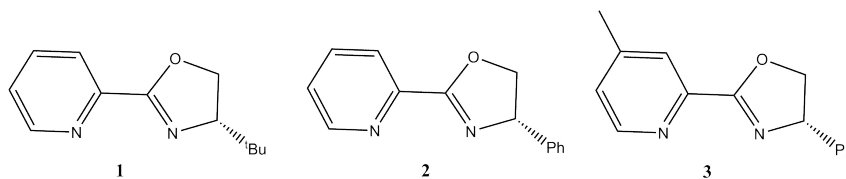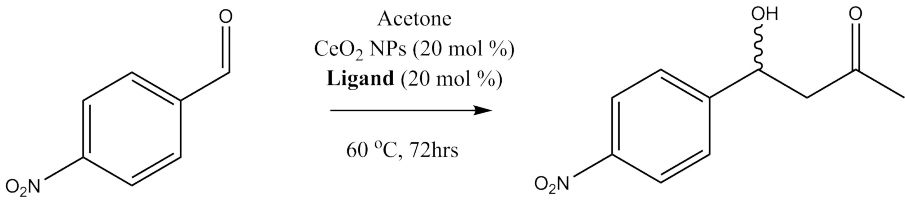
Figure 5.7: PyBox-based ligands for inital catalytic investigations
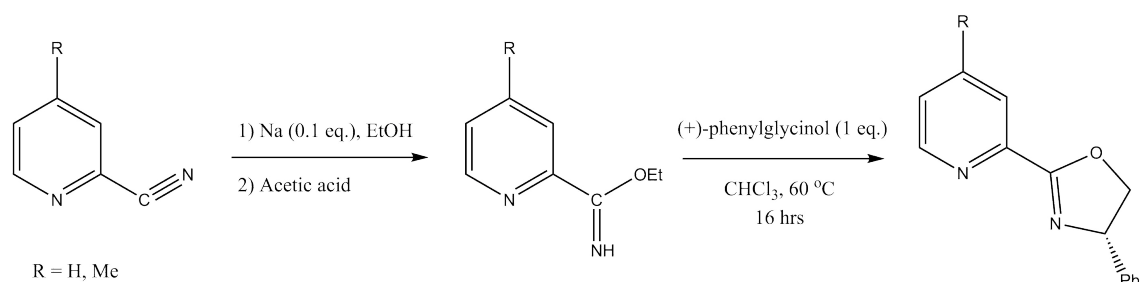
Scheme 5.1: Synthetic scheme for the preparation of PyBox ligands
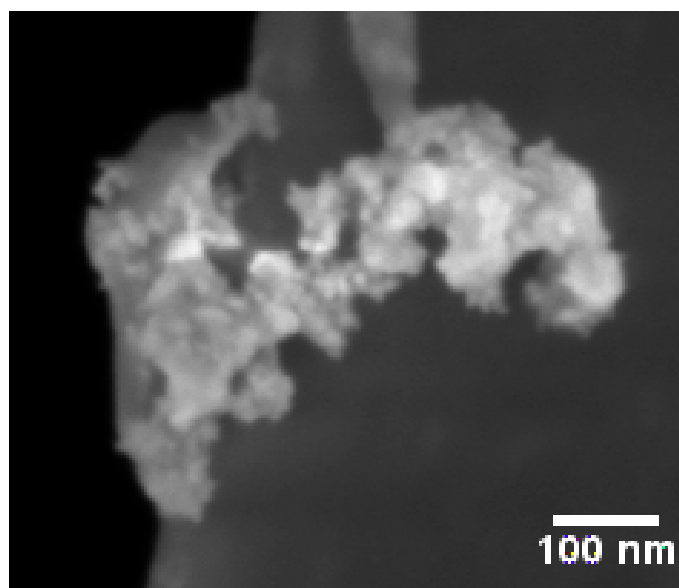
Figure 5.6: SEM image of CeO$_2$ NPs

A series of PyBox based ligands were chosen for the initial investigations. The structures of these ligands can be seen in Figure 5.7. Ligand **1** is commercially available whereas ligands **2-3** had to be prepared as can be seen in Scheme 5.1. Ligands **2-3** differ with respect to the 4-position on the pyridine ring. The -methyl substituents present on ligand **3** and was chosen with the objective of increasing the electron density present at the pyridine nitrogen, thus increasing it's Lewis basicity.
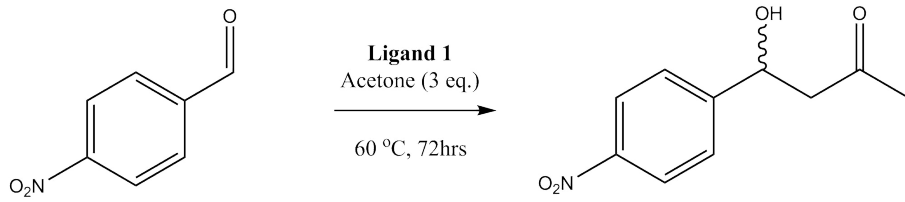
Ligand	Yield (%)	% ee
1	16	< 5
1 control (no CeO$_2$)	0	-
2	20	< 5
1 control (no CeO$_2$)	0	-
3	20	< 5
3 control (no CeO$_2$)	0	-
CeO$_2$ control (no ligand)	0	-

Table 5.1: Initial investigations of aldol reaction between acetone and 4-nitrobenzaldehyde

An aldol reaction between acetone and 4-nitrobenzaldehyde was chosen as a suitable test reaction. This was carried out using ligands **1-4** with commercially available CeO$_2$ nanoparticles. The results of these reactions are summarised in Table 5.1

One of the most striking results is that the self-assembled catalyst is managing to drive the formation of the aldol product. The base-catalysed aldol reaction begins with the deprotonation of acetone. Acetone has a pK$_a$ of 26.5[3], whereas the nitrogen atoms in the ligand have an estimated pK$_a$ between 5-7. The self-assembled base catalyst must have a pK$_a$ > 19.2 in order to deprotonate acetone. This is a large increase in basicity and indicates that the self-assembled catalyst is forming a basic active-site in a similar manner to that described by Tamura *et al.*[2]. The products of the aldol reaction are racemic, indicating that the ligand is not exerting stereochemical control over the catalytic site. The effects of differing the solvent was also investigated. Changing the solvent may have drastic effects upon both the yield and enantioselectivities of asymmetric transformations.[4,5] The results shown in Table 5.2 show that there is an effect upon the yield in the case of CHCl$_3$ but otherwise no effect upon the enantioselectivity of the reaction in any of the solvents investigated.

Table 5.2: Effect of solvent on aldol reaction between acetone and 4-nitrobenzaldehyde

Solvent	Yield (%)	% ee
THF	18	< 5
CHCl$_3$	8	< 5
Toluene	21	< 5
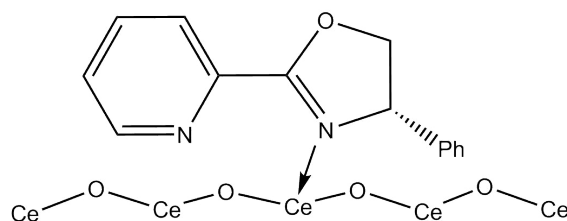
Figure 5.8: Suggested PyBox ligand orientation on CeO$_2$ surface

An explanation for the lack of enantioselective control in the aldol reaction may be due to a mismatch in basicity between the nitrogens of the pyridine and oxazoline rings present in the PyBox catalyst. Higher Lewis-basicity of the oxazoline ring would result in the oxazoline-nitrogen preferentially forming a Lewis-adduct with the Cerium atoms present on the surface of CeO$_2$. This would result in the active base site being formed between the pyridine-nitrogen and the oxygen atoms on the CeO$_2$ surface as shown in Figure 5.8. The stereochemical control provided by the bulky phenyl group would be lost in this scenario as it is far from the catalytic site.

Evidence for the mismatch in basicity comes from the results of initial investigation upon the suitability of the catalyst for a base-catalysed Michael addition. The results of these investigations are shown in Table 5.3. Dimethyl malonate has a pK$_a$ of 15.9 and Meldrum's acid has a pK$_a$ of 7.3.[6] It can be seen that **2** is not able to deprotonate dimethyl malonate whereas it is able to deprotonate Meldrum's acid, which is the first step of the base-catalysed Michael addition. Pyridine has a pK$_a$ of 5.14,[7] therefore we are able to infer that the oxazoline ring of the PyBox ligand

Michael Donor	Yield (%)	% ee
Dimethyl malonate	8	0
Control (no CeO_2)	0	-
Meldrum's acid	17	0
Control (no CeO_2)	15	0

Table 5.3: Initial investigations of Michael Reaction

has a $pK_a > 7.3$, which is required to successfully catalyse this Michael addition. It was also found that the products of the Michael reaction were racemic, with no enantioselective effect being observed.

5.3   Conclusions

Thus we have performed the initial development and testing of the new CeO_2 based system for ligand accelerated catalysis. It has been demonstrated that it is possible to catalyse both aldol and Michael reactions by ligand self assembly on the surface of CeO_2 NPs. The products of these reactions are racemic however, and this is most likely due to a mismatch in pK_a of the nitrogen atoms in the chiral PyBox ligands. This has been inferred through the use of Michael donors of differing pK_a. Therefore, future work is necessary to further develop and optimise this catalytic system.

References

(1) Berrisford, D. J.; Bolm, C.; Sharpless, K. B. *Angewandte Chemie International Edition in English* **1995**, *34*, 1059–1070.

(2) Tamura, M.; Kishi, R.; Nakagawa, Y.; Tomishige, K. *Nat Commun* **2015**, *6*, DOI: `10.1038/ncomms9580`.

(3) Bordwell, F. G. *Accounts of Chemical Research* **1988**, *21*, 456–463.

(4) Reichardt, C.; Welton, T., *Solvents and Solvent Effects in Organic Chemistry*, 2004.

(5) Dyson, P. J.; Jessop, P. G. *Catal. Sci. Technol.* **2016**, DOI: `10.1039/C5CY02197A`.

(6) Arnett, E. M.; Maroldo, S. G.; Schilling, S. L.; Harrelson, J. A. *Journal of the American Chemical Society* **1984**, *106*, 6759–6767.

(7) *Determination of organic structures by physical methods / editors, E.A. Braude, F.C. Nachod*; Nachod, F. C.F. C., Braude 1922, E. A.E. A., Eds.; Academic Press: New York, 1955.

Chapter 6

Experimental

6.1 Materials

6.1.1 Starting chemicals and solvents

All starting materials were purchased from Sigma Aldrich and Acros Organics. The Millipore water was obtained using a MilliQ system pure to $18\,\mathrm{M\Omega}$. All solvents were obtained from the Trinity College Dublin hazardous materials solvent stores.

6.1.2 Equipment

Hydrothermal reaction vessels and 23 mL PTFE-liners were purchased from the Parr Instrument Company. The furnace used was a Barnstead Thermolyne 1400 Furnace.

6.2 Instrumentation

6.2.1 CD spectroscopy

Circular dichroism is defined as the difference in absorption between left and right-handed circularly polarised light:

$$CD = A^l - A^r$$

Where Al and Ar are the absorptions of left- and right-handed circularly polarised light at a given wavelength. Due to historical reasons, the output of CD spectrometers is often measured in ellipticity, θ (in mdeg). This is related to CD by $\theta(in\,mdeg) = 32,980\,CD$. By definition, circular dichroism can only be observed with regard to the absorption bands, and a characteristic rapid change in the sign of the CD-response can often be observed approaching the absorbance maximum. This is known as the cotton effect.[1] .

Kuhn's anisotropy factor or g-factor is a dimensionless quantity which can be defined thus:

$$g = \frac{A^l - A^r}{A}$$

where A is the absorbance of the sample at the given wavelength. The g-factor is independent of the concentration or the path length of the sample (this can be demonstrated using the Beer- Lambert law).

Performed using a Jasco J-815 CD spectrometer. The scans were preformed using a quartz cuvette of path length 10 mm, a scan rate of 100 nm per minute and a response time of 1 second.

6.2.2 Chiral HPLC

Chiral HPLC was preformed using an Acquity UPC^2 system. Chiral Stationary Phase used was an Acquity UPC^2 Trefoil CEL1 (2.5 μm) 3.0 x 150mm Column. Detection: UV 254 nm with PDA detector Mobile Phase: A $=$ CO$_2$, B $=$ Methanol/IPA (1:1, v:v)

Column Temperature: 30 °C Inlet Pressure: 1500 (psi)

6.2.3   Cyclic volatammetry

This was carries out using a Metrohm Autolab type III controlled using Autolab NOVA. A three electrode setup was used, utilising a titanium counter electrode, a saturated calomel reference electrode and the electrode to be tested as the working electrode.

6.2.4   Differential thermal analysis

Differential thermal analysis (DTA) is used to measure the flow of thermal energy into or out of a sample when heat energy is applied, with respect to a reference material. The sample is in a crucible, which rests on a thermocouple that can measure changes in temperature and thermal energy. This can give insight into thermal events such as crystallisation that may occur within a sample with rising temperature.

DTA was conducted on a Stanton Redcroft STA-1500 using a platinum crucible and alumina as a reference material.

6.2.5   Dynamic light scattering

Dynamic light scattering (DLS), is a technique used to measure the size of particles in the sub-micron range. It provides information about the average particle size in suspension and also measures the width of the particle distribution, called the polydispersity index (PDI). It utilises the Brownian motion of particulates undergoing diffusion in a liquid sample to provide a measurement of the hydrodynamic radius of the sample. In this way, it differs from electron microscopy, which shows the primary particle size of a sample which has been dried on a substrate. As such, average diameters according to DLS are often larger than those measured using electron microscopy.

Illumination of randomly moving particles in a liquid with a laser causes scattering of the light. This scattered intensity fluctuates as the particles move under Brownian

motion. Mathematical analysis of this fluctuation in the light intensity allows determination of an intensity distribution of the average hydrodynamic radius, which can be further manipulated mathematically to provide information about the volume distribution and the PDI. An important feature of nanoparticle suspensions is that small particles move more quickly than larger particles and this relationship is defined by the Stokes-Einstein equation:

$$D = \frac{kT}{6\pi R \eta}$$

T is the temperature, r is the radius and η is the solvent viscosity.

Dynamic light scattering measurements were performed using a Malvern Zetasizer Nanoseries V5.10.

6.2.6 ^{1}H NMR spectroscopy

Nuclear magnetic resonance spectroscopy is a powerful technique which is used to deliver detailed information about molecular structure and bonding. It is dependent on the magnetic properties of the nucleus. When a nucleus is placed in a magnetic field it may absorb energy (radiofrequency). The energy ($E = hv$) of the absorbed radiation is characteristic of the nucleus and its environment. Certain atomic nuclei possess spin angular momentum and this gives rise to difference spin states. The number of possible orientations is given by 2I + 1, where I is the spin quantum number and it is possible to have values of zero, half, and whole integers. Nuclei with $I = 0$ do not possess a magnetic moment and therefore do not demonstrate NMR signals; all other nuclei can. Nuclei, such as those with $I = \frac{1}{2}$ like ^{1}H, have two possible arrangements, either aligned "with" (α) or "against" (β) an applied magnetic field (B_0), generating two spin states. These are two different energy states and it is the transition between these that can be monitored and is the origin of the NMR effect. The difference between these two spin states is directly proportional to the magnitude of B_0. A slight excess of spins aligns with B_0 and this creates a net magnetisation in the sample (M_0). In a static magnetic field, these nuclei precess around the magnetic field at a frequency dependent on the strength of the magnetic

field, the Larmor frequency (ω_o):

$$\omega_o = \gamma B_0$$

Where γ is the magnetogyric ratio.

Since the external applied magnetic field is much greater than the sample's magneti-sation, M_0, the sample is difficult to detect. Therefore, a second magnetic field is applied perpendicular to the external field by applying a radiofrequency pulse (B_1) along the x-axis. This causes the magnetic moments to move to the x-axis, away from their equilibrium state. Upon the removal of B_1, the nuclei return to their previous equilibrium. $M_x y$ returns to M_0 in a spiralling motion while still rotating at ω_o. This is referred to as longitudinal relaxation and the time it takes is T_1. The motion of the magnetic moments generates a current in a receiver coil in the x-axis which is then used to construct a time domain NMR signal. A Fourier transform is then used to generate the typical frequency domain spectrum.

Spectra were recorded in deuterated solvents with a Bruker Advance DPX-400 MHz spectrometer at frequency 400.13 MHz for ^{1}H. The signal for ^{1}H was referenced to TMS at $\delta = 0.00$, coupling constants were recorded in hertz (Hz) to one decimal place.

6.2.7   Nuclear Overhauser effect spectroscopy (2D NMR)

The nuclear Overhauser effect (NOE) is observed as a change in intensity of one resonance when the intensity of another resonance is perturbed. It is caused by the relaxation of one spin by a neighbouring spin. Take a system consisting of two NMR-active nuclei, S and I. In a NOE experiment, the equilibrium of the S nucleus is perturbed with an R_f pulse at its Larmor frequency, thus there is now an equal population of S nuclei aligned with (α) and against (β) the magnetic field. Once the R_f pulse is turned off, S will subsequently return to equilibrium by relaxation processes. This relaxation of S toward equilibrium can also involve I, if the two are close enough together in space (typically within 5 Å), leading to perturbation of the
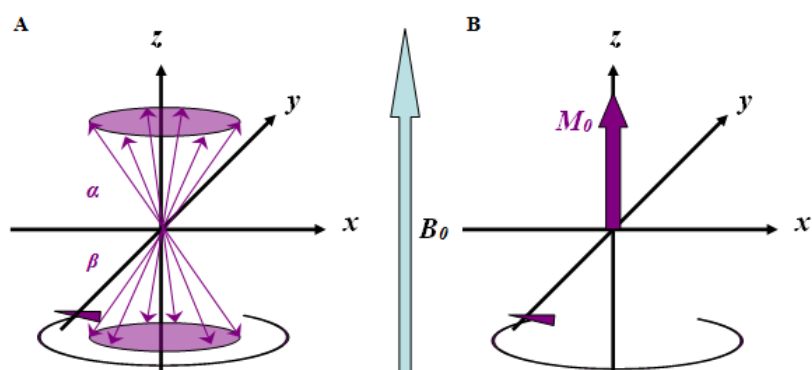
(a) A) Schematic representation of the precession of magnetic moments around the z-axis in the presence of a magnetic field, B_0. B) Simplified schematic demonstrating the excess spin alignment creating a net magnetisation, M_0.
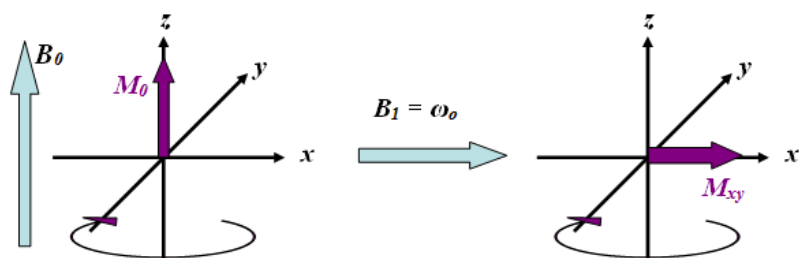
(b) Schematic illustration of resonance, the condition where the applied radiofrequency (B_1) equals the Larmor frequency (ω_o) and the net magnetisation changes plane.

Figure 6.1: ^{1}H NMR Spectroscopy
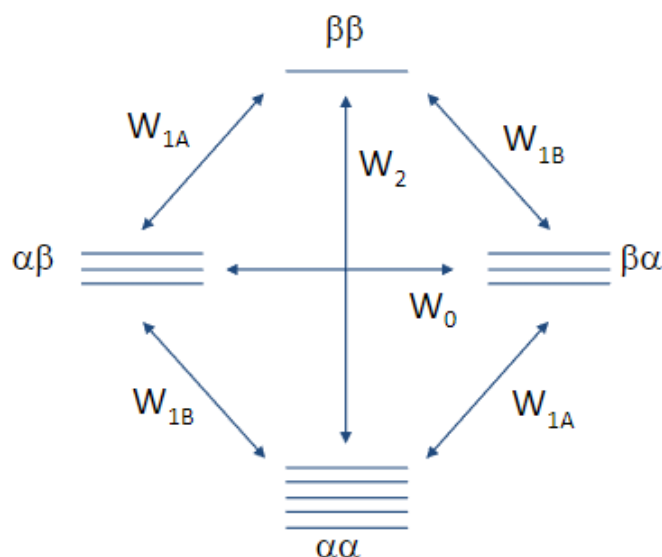
Figure 6.3: Energy levels and transitions of a two-spin system. Each spin can be in spin state α or β. The total spin state is described by listing the state of I first and then S, so, for example, state is the state in which I is in α and S is in β. Figure reproduced from Williamson.[2]

populations of I and hence a change in intensity and a NOE at I arising from the initial perturbation of S. There are two relaxation pathways that contribute to the NOE, the W_2 and the W_0 mechanism (Figure 6.3). The W_2 mechanism is where the S spin relaxes down to its ground state, the coupled I spin also flips from a high energy state down to the ground state. This increases the population difference as now more I spins are at the ground state than should be at equilibrium, thus causing a positive NOE. The converse of this is the The W_0 mechanism where the S spin relaxes down to its ground state, the coupled I spin also flips, but this time from the ground state to a high energy state. This decreases the population difference as now less I spins are at the ground state than should be at equilibrium, thus causing a negative NOE.[2] The NOE is a useful tool because the W_2 mechanism is dominant in small molecules such as unbound ligands whereas the W_0 mechanism is dominant in larger molecules that are conformationally restricted, such as a ligand bound to a nanoparticle.

Spectra were recorded in deuterated solvents with a Bruker Advance DPX-400 MHz spectrometer at frequency 400.13 MHz for ^{1}H. The signal for ^{1}H was referencesto

TMS at $\delta = 0.00$.

6.2.8   Mass spectrometry

Electro mass spectra were recorded on a Mass Lynx NT V 3.4 on Waters 600 controller connected to a 966 photodiode array detector with HPLC-grade MeOH as carrier solvent. A peak matching method was used to determine accurate molecular weights using leucine enkephaline (H-Tyr-Gly-Gly-Phe-Leu-OH) as the standard reference (m/z = 556.2771); all accurate masses were reported within 5 ppm of the expected mass.

6.2.9   Photoluminescence spectroscopy

Photoluminescence or fluorescence spectroscopy is a type of electromagnetic spectroscopy used for analysing materials which emit radiation upon absorption of light. Absorption of a photon of light, usually ultraviolet light, excites the electrons in molecules of certain compounds from their ground state to a vibrational state within the molecule's excited electronic state. Collisions with other molecules cause the loss of vibrational energy until it reaches the lowest state of its excited form. Emission of a photon of light occurs when the electron falls from this excited state back to the ground state. Electrons which fall to different vibrational levels of the ground state have different energies, which results in the emission of different frequencies of light. Analysis of these frequencies allows the identification of the different vibrational levels within a molecule. The fluorescent lifetime of a molecule refers to the time the molecule stays in its excited state before emitting a photon. Phosphorescence refers to emission of a photon of light from the triplet excited state of a molecule. This state is lower in energy than the singlet excited state and becomes occupied by an electron if the spin of the excited state is reversed, via intersystem crossing. The Jablonksi diagram describes the various relaxation mechanisms for excited state molecules (Figure 6.4).

Photoluminescence measurements were carried out using a Perkin Elmer LS55 Lumi-
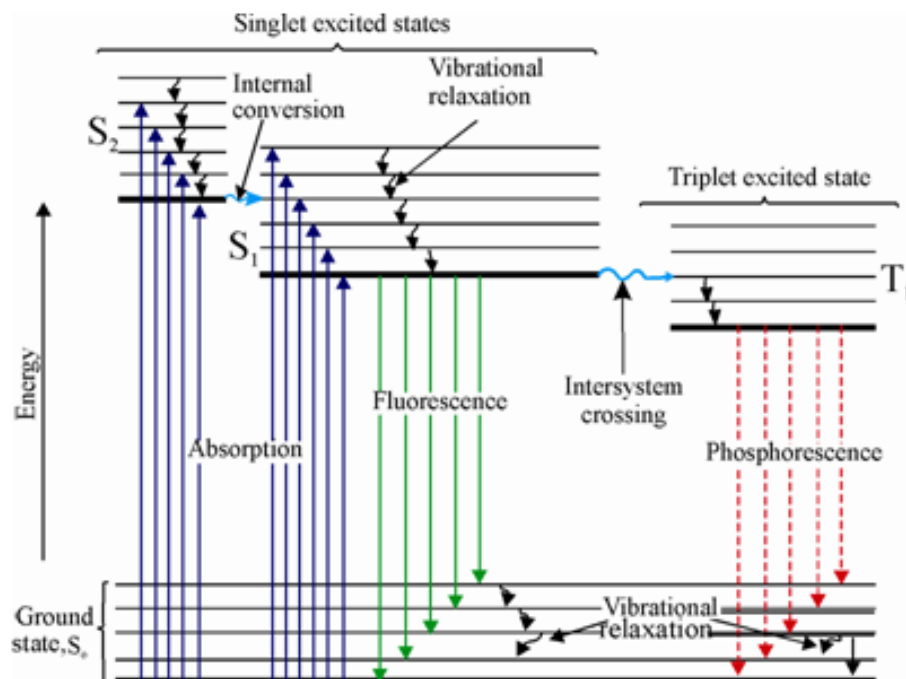
Figure 6.4: Jablonski diagram showing the absorption and relaxation mechanism of radiation within the electronic states of a molecule. Figure reproduced from the ref.[3]

nescence spectrometer. The photoluminescence lifetime and time resolved emission spectra measurements were performed by a time correlated single photon counting spectrometer (Fluorolog 3 Horiba Jobin Yvon) and a diode laser (261 nm "Nano LED" – HORIBA Jobin Yvon) with pulse duration shorter than 1 ns for excitation.

Relative quantum yields were calculated by the comparison of PL intensity between a sample and a standard dye, which have well-known quantum yields and calculated using the following equation:

$$\Phi_x = (\frac{A_s}{A_x})(\frac{F_x}{F_s})(\frac{n_x}{n_s})^2 \Phi_s$$

Where Φ is the quantum yield, A is the absorbance, F is the integrated fluorescence and x and s subscripts are for the sample being tested and the standard, respectively.
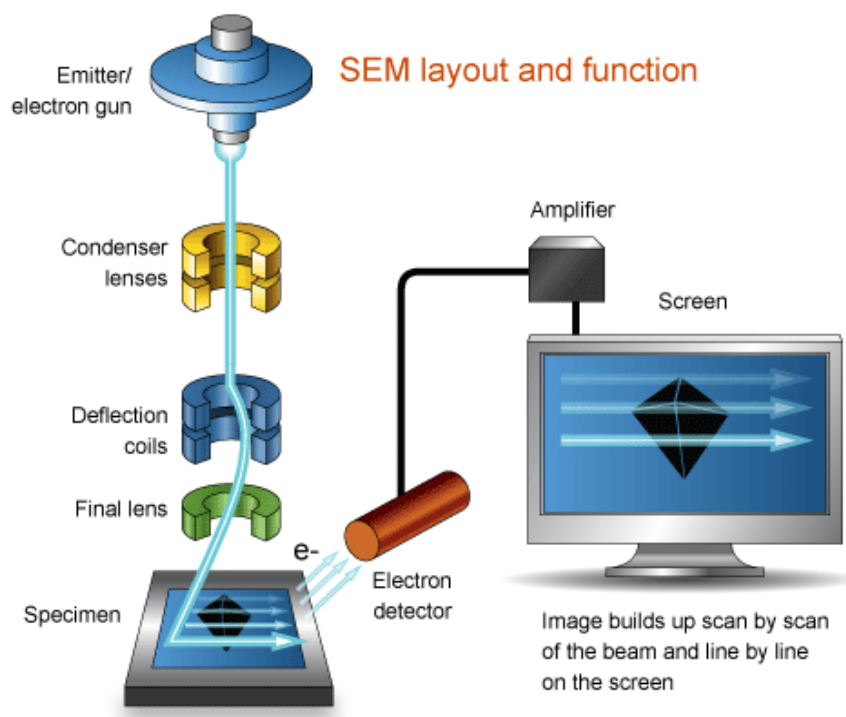
Figure 6.5: Diagram showing the basic structure of an SEM microscope. This figure was reproduced from ref.[4]

6.2.10   Raman spectroscopy

Performed using a Renishaw inVia Raman Microscope equipped with a 785 nm Renishaw HP-NIR laser.

6.2.11   Scanning electron microscopy

In scanning electron microscopy (SEM), a focused beam of electrons is passed over the surface of a material. As the electrons strike the surface of the sample, they interact with it and these interactions result in the emission of electrons and photons, including secondary electrons, backscattered electrons and x-rays. These can be collected and formed into various types of SEM images. The basic operating principles of an SEM is shown in Figure 6.5.

Performed using a Zeiss Ultra Plus SEM. Samples were dropped frm Millipore water onto lacey carbon coated TEM grids. The samples were dried under reduced pressure for 24 hours before imaging.

6.2.12   Scanning transmission electron microscopy

Performed using an FEI Titan TEM. Samples were dropped from Millipore water onto lacey carbon coated TEM grids. The samples were dried under reduced pressure for 24 hours before imaging.

6.2.13   Thermogravimetric analysis

Thermogravimetric analysis is a technique which monitors the temperature-dependant weight loss of a material. It can give information about the behaviour of materials and compounds at different temperatures, the stability and stoichiometry of a reaction, and more commonly, the composition of functionalised materials.[5] The machine operates by combining a microbalance with a temperature-programmable furnace. It provides a curve of percentage weight loss against the temperature range scanned.

TGA was conducted on a Stanton Redcroft STA-1500 using a platinum crucible.

6.2.14   Transmission electron microscopy

Transmission electron microscopes have similar designs to optical microscopes, except that the source which is used to visualise the sample is a beam of electrons instead of a beam of light. TEM can provide details on the morphology, topography, composition and crystallographic information of a sample. The basic operating principle of this instrument is shown in Figure 6.6

Performed using an FEI Titan TEM operating at 300 kV. Samples were dropped from Millipore water onto lacey carbon coated TEM grids. The samples were dried under reduced pressure for 24 hours before imaging.
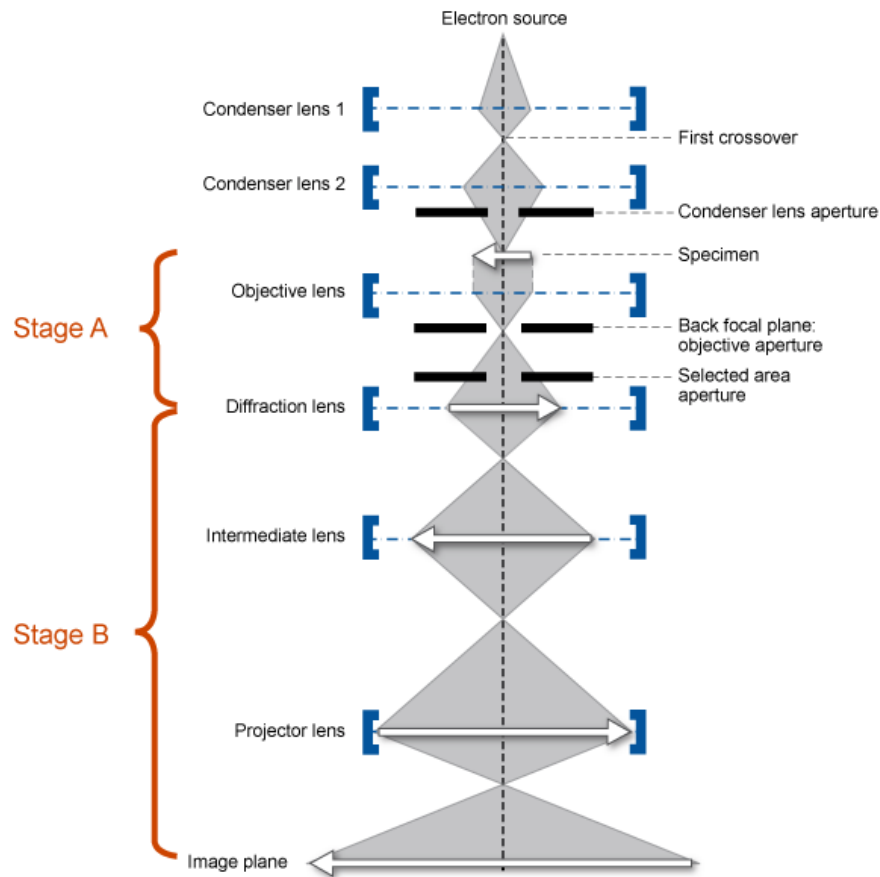
Figure 6.6: Diagram showing the basic structure of a TEM microscope. Stage A is the scattering of an incident electron beam by a specimen. This scattered radiation passes through an objective lens, which focuses it to form a primary image obtained in stage A and magnifies this image using additional lenses to form a highly magnified final image. This figure was reproduced from ref.[6]

6.2.15   UV-vis spectroscopy

UV-visible spectra arise as a result of the absorption of a beam of incident photons by a sample. The region of the electromagnetic spectrum generally measured for this technique is from 200-900 nm (covering both the UV and the visible range). The Beer-Lambert law (Equation 7) demonstrates that the absorption of light (A) is directly proportional to the path length of the cell used (l) and the concentration (c) of the sample under investigation:

$$A = \varepsilon c l$$

Where   is the extinction coefficient of the substance (M^{-1} cm^{-1}). Bands in UV-vis spectra correspond to electronic transitions, as absorption of the incident light promotes excitation of the valence electrons in a molecule. The wavelength (and also the intensity) of the absorbed photon is directly proportional to the energy difference between the ground and excited levels. The wavelength of absorption of radiation is characteristic of the material under investigation.

UV–vis absorption spectroscopy was carried out using a Perkin Elmer LAMBDA 1050 UV/vis/NIR spectrophotometer. The scans were performed using a quartz cuvette of path length 10 mm.

6.2.16   X-ray powder diffraction

X-ray diffraction (XRD) is the scattering of light by a periodic array of atoms in a sample. This diffraction of light can used to construct a pattern to describe the periodic array of atoms. When studying XRD patterns, Miller indices are used to describe planes of atoms using (hkl) coordinates. The d_{hkl} vector which extends from the origin to the hkl plane is used in tandem with Bragg's Law to estimate diffraction peaks:

$$\lambda = 2d_{hkl}sin\theta$$
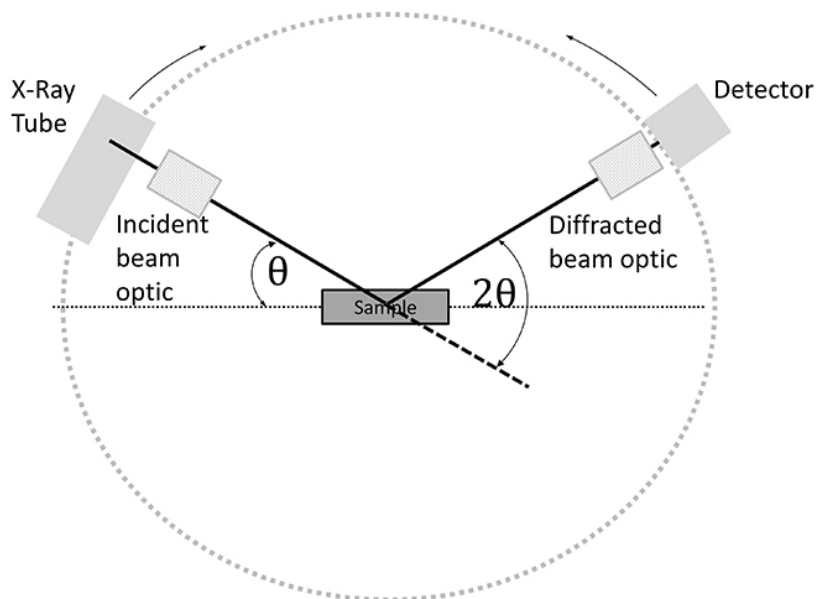
Figure 6.7: An illustration of Bragg-Bretano geometry used for x-ray powder diffraction where θ is the incident angle and 2θ is the diffraction angle. Figure reproduced from ref.[7]

The wavelength λ, is usually fixed. The angle θ, which causes constructive interference from x-ray will produce diffraction peaks.

Powder x-ray diffraction is a specific case which utilises Bragg-Bretano geometry to calculate a diffraction pattern (Figure 6.7. The sample is typically rotated to increase the number of crystallites observed and thus obtain a more reliable diffraction pattern.

The Scherrer equation can be used to calculate the crystallite size through its relationship to the width of a specific peak:

$$\tau = \frac{K}{\beta Cos\theta}$$

Where τ is the mean ordered crystallite size, K is the shape factor which is typically taken to be 0.9 but is dependent upon the crystallite shape, β is the peak width and θ is the Bragg angle.

XRD patterns were recorded using a Bruker D2 Phaser diffractometer. Patterns were recorded with a 2.2 hour scan time.

6.3 Chapter 2 Experimental Section

6.3.1 Synthesis of chiral and luminescent TiO$_2$ nanoparticles

625 mg (1R,2R)-(+)-DPEN was placed into a 100 mL three-neck round bottom flask containing 30 mL of degassed, anhydrous benzyl alcohol. The flask was then purged with Argon before 0.75 mL of TiCl$_4$ was added dropwise with stirring. The reaction was then heated to 60 °C (a yellow solution was observed) for 48 hr (at which point a white precipitate was obtained). The product was recovered by centrifugation and washed twice with 15 mL of EtOH. The product was then dried under reduced pressure to obtain a white powder.

6.3.2 Synthesis of OA-capped TiO$_2$ nanorods for ^{1}H NMR analysis

Procedure adapted from Joo *et al.*[8] 28 mL (25 g) of oleic acid was heated to 110 °C for 1 hour to degas and remove water. The solution was then cooled to room temperature before 8.85 mL titanium isopropoxide was added. The solution was then heated to 270 °C for 2 hours. After cooling, the TiO$_2$ NPs were precipitated with acetone. The solution was then centrifuged, washed once with acetone and dispersed in 20 mL deuterated chloroform to yield a clear solution of TiO$_2$ nanoparticles.

6.3.3 Phase transfer of OA-capped TiO$_2$ nanorods with disodium tartrate

A 5 mL solution of OA-capped TiO$_2$ nanorods of known concentration (which was determined by recording the weight of NPs after removal of the solvent under reduced pressure of a sample of 1 mL of NPs) was added to 5 mL solution of D- or L-disodiumtartrate (1 mol equivalent) in Millipore water. The two layers were stirred vigorously overnight before and the aqueous layer was separated using a separating funnel. The aqueous layer was then centrifuged to remove any precipitate and the supernatant layer was kept. The supernatant layer now contains water soluble

chiroptically-active TiO_2.

6.3.4 Synthesis of linear polyethylenimine

0.5g of poly(2-ethyl-2-oxazoline) (5 mmols) was dissolved in 10 mL of 5 M HCl. The solution was stirred at 90 °C for 10 hours, after which the insoluble white precipitates were filtered and washed three times with acetone. In ^{1}H NMR (D_2O), a single peak at 3.4 ppm was observed ($-NCH_2CH_2-$). This powder was stirred in a solution of 5 M ammonia for 1 hour . The insoluble precipitates were then collected by filtration and dried under reduced pressure at 40 °C for 6 hours to obtain a crystalline white solid. Yield 159 mg, 74 %.

^{1}H NMR (400 MHz, D_2O): 3.17 (s, 4H)

6.3.5 Synthesis of tartaric acid@PEI TiO_2

316 mg PEI (4.0 mmol) was dissolved in 4 mL Millipore water at 100 °C. To this a solution of D- or L-tartaric acid (300 mg, 2.0 mmol) in 4 mL Millipore water was added to the solution and stirred for 10 minutes at 100 °C. After the solution was cooled to room temperature, 4.1 mls of 75 wt. % solution of titanium diisopropoxide bis(acetylacetonate) in isopropanol was added slowly and the reaction was heated to 55 °C for 4 hours. The resulting precipitates were centrifuged and washed with 20 mL of Millipore water and 20 mL of ethanol before being dried in air at room temperature overnight.

6.3.6 Synthesis of 16-2-16 gemini surfactant

3.0 mls of N,N,N',N'-tetramethylethylenediamine (20 mmols) and 4.9 mls 1-bromohexadecane (16 mmol) were heated at 40 °C in 50 ml acetonitrile for 72 hours. After evaporation of the solvent and recrystallisation from ethanol, 5.45 g of hexadecyl dimethyl [1-(2-dimethylamino)ethyl] ammonium bromide was obtained, the identity of which was confirmed by ^{1}H NMR. 3 g of this product was then added to 8.7mls 1-

bromohexadecane in 70 ml ethyl acetate and the mixture was refluxed for 2 days. After evaporation of the solvent, the residue was then recrystallised 4 times from a 50/50 mixture of $CHCl_3$ and acetone to afford a white solid. Yield: 2.71 g, 52 %.

^{1}H NMR (400 MHz, CDCl$_3$): 3.71 (s, 4H), 3.59 (t, 4H, J=8.2), 3.23 (s, 12H), 1.83 (s, 4H), 1.41 (s, 4H), 1.28 (s, 48H), 0.90 (t, 6H, J=6.5)

6.3.7   Synthesis of 16-2-16 gemini tartrate

103 mg of D-tartaric acid (0.69 mmol) and 95 mg Ag_2CO_3 (0.5 equivalents) were stirred vigourously in 10 mL Millipore water for 1 hour. 500 mg (0.88 mmol) of the 16-2-16 gemini surfactant was added and the mixture stirred for 5 minutes. After evaporation of the solvent, the resulting powder was dissolved in methanol and filtered through Celite to give a colourless solution. After evaporation, the product was dissolved in a mixture of chloroform/methanol (9/1, v/v), precipitated upon addition of ethyl acetate, filtered, and then dried. Yield 473 mg, 96 %.
The formation of the 16-2-16 gemini D-tartrate was confirmed by mass spectrometry: HRMS (m/z) (ES+): Calculated for $C_{42}H_{87}N_2O_{11}$ m/z = 715.6564 Found for $[M+H]^+$ $C_{42}H_{87}N_2O_{11}$ m/z = 715.6564

6.3.8   Synthesis of silica nanohelices

The synthesis was performed according to a procedure reported by Delclos *et al.*:[9]

A 5 mM solution of 16-2-16 gemini D-tartrate in Millipore water was heated to 45 °C for 15 minutes and then cooled to room temperature. 500 μl of this solution was then transferred to an Eppendorf, the tubes were sealed, and the gel was aged for 21 days. After this aging process, 500 μl of a 15 % w/w solution of TEOS in Millipore water which had been stirred vigorously for 12 hours was added to the Eppendorf. The mixture was then agitated with a vortex so as to increase the contact. The Eppendorf is then left in static conditions for 36 hours. Once the transcription was over, the mixture was washed with an excess of ethanol, in order to solubilize the organic by-products. A drop of the hybrid material suspension was then deposited

directly on a TEM grid for SEM analysis. The remainder of the suspension was then calcined in air in a furnace (1 hour at 100 °C, 1 hour at 200 °C, and 3 hours at 450 °C).

6.3.9 Synthesis of TiO$_2$ nanohelices

5 mM solution of 16-2-16 gemini D-tartrate in Millipore water was heated to 45 °C for 15 minutes and then cooled to room temperature. 500 μl of this solution was then transferred to an Eppendorf, the tubes were sealed, and the gel was aged for 21 days. After this aging process, 500 μl of Titanium diisopropoxide bis(acetylacetonate) (75 wt. % in isopropanol) was added to the Eppendorf. The mixture was then agitated with a vortex so as to increase the contact. The Eppendorf is then left in static conditions for 36 hours. Once the transcription was over, the mixture was washed with an excess of ethanol, in order to solubilise the organic by-products. A drop of the hybrid material suspension was then deposited directly on a TEM grid for SEM analysis. The remainder of the suspension was then calcined in air in a furnace (1 hour at 100 °C, 1 hour at 200 °C, and 3 hours at 450 °C).

6.3.10 Epoxidation reaction procedure

0.30 g of chalcone (14.5 mmol, 1,3-Diphenyl-2-propen-1-one) is dissolved in 5.0 ml toluene in presence of 0.05g of TiO$_2$ NPs in a 25 ml 2 neck RBF. The mixture is then stirred and purged with argon for 15 minutes before adding 0.25 ml of TBHP (14 mmol, 5.5 mol/L in decane) or 0.2 ml H$_2$O$_2$ (27.5 wt % H$_2$O$_2$ in H$_2$O). The reaction is heated to 60°C for a time ranging between 24h and 72h. The reaction was monitored by TLC (chalcone/oxide chalcone = 1.24 in ratio solvent of 1/10 ethyl acetate and hexane). The mixture was centrifuged at 5000 rpm (rotations per minute) to recover the catalyst. The catalyst was then washed three times with 10 ml of ethanol and two times with 10 ml Millipore water. The solution was evaporated under reduced pressure before purification by column chromatography (ratio solvent of 10/1 of ethyl acetate and hexane).

¹H NMR (CDCl₃, 400 MHz): 8.05-8.10 (d, 2H), 7.60-7.65 (t, 1H), 7.51-7.55 (t,

2H), 7.32-7.38 (m, 5H), 4.35 (d, 1H), 4.10 (d, 1H)

6.3.11 Aldol reaction procedure

0.05 g of TiO$_2$ NPs were suspended in a 2 neck-RBF containing 5 ml acetone (68 mmol) or 3 ml of cyclohexanone (28 mmol) and 2 ml toluene. Then, either 0.2 ml of benzaldehyde (2 mmol) RBF or 0.20 g p-nitro benzaldehyde (1,4 mmol) was added under an argon atmosphere. In all cases, the mixture was heated to 60°C for a ranging time between 24 and 72h depending on the reaction. The progresses of reactions were analysed by TLC (ratio $\frac{1}{4}$ ethyl acetate and hexane). After reaction, the mixture was centrifuged at 5000 rpm for 15 minutes to recover the catalyst and the catalyst was washed three times with 10 ml of distilled water and twice with 10 ml ethanol. The solvent in there action mixture was then evaporated under reduce pressure and and the products were purified by column chromatography (ratio 1/5 of ethyl acetate and hexane).

^{1}H NMR (CDCl$_3$, 400 MHz): 8.21(2H, d, 3JHH=8.0 Hz, pyH), 7.54(2H,d, 3JHH=8Hz, pyH), 5.26(1H,m, CHOH), 2.85 (2H,m, CH2), 2.22(3H, s, CH3) ppm.

6.3.12 Oxyalkylation of trans-anethole procedure

Oxyalkylation of trans-anethol [(E)-1-Methoxy-4-(1-propenyl)benzene] in the presence of a catalyst TiO$_2$ NPs were carried under atmosphere. 0.05 g of catalyst was dispersed in 2-neck RBF of 25 ml containing 5 ml of THF (62 mmol). Then 0.10 ml (100 mg, 0.67 mmol) of trans-anethol was added to the RBF and the mixture is refluxed for a ranging time between 24h and 72h. The reaction was monitored by TLC (ratio solvent of 1/1 ethyl acetate and hexane). The mixture is then centrifugated at 5000 rpm to recover the catalyst, which was then washed three times with 10 ml distilled water and twice with 10 ml ethanol. The solvent in the reaction mixture was evaporated under reduced pressure and the product was purified by column chromatography (ratio 3/10 of ethyl acetate and hexane).

^{1}H NMR (CDCl$_3$, 400 MHz): 7.00-8.00 (m, 4H), 6.956.92 (m, 2 H), 4.194.13 (m, 1 H), 3.87 (s, 3 H), 3.853.81(m, 2 H), 3.743.69 (m, 1 H), 3.593.55 (m, 1 H),1.941.88

(m, 2 H), 1.681.61 (m, 1 H)

6.4   Chapter 3 Experimental Section

6.4.1   Synthesis of chiral Mn$_3$O$_4$ nanoparticles

100 mg of MnCl$_2$.4H$_2$O , 150 mg of SDS (sodium dodecyl sulfate) and 100 mg of R,R-DPEN or S,S-DPEN were added to a 100 mL 3-neck RBF containing 10 ml of distilled water and stirred vigorously until a colloidal solution was obtained. 7.5 ml of a solution of 4 M NaOH was then added dropwise over 10 min and then stirred for 15 minutes. The mixture was then transferred to a 23ml PTFE-lined hydrothermal vessel and heated at 120°C for 1 hour. The mixture was then left to cool down and washed respectively with 15ml distilled water and 15 ml ethanol. The sample was then dried under reduced pressure. Yield 22 mg, 19 %. The same experimentation has been used to synthesise different functionalised manganese oxide NPs in presence of different chiral ligand; R- or S-BINOL , R- or S-BINAP, (+)-cinchonidine and R- or S-DACH .

6.4.2   Epoxidation procedure

Carried out analogously to the reaction procedure given for the TiO$_2$ NPs in Section 6.3.10.

6.4.3   Aldol reaction procedure

Carried out analogously to the reaction procedure given for the TiO$_2$ NPs in Section 6.3.11.

6.4.4 Oxyalkylation of trans-anethole procedure

Carried out analogously to the reaction procedure given for the TiO_2 NPs in Section 6.3.12.

6.4.5 Preparation of Mn_3O_4 working electrodes

A 5 % wt. dispersion of D- or L- tryptophan functionalised Mn_3O_4 nanoparticles was dispersed in a solvent mixture composing of 0.25 g ethyl cellulose, 1.2 mL terpinol and 0.3 mL heptanol. The nanoparticle dispersion was then applied to indium-tin oxide coated conductive glass using a doctor-blade technique to make a 1 cm^2 working electrode. The working electrodes were then annealed at 200 °C for 1 hour.

6.4.6 Electrochemical oxidation of L-tryptophan with Mn_3O_4 working electrode

Cyclic voltammetry potential was swept from 0.1 o 1.4 V with a sweep rate of 0.005 V s^{-1}.

6.4.7 MTT assay protocol

This assay was carried out by a collaborator using the following procedure:

When BT-549 cells have reached confluence in a flask, aspirate the media (RMPI-1640 with 10 % foetal calf serum (FCS), 50 units/ml penicillin and 50 µg/ml strep-tomycin), rinse in PBS and add 2ml of trypsin/ EDTA and incubate for 3 minutes. When all cells have detached from the flask surface, add the cell suspension to a 50 ml tube containing RPMI-1640 to inactivate trypsin. Centrifuge at 1,000 rpm for 3 minutes, remove the media without disturbing the cell pellet. Re-suspend the cells in 1 ml of cell culture media. Using a haemocytometer, count the number of cells in 1 ml of media and then adjust for 1 x 10^4 cells per well. Add the desired volume to each well. Each concentration of NPs was prepared in quadruplicate. The next day,

weigh out 0.0128 g of nanoparticles and add them to 20 ml of RPMI-1640 containing 10 % FCS. Mixture was then sonicated and each condition was made up as shown in Table 6.1 below.

Nanoparticle conc. (µg/ml)	Volume of media containing NPs (µl)	Volume of media (µl)
640	200	200
320	100	100
160	50	150
80	25	175
40	12.5	187.5
20	6.3	194
10	3.15	197
5	1.5	198.5
0	0	200

Table 6.1: MTT assay conditions

The incubation lasted for 24 hours. A solution of 5mg/ml of MTT dissolved in PBS and sterile filtered was made. Add 20 µl of MTT solution was added to each well and incubated for 5 hours at 37 °C. When this was complete, the media was aspirated and 200 µL of DMSO was added to each well. This lyses the cells and dissolves the formazan crystals. The 96-well plate was read at an absorbance of 590 nm.

6.5   Chapter 4 Experimental Section

6.5.1   Synthesis of N-stearoyl-L-glutamic methyl diester

0.375 mL $SOCl_2$ was added to 0.5 g (4.8 mmol) of L-glutamic acid in 10 mL an-
hydrous MeOH at 0 °C. The solution was left to stir overnight before the solvent
was evaporated under reduced pressure to yield a clear oil. 20 mL $CHCl_3$ was then
added to dissolve this oil before 4.0 mmol stearoyl chloride was slowly added. Upon
addition of 1.1 mL (8.0 mol) triethylamine, an exothermic reaction was observed.
The reaction was then left to stir at room temperature overnight. The solvent was
then evaporated under reduced pressure before the resulting off-white powder was
purified by column chromatography. Yield 1.865 g, 88 %.

^{1}H NMR (400 MHz, CDCl$_3$): 6.19 (1H, d), 4.66 (1H, m), 3.78 (3H, s), 3.70
(3H, s), 2.42 (2H, dm), 2.24 (2H, m), 2.03 (2H, m), 1.65 (2H, t), 1.28 (24H, s), 0.90
(3H, t)

6.5.2   Synthesis of N-stearoyl-L-glutamic acid

500 mg (1.1 mmol) of N-stearoyl-L-glutamic methyl diester was dissolved in 20 mL
THF mixed with 10 mL Millipore water. 142 mg (3.3 mmol) $LiOH.H_2O$ was then
added and the mixture was left stirring overnight. The reaction was then quenched
with 5 mL 2 M HCl. The products were extracted with 20 mL ethyl acetate before
being washed with 20 mL brine and dried over anhydrous sodium sulfate. Yield 455
mg, 99 %.
^{1}H NMR (400 MHz, CDCl$_3$): 4.45 (1H, m), 2.46 - 2.14 (8H, m), 1.95 (2H, m),
1.64 (2H, t), 1.31 (24H, s), 0.92 (3H, t)

6.5.3   Synthesis of 1-(1H-benzo[d][1,2,3]triazol-1-yl)octadecan-1-one

2.845 g (0.01 mol) stearic acid and 4.8 g (0.04 mol) benzotriazole were dissolved in
25 mL DCM. 0.75 mL (0.01 mol) $SOCl_2$ was then added dropwise. The solution

was left overnight at which point a white precipitate was observed. The precipitate was filtered and washed with DCM (2 x 20 mL). The combined organic layer was washed with 2 M NaOH (2 x 50 mL), dried over anhydrous sodium sulfate and the solvent was removed under reduced pressure. Yield 2.774 g, 72 %.

^{1}H NMR (CDCl$_3$, 400 MHz): 8.24 (2H, dd), 7.61 (2H, dt), 3.45 (2H, t), 1.93 (2H, m), 1.60 (2H, s), 1.51 (2H, m), 1.24 (24H, s), 0.90 (3H, t)

6.5.4   Synthesis of N-stearoyl-L-cysteine

This synthetic procedure was adapted from a synthesis reported by Katritzky *et al.*[10]

To a solution of L-cysteine (3.0 mmol, 363 mg) and triethylamine (3.0 mmol, 0.42 mL) in CH$_3$CN-H$_2$O (3:1, 12 mL), 1.156 g (3.0 mmol) 1-(1H-benzo[d][1,2,3]triazol-1-yl)octadecan-1-one was added. The solution was stirred at room temperature for 2 hours before the solvent was removed under reduced pressure. The product was then added to 20 mL EtOH and filtered. The filtrate was then evaporated under reduced pressure to yield a white powder. Yield 639 mg, 55 %.

^{1}H NMR (400 MHz, CDCl$_3$): 15.74 (1H, b), 8.12 (1H, d), 4.38 (1H, m), 2.79 (2H, dm), 2.15 (2H, t), 1.49 (2H, m), 1.24 (24H, s), 0.86 (3H, t)

6.5.5   Synthesis of succinic-N-stearoyl

10g (0.035 mol) stearic acid, 6 g (0.052 mol) N-hydroxysuccinimide was dissolved in 80 mL THF and cooled in an ice bath. 9 g (0.044 mol) dicyclohexylcarbodiimide was then added while stirring and left overnight. The resulting mixture was then filtered, the solvent evaporated under reduced pressure and finally recrystallised from isopropanol. Yield 8.956 g, 70 %.

^{1}H NMR (400 MHz, CDCl$_3$): 2.87 (4H, s), 2.63 (2H, t), 1.77 (2H, m), 1.62 (2H, m), 1.43 (2H, m), 1.28 (s, 24H), 0.88 (3H, t)

6.5.6 Synthesis of N-stearoyl-L-alanine

1.096 g (3 mmol) succinic-N-stearoyl in 12mLs THF was slowly added to a solution of 294 mg L-alanine (3.3 mmol) and 756 mg sodium bicarbonate in 12 mL H_2O. Was left to stir at room temperature overnight before th solvent was removed under reduced pressure, redissolved in 50 mL water and the pH adjusted to 3 with 1 M HCl. The product was then extracted twice with 50 mL ethyl acetate and the organic extracts washed with H_2O and brine. The product was then dried over Na_2SO_4 and the solvent removed under reduced pressure. Yield 586 mg, 65 %.

^{1}H NMR (400 MHz, CDCl$_3$): 4.61 (m, 1H), 2.28 (t, 2H), 1.66 (m, 2H), 1.53-1.23 (m, 26H), 0.91 (t, 3H)

6.5.7 Preparation of N-stearoyl-glutamic acid functionalised ZnO

50 mg (0.1 mmol) N-stearoyl-glutamic acid was stirred in 10 mL Millipore water. 11 mg (0.1 mmol) sodium carbonate was then added and the solution stirred for 15 minutes. After 15 minutes, a clear solution was obtained. 14 mg (0.1 mmol) $ZnCl_2$ was then added and the solution stirred for 1 hour. The aqueous layer was then extracted twice with 10 mL CHCl$_3$ and the organic layer dried over anhydrous Na_2SO_4. The solvent was then removed under reduced pressure. 15 mg of this Zinc glutamate complex was then dissolved in 10 mL EtOH and 1.4 mg (1 equivalent) LiOH.H_2O dissolved in 1 mL EtOH was added. The solution was then refluxed for 1 hour to obtain ZnO QDs.

6.5.8 Preparation of N-stearoyl-cysteine functionalised ZnO

77 mg (0.2 mmol) N-stearoyl-cysteine was stirred in 10 mL Millipore water. 11 mg (0.1 mmol) sodium carbonate was then added and the solution stirred for 15 minutes. After 15 minutes, a clear solution was obtained. 14 mg (0.1 mmol) $ZnCl_2$ was then added and the solution stirred for 1 hour. The aqueous layer was then extracted twice with 10 mL CHCl$_3$ and the organic layer dried over anhydrous Na_2SO_4. The

solvent was then removed under reduced pressure. 30 mg of this Zinc glutamate complex was then dissolved in 10 mL EtOH and 1.5 mg (1 equivalent) LiOH.H_2O dissolved in 1 mL EtOH was added. The solution was then refluxed for 1 hour to obtain ZnO QDs.

6.5.9   Preparation of N-stearoyl-alanine functionalised ZnO

71 mg (0.2 mmol) N-stearoyl-aspartic acid was stirred in 10 mL Millipore water. 11 mg (0.1 mmol) sodium carbonate was then added and the solution stirred for 15 minutes. After 15 minutes, a clear solution was obtained. 14 mg (0.1 mmol) $ZnCl_2$ was then added and the solution stirred for 1 hour. The aqueous layer was then extracted twice with 10 mL $CHCl_3$ and the organic layer dried over anhydrous Na_2SO_4. The solvent was then removed under reduced pressure. 30 mg of this Zinc glutamate complex was then dissolved in 10 mL EtOH and 1.6 mg (1 equivalent) LiOH.H_2O dissolved in 1 mL EtOH was added. The solution was then refluxed for 1 hour to obtain ZnO QDs.

6.6 Chapter 5 Experimental Section

6.6.1 Synthesis of ethyl picolinimidate

Sodium metal (0.05 grams, 2.17mmol) was added to a solution of 2-cyanopyridine(2g, 19.21mmol) in EtOH (30ml) and stirred at room temperature for 48hours. Glacial Acetic acid(0.136ml, 2.387mmol) was then added to quench the reaction and the solvent removed under reduced pressure. The crude product was dissolved in CH_2Cl_2(50ml), washed with water(2x50ml), brine (1M,50ml) and dried over Na_2SO_4. After filtering the solvent was removed under reduced pressure to give the product as a light brown oil.(1.303 g, 45.20 %)

^{1}H NMR (400 MHz, CDCl$_3$): 9.03 (1H, br s, NH), 8.53 (1H, dd, 3JHH : 7.7 and 5.6 Hz, pyH), 7.27 (1H, m,pyH), 4.36 (2H, q, 3JHH=7.1 Hz, CH2), 1.37 (3H, t, 3JHH=7.1 Hz, CH3) ppm

6.6.2 Synthesis of (S)-4-phenyl-2-(pyridin-2-yl)-4,5-dihydrooxazole

A solution of ethyl picolinimidate (392mg, 2.61mmol), CHCl$_3$ (15mls), and s-(+)-phenylglycinol(358mg, 2.61mmol) was stirred at 60 °C for 16 hours. The solution was washed with Millipore water(2x30ml) and brine (1M , 30mls) and dried over Na_2SO_4. It was then filtered and the solvent was removed under reduced pressure to give the product as a brown viscous oil. Yield 533 mg, 91 %

^{1}H NMR (400 MHz, CDCl$_3$): 8.67 (1H, d, 3JHH = 6.0 Hz, pyH), 8.08 (1H, d, 3JHH = 7.9 Hz, pyH), 7.71 (1H, app. t, 3JHH=7.9 Hz, pyH), 7.36 (1H, m, pyH), 7.30-7.18 (5H, m, PhH), 5.38 (1H, app t, app. 3JHH = 8.6 Hz, CHPh), 4.81 (1H, app.t, app. JHH = 8.6 Hz, CHHO), 4.30 (1H, app. t, app. JHH = 8.5 Hz, CHHO) ppm

6.6.3 Synthesis of (S)-4-phenyl-2-(4-methylpyridin-2-yl)-4,5-dihydrooxazole

A solution of ethyl 4-methylpicolinimidate (392mg, 2.61mmol), $CHCl_3$ (15mls), and s-(+)-phenylglycinol(358mg, 2.61mmol) was stirred at 60 °C for 16 hours. The solution was washed with Millipore water(2x30ml) and brine (1M , 30mls) and dried over Na_2SO_4. It was then filtered and the solvent was removed under reduced pressure to give the product as a brown viscous oil. Yield 591 mg, 95 %.

^{1}H NMR (400 MHz, CDCl$_3$): 8.61 (d, 1H), 8.05 (s, 1H), 7.42-7.23 (m, 6H), 5.47 (t, 1H), 4.92 (t, 1H), 4.41 (t, 1H), 2.23 (s, 3H)

6.6.4 Synthesis of (R)-4-hydroxy-4-(4-nitrophenyl)butan-2-one using CeO$_2$/ligand self assembled base catalyst

CeO_2 nanoparticles (95mg, 0.552mmol) were heated to 600 °C overnight before being added to solution containing acetone (5ml, 67.5 mmol), 4-nitrobenzaldehyde (151 mg, 1 mmol) and 4-phenyl-2-(pyridin-2-yl)-4,5-dihydrooxazole (120 mg, 0.535mmol) was stirred, at 60 °C, for 72hrs. The solution was filtered and giving a clear orange oil. The product was purified using column chromatography.

^{1}H NMR (400 MHz, CDCl$_3$): 8.21(2H, d, 3JHH=8.0 Hz, pyH), 7.54(2H,d, 3JHH=8Hz, pyH), 5.26(1H,m, CHOH), 2.85 (2H,m, CH2), 2.22(3H, s, CH3) ppm.

6.6.5 PyBox/CeO$_2$ catalysed Michael addition

CeO_2 nanoparticles were heated to 600 °C overnight before being added to solution of chalcone (1.2 mmol) and 1.2 mmol Michael donor (either dimethyl malonate or Meldum's acid) in 5 mL ^{t}BuOH. The solution was stirred at 40 °C, for 72hrs. The solution was then filtered to recover the CeO_2 nanoparticles and the product purified by using column chromatography.

Dimethyl 2-(3-oxo-1,3-diphenylpropyl)malonate

textbf[1]H NMR (400 MHz, CDCl$_3$): 7.91 (2H, m), 7.53 (1H, m), 7.45 (2H, m), 7.27 (4H, m), 7.22 (1H, m), 4.19 (1H, m), 3.88 (1H, d), 3.75 (3H, s), 3.57 (1H, dd), 3.53 (3H, dd), 3.49 (1H, dd)

5-(1,3-diphenyl-3-oxopropyl)-2,2-dimethyl-1,3-dioxane-4,6-dione

^{1}H NMR (400 MHz, CDCl$_3$): 8.21-7.45 (10H, m), 4.62 (1H, m), 4.31 (1H, m), 3.50 (2H, dm), 1.67 (3H, s), 1.35 (3H, s)

References

(1) Berova, N.; Bari, L. D.; Pescitelli, G. *Chemical Society Reviews* **2007**, *36*, 914–931.

(2) Williamson, M. P. In *Modern Magnetic Resonance*, 2008.

(3) What is the Jablonski diagram?, https://www.quora.com/What-is-the-Jablonski-diagram, Date accessed: 27/09/17.

(4) SEM Layout and Function - http://www.ammrf.org.au/myscope/images/sem/layout-and-function.png - Date Accessed: 27/09/17.

(5) Brown, M. E. Introduction to Thermal Analysis: Techniques and Applications., 1988.

(6) Image Formation Basics - http://www.ammrf.org.au/myscope/tem/background/concepts/imagegene -Accessed 27/09/17.

(7) X-Ray Powder Diffractometry - http://lipidlibrary.aocs.org/Biochemistry/content.cfm?ItemNumber= Date accessed: 27/09/17.

(8) Joo, J.; Kwon, S. G.; Yu, T.; Cho, M.; Lee, J.; Yoon, J.; Hyeon, T. *The Journal of Physical Chemistry B* **2005**, *109*, 15297–15302.

(9) Delclos, T.; Aimé, C.; Pouget, E.; Brizard, A.; Huc, I.; Delville, M.-H.; Oda, R. *Nano Letters* **2008**, *8*, 1929–1935.

(10) Katritzky, A. R.; Tala, S. R.; Abo-Dya, N. E.; Gyanda, K.; El-Gendy, B. E.-D. M.; Abdel-Samii, Z. K.; Steel, P. J. *The Journal of Organic Chemistry* **2009**, *74*, 7165–7167.

Chapter 7

Conclusions and Future Work

7.1 Conclusions

Thus, we have developed a range of novel chiroptically-active metal oxide nanoparticles. All nanomaterials have been characterised by various instrumental techniques, confirming the formation of our targeted nanomaterials. This was achieved by a range of "bottom-up" approaches, including sol-gel and hydrothermal techniques. The as-synthesised metal oxide nanomaterials are all chiroptically-active, which has been proven through the use of CD spectroscopy.

A new chiroptically-active and luminescent TiO_2 nanomaterial was prepared by using either D- or L-DPEN as a chiral ligand in a benzyl alcohol mediated synthesis. This luminescent TiO_2 nanomaterial also has the second highest quantum yield ever reported for luminescent TiO_2, with a quantum yield of 3.5 %.[1]

Chiral polymer templates made from a tartaric acid and PEI complex were used for the production of an amorphous, chiroptically-active TiO_2 based nanomaterial. The material was not found to be chiroptically-active after removal of the template and crystallisation of the amorphous TiO_2 nanomaterial. A similar system using 16-2-16 gemini tartrates has also been investigated as a means to prepare a TiO_2 nanomaterial with a helical morphology. This has provided promising results with a chiroptically-active TiO_2 material having been produced that exhibits a helical

morphology under examination using SEM.

Water soluble, chiroptically-active TiO_2 NPs have also been prepared by a phase transfer protocol from the organic phase with D- or L- disodium tartrate. NMR analysis of these NPs has proven difficult at the current time due to an excess of the disodium tartrate present after the phase transfer protocol.

chiroptically-active Mn_3O_4 NPs have been prepared using hydrothermal techniques. Various chiral ligands such as amino acids, amino alcohols and a range of "priveliged" ligands from the field of asymmetric homogeneous catalysis have been proven to be suitable for the preparation of these chiroptically-active Mn_3O_4 NPs. These Mn_3O_4 NPs were also tested for activity against against breast cancer cells, the results of this investigation were inconclusive. A chiral manganese-based MOF was also investigated as a means to prepare a chiral manganese oxide, the resulting material did not display any chiroptical activity however.

Chiroptically-active ZnO NPs have also been prepared using a sol-gel approach. The chiral component of these systems are chiral amino acids that have been modified at the N-position with an 18-C chain. The chiroptical activity of the ZnO NPs has been shown to dependent on the binding behaviour of the chiral ligand, with the N-stearoyl-L-alanine ligand inducing no CD in the ZnO NPs whereas the N-stearoyl-L-cysteine and N-stearoyl-glutamic acid ligands do induce CD in the ZnO NPs.

The chiroptically-active Mn_3O_4 and TiO_2 NPs were also tested for catalytic activity for a range of organic transformations. The NPs were found to be catalytically inactive. This is proposed to be due to the chiral ligand blocking access of the reagents to the catalytic sites present on the surface of the metal oxide NPs. chiroptically-active Mn_3O_4 NPs were also used successfully as part of a working electrode for the electrochemical oxidation of L-tryptophan, there was no enantioselective effect present however.

It has been demonstrated that it is possible to catalyse both aldol and Michael reactions by ligand self assembly on the surface of CeO_2 NPs. The products of these

reactions are racemic however, this is most likely due to a mismatch in pK_a of the nitrogen atoms in the chiral PyBox ligands. This has been inferred through the use of Michael donors of differing pK_a.

In conclusion, our work has demonstrated the development of a range of chiroptically-active metal oxides. It is anticipated that these new chiroptically-active metal oxide based materials may find applications in areas such as enantioselective catalysis, chiroptical devices, anti-bacterial coatings, biomedical applications and enantiomeric separation.

7.2   Future Work

A range of work has arisen from our research that we believe would be advantageous to explore, with the aim of furthering our aims of innovation in the field of chiroptically-active metal oxide nanomaterials.

NMR techniques will be used to characterise the ligand sphere surrounding the chiroptically-active TiO_2, Mn_3O_4 and ZnO NPs prepared in our work. The aim will be to explore how the ligand interacts with the surface of the metal oxide NPs, and how this interaction effects the induced CD that is present in these systems. A range of techniques will be used, both 1D and 2D, to probe the nature of the ligand sphere.

The preparation of a helical TiO_2 nanomaterial by chiral gemini tartrates will be optimised in future work. This part of our work has shown great promise and will be further investigated with the aim to produce a chiroptically-active TiO_2 nanomaterial with helical morphology.

Aspects of our work on chiroptically-active ZnO NPs require further studies, and computer modelling and is to be explored in the future. Also, it will be important to investigate biological behaviour of chiroptically-active and luminescent ZnO NPs *in vitro* for potential biosensing and bioimaging applications.
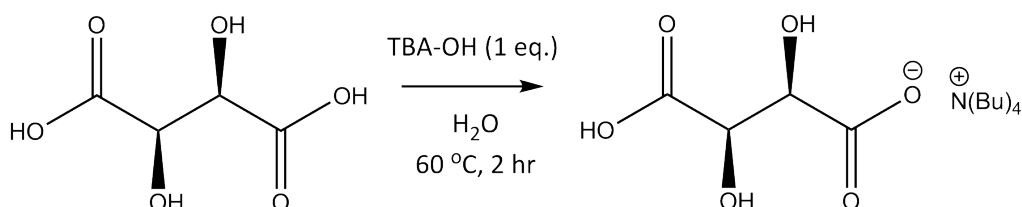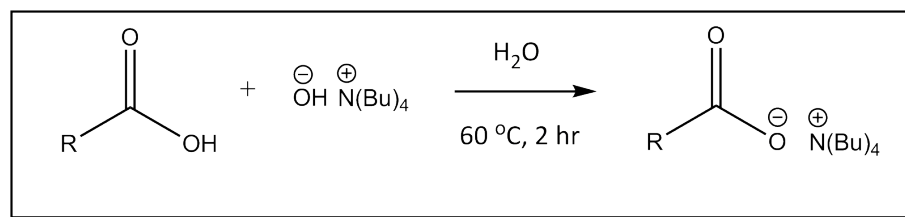
Scheme 7.1: Synthetic scheme for the preparation of chiral ionic liquids

A potential avenue for solving the issue of a mismatch in Lewis bascity in the ligand self-assembled catalyst presented in Chapter 5 is the use of chiral bis(oxazoline) ligands that possess a symmetry centre of inversion (Figure 7.1). In this system, it does not matter which way around the catalyst assembles as each configuration would have the necessary steric hindrance beside the catalytic site. The suitability of these ligands for both aldol and Michael reactions shall be explored.
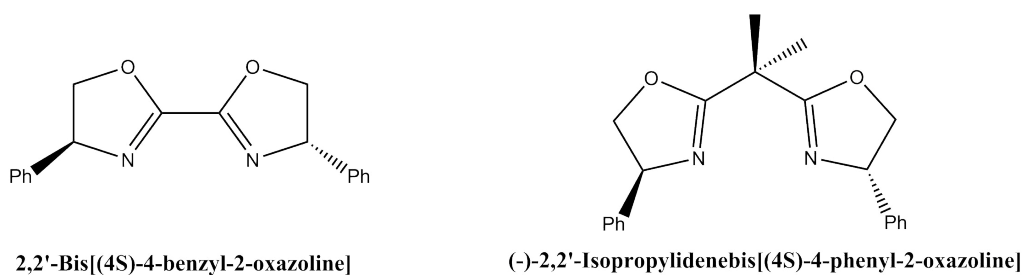

2,2'-Bis[(4S)-4-benzyl-2-oxazoline]   **(-)-2,2'-Isopropylidenebis[(4S)-4-phenyl-2-oxazoline]**

Figure 7.1: Proposed chral bis(oxazoline) ligands for asymmetric catalysis

Chiral ionic liquids will be explored as a synthetic medium for the production of chiroptically-active metal oxides. Ionic liquids have been demonstrated in the literature to be a suitable medium for the production of metal oxide nanomaterials[2,3] but have not to our knowledge, been used to produce a chiral nanomaterial. We have prepared as chiral ionic liquid using chiral carboxylic acids such as tartaric acid according to a preparation reported by Allen *et al.*[4] (Scheme 7.1).

The chiral ionic liquid has been prepared and initial CD investigations of this chiral ionic liquid indicate the formation of a different species to the D-tartaric acid (Figure 7.2). This chiral ionic liquid will be utilised in future work in an attempt to synthesise chiral metal oxides by a novel synthetic approach.
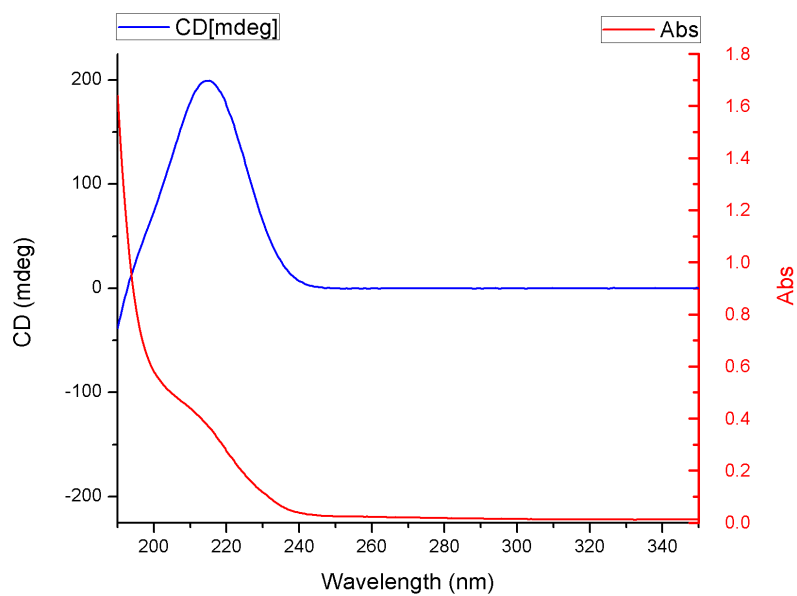
(a) CD and UV-vis of D-tartaric acid
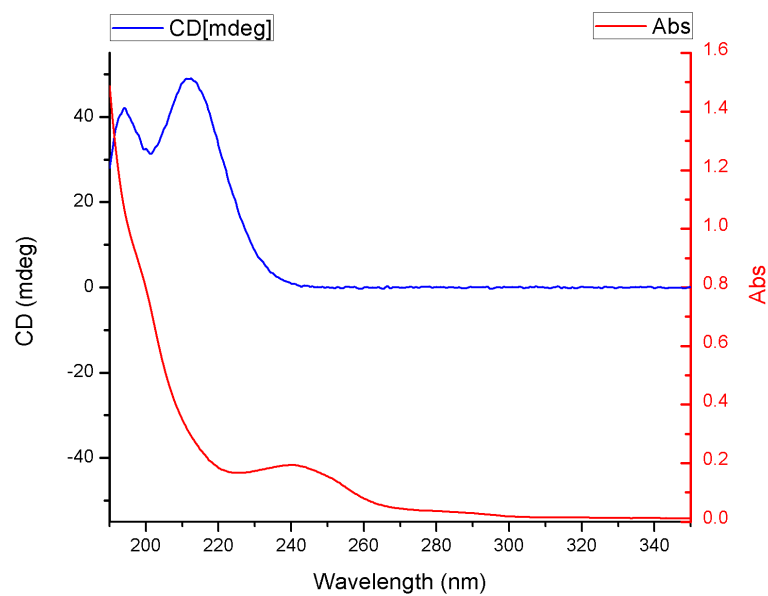
(b) CD and UV-vis of chiral ionic liquid

Figure 7.2: Comparison of D-tartaric acid and chiral ionic liquid

References

(1) Cleary, O.; Purcell-Milton, F.; Vandekerckhove, A.; Gun'ko, Y. K. *Advanced Optical Materials* **2017**, DOI: `10.1002/adom.201601000`.

(2) Bussamara, R.; Melo, W. W. M.; Scholten, J. D.; Migowski, P.; Marin, G.; Zapata, M. J. M.; Machado, G.; Teixeira, S. R.; Novak, M. A.; Dupont, J. *Dalton Transactions* **2013**, *42*, 14473–14479.

(3) Liu, D.-P.; Li, G.-D.; Su, Y.; Chen, J.-S. *Angewandte Chemie International Edition* **2006**, *45*, 7370–7373.

(4) Allen, C. R.; Richard, P. L.; Ward, A. J.; van de Water, L. G. A.; Masters, A. F.; Maschmeyer, T. *Tetrahedron Letters* **2006**, *47*, 7367–7370.